HIghly advanced Probabilistic design and Enhanced Reliability methods for high-value, cost-efficient offshore WIND

Title: Methods for efficient ULS reliability calculations and their impact on probabilistic design

Deliverable no: D4.2

Delivery date: 06 June 2024

Lead beneficiary: IFP Energies nouvelles

Dissemination level: Public

This project has received funding from the European Union's Horizon 2020 Research and Innovation Program under Grant Agreement No. 101006689

Author information:		
Name	Organization	Email
A. Cousin	IFPEN	alexis.cousin@ifpen.fr
M. Munoz Zuniga	IFPEN	miguel.munoz-zuniga@ifpen.fr
L. Franceschini	IFPEN	
M. Guiton	IFPEN	martin.guiton@ifpen.fr
C. Agrell	DNV	christian.agrell@dnv.com
N. Dimitrov	DTU	nkdi@dtu.dk
O. Gramstad	DNV	odin.gramstad@dnv.com
S. Marelli	ETH	marelli@ibk.baug.ethz.ch
M. McWilliam	DTU	mimc@dtu.dk
S. Schaer	ETH	styfen.schaer@ibk.baug.ethz.ch
E. Vanem	DNV	erik.vanem@dnv.com
H. Wang	DNV	hong.wang@dnv.com
S . Winter	DNV	sebastian.winter@dnv.com
M. Kelly	DTU	mkel@dtu.dk

Acknowledgements/Contributions::		
Name	Name	Name
G. Gudendorff (IFPEN)	G. Huwart (IFPEN)	C. Peyrard (EDF)
Y. Poirette (IFPEN)	A. Lovera (EDF)	B. Sudret (ETH)

Document information:					
Version	Date	Description	Prepared by	Reviewed by	Approved by
1.0	06/06/2024	Official	Authors listed above	R. El Amri (IFPEN), J.P. Murcia (DTU)	N. Dimitrov

Definition:	

Contents

List of Figures

List of Tables

List of Abbreviations

AK	Adaptive Kriging,
BNN	Bayesian Neural Network,
CAPEX	Capital Expenditure,
CoV	Coefficient of Variation,
DLC	Design Load Case,
DP	Design Point,
DS	Direct Sampling,
EOG	Extreme Operational Gust,
IFORM	Inverse First-Order Reliability Method,
FLS	Fatigue Limit State,
FNN	Feedforward Neural Network,
FORM	First Order Reliability Method,
GEV	Generalized Extreme Value,
GP	Gaussian Process,
KL	Karhunen-Loève,
LLN	Law of Large Numbers,
LT	Long Term,
MC	Monte-Carlo,
MCMC	Markov Chain Monte Carlo,
ML	Machine Learning,
MLE	Maximum Likelihood Estimate,
OWT	Offshore Wind Turbine,
PCE	Polynomial Chaos Expansion,
RBDO	Reliability-Based Design Optimisation,
ULS	Ultimate Limit State,
SLS	Service Limit State,
SORM	Second Order Reliability Method,
ST	Short Term,

1 Executive Summary

Large safety margin can be gained in the design of Offshore Wind Turbines (OWT) by reducing the uncertainty. This report focuses on Ultimate Limit States (ULS) which are deemed to often be the critical conditions of design. Current versions of international standards IEC (2019b,a); DNVGL (2018) introduce a deterministic formulation in which sources of uncertainty are represented by safety factors on load and resistance parts. These factors were inherited from offshore oil and gas engineering, and need to be re-calibrated for the different context of offshore wind. We consider here several reliability methods with the aim to demonstrate their feasibility in the analysis of realistic use-cases.

Section 2 introduces the context and motivation of this work, referring to few research papers on OWT reliability. Section 3 presents the probabilistic formulation of ULS that is retained in this report, with the list of various uncertainty contributions, including that on wind and wave representation, model approximation and material resistance.

Section 4 compares four methods dedicated to the case of stationary ULS on a simplified 2D benchmark in wind parameters, with NREL 5MW turbine and a surrogate model developed in Dimitrov et al. (2022); Schär et al. (2023) to replace the time costly multiphysics simulator. The methods are Environmental Contour, Bayesian Neural Network (BNN), Gaussian Process (GP) with sequential sampling, and an outcrossing optimization in jointed Long-Term (LT) and Short-Term (ST) space. Due to the challenging difficulty to get an accurate estimate of the tail distribution for the critical loading on OWT components, most of the methods did not succeeded to compute the annual failure probability with a feasible computational time. The BNN faces difficulty due to the Gaussian assumption of the tail distribution. The outcrossing optimization is limited by FORM in high dimensions with possible non connected local minima. However, the method with GP and sequential sampling is demonstrated to be well suited for this application, if sorting a minimum number of stochastic seeds to capture the ST variability (introduced by wind turbulence and wave irregularity). It compares well with Q90 contours loading for a fixed foundation OWT but not for a floating OWT as failure domain appears to be inside the contour. The convergence of annual failure probability with this method is more difficult than for return period but the reason found is due to very few outliers significantly deviating from the Gumbel fit of ST maxima which may be explained by the use of a surrogate out of its training domain instead of a physical simulator of offshore wind turbine dynamics.

Section 5 investigates with the same objective two methods dedicated to the case of transient ULS, with the occurrence of wind gust and possible synchronous grid-loss for the case of an OWT supported on a monopile of Teesside wind farm of EDF (East coast of UK). Gusts are defined according to the selection of real events from Kelly and Vanem (2022) instead of the IEC Extreme Operating Gust (EOG). The transient ULS dependency on ST parameters is small enough to be neglected when compared to that on LT parameters. A Monte-Carlo (MC) sampling shows that shutdown only do not provide higher load than the stationary case (extreme operational conditions) while the extreme load is largely increased when introducing gust. Within gust parameterization, acceleration provides the dominant effect on ULS. To improve the feasibility of such method for computing the failure probability, an approach combining GP and active learning is then presented on the same case study.

In section 6, we demonstrate the feasibility of the reliable ULS approach, with an appli-

cation on an OWT of the Teesside wind farm. From a series of simulations, the selected critical condition is found to be that of plasticity on the monopile at mudline in extreme parked (idle) condition corresponding to DLC6.1. The GP with sequential sampling method successfully converges to a very small annual failure probability much lower than the admissible target of 1.E-4, indicating that the initial design is significantly conservative. An optimization of the tower and monopile design is then conducted by reducing the thickness while checking several constraints for buckling, reliable plasticity at monopile mudline, manufacturability and tower resonance. This optimization with reliable condition was possible thanks to a conservation of the bending moment when changing the design. A final design, mainly constrained by the tower resonance, was found with 21% mass reduction.

Section 7 presents the application of the sequential sampling approach for the floating case study of IEA15MW on UMaine semi-submersible in a South Brittany (West coast of France) site Allen et al. (2020); Capaldo et al. (2021); Peyrard et al. (2022). Similarly to the Teesside case study, the failure probability was estimated with good confidence, after few enrichment cycles only. Furthermore, no optimization was required, as the initial design was already near the design target for the tower basis plasticity in extreme parked (idle) condition.

Section 8 investigates the influence of uncertainty on the wind and wave joint probability, representative of the farm site, on the ULS annual failure probability of the Teesside case study. Taking advantage of the GP final surrogate obtained at the convergence of the sequential sampling method, uncertainty can be propagated without requiring additional simulations. The results show an important effect of the environmental uncertainty on the ULS reliability, suggesting it is worth paying attention to the joint probability fitting, as discussed in Vanem et al. (2023).

Finally, conclusions and perspectives which would be interesting to investigate in future works are given in the last section.

2 Introduction

Offshore wind industry is currently going through a particular market context with a drastic increase of instability after Covid and geopolitical crises. This has put tension on the supply chain an even resulted in several non attribution of assets due to too low return values for operators and investors GWEC (2023). This is particularly true for the case of floating wind installations which are still waiting for the transition from pilot units to industrial deployment.

This situation is not to be interpreted as a loss of interest in this relatively new sector, as offshore wind energy still remains one of the most credible source of renewable energy with current technology. However, it points to the need of lowering the risk for capital investments and insurance, as the failure probability is expected to be significantly higher for Offshore Wind Turbines (OWT) than for onshore ones Li and Guedes Soares (2022). To achieve such a goal, the designer have first derived their conceptions following the guidelines of international standards like IEC (2019b,a); DNVGL (2018), which formulate the problem in terms of target reliability (typically of 10^{-4} for annual failure) and deterministic limit states, uncertainties being accounted for by the use of safety factors on both load and material contributions (see Section 3).

However, the values of these safety factors are deemed to be inherited from oil and gas return of experience for which loading conditions are significantly different than that on offshore wind turbines, requiring to recalibrate them Velarde et al. (2020); Morató and Sriramula (2021). Indeed, OWT are generally installed in shallower water depths (typically up to 60 m for bottom-fixed supports among which monopile are predominant and up to few hundred of meters for floating cases) with harsher sea states. Furthermore, the wind turbine dynamics are also sensitive to turbulent wind interaction, controller strategy and is submitted to a risk of resonance over multiple frequencies from low ones associated to large time varying wind, of the order of 0.1 Hz for waves, few times the latter for rotor harmonics and then up to few Hz for the structure elasticity Vorpahl et al. (2013); Velarde et al. (2019).

For all these reasons, several papers on OWT design have introduced since many years the need to develop reliability approaches, taking explicitly into account all sources of uncertainty (stochastic environmental conditions, epistemic model approximations including that of reliability approach, and both epistemic and stochastic resistance parameters) for evaluating an annual failure probability for a given OWT design Tarp-Johansen et al. (2005); Veldkamp (2008); Muskulus and Schafhirt (2015). Considering that the risk for wind turbines is mainly economical, Nielsen et al. (2023) recently presented a more holistic risk-based assessment approach to estimate the optimal target failure probability from the different cost terms on the expected lifetime horizon: benefits from power production, construction cost, operation and maintenance costs and cost of structural failure. Based on these considerations, an IEC technical specification (IEC, 2023) is currently in preparation. It provides a formal definition of the probabilistic approach to wind turbine design.

As mentioned in previously cited OWT standards, the designer should consider several limit states for all components of the OWT which are classified into Ultimate Limit States (ULS), Fatigue Limit States (FLS), Service Limit States (SLS) and Accident scenarios. In IEC (2019b); DNVGL (2018), bases of Design are composed by a list of Design Load Cases to be checked, corresponding to these limit states. Finding the most critical DLC and more specifically the most critical limit state (including the location of the component on the structure), for a given OWT design in site-specific conditions, is not trivial and is rarely discussed in the literature. From the author's experiences, the more critical conditions are however usually found for ULS or FLS. If most of OWT ULS reliability literature focuses on a single OWT case only, in reality the designer has first to consider the OWT configuration within a given farm. In addition to possible variability of site (e.g. water depth) and OWT configurations in a wind farm, the main effect is the well know wake deficit and added turbulence in a zone downwind and close enough to an operating turbine. Concerning design conditions, the most obvious effect is that of added turbulence which may increase the fatigue on downwind OWT. However, standards also mention that the wake added turbulence should be added to the ambient one for extreme operational ULS for Extreme Turbulence Model DNVGL (2016). In the present work, for the sake of simplification we will however consider that we can neglect the wake effect on ULS design in probabilistic design. Contrarily to the FLS investigated in D43 report of HIPERWIND, we will hence not consider the wake modification of mean speed and turbulence in the wind farm case studies which was obtained in Ardillon et al. (2022). Consequently, the studies of this report will consider a single representative OWT which is submitted to turbulent ambient wind conditions which probabilistic distribution is assumed to encompass that of any turbine

within the farm.

Many approaches have been devoted to the fatigue risk Veldkamp (2008); Horn et al. (2019); Velarde et al. (2020), arguing that OWT are submitted to a huge number of load variations during their service life, about 25 years, and also motivated by the great difficulty to detect the risk of fatigue damage during maintenance visits. As poly-cyclic fatigue is an accumulation of microcracking coalescence over most of the structure life, its evaluation requires to compute the mean expectation over the joint probability of all environmental conditions, hence introducing a computational challenge for OWT where both wind and wave parameters combination need to be considered. However, due to the weight of occurrence, the main contribution to FLS is expected to come from the body of joint distributions which is more easy to determine than the tail of the distributions. This is particularly true when few monitoring data are available in pre-design and during the first years of exploitation for the reevaluation of structure reliability. Despite of its importance, FLS is nevertheless dominated by a very large uncertainty (typically of log-normal distribution with Coefficient of Variation (CoV) up to 0.3) due to the very strong approximation of independent load events with Palmgren-Miner cumulative linear damage which neglects the time-dependency Veldkamp (2008); JCSS (2011); Muskulus and Schafhirt (2015). It is then unlikely that OWT operators will accept to reduce the FLS conservatism until this approximation can be clearly evaluated. Such goal is very ambitious, as it would require to consider the whole stochastic combinations over the service life. Fortunately, with the increase of monitoring on OWT structural components, the research community on offshore wind is currently developing new techniques based on digital twins (i.e. combining models and monitoring data) which will be helpful to reduce the fatigue uncertainty as the life of the OWT advances Dimitrov and Natarajan (2019); Wang et al. (2022); Dimitrov and Göçmen (2022); Branlard et al. (2024); Moynihan et al. (2024).

Conversely to FLS, ULS approaches first rely on an accurate determination of the tail distribution of the OWT component load. Often this estimation is based on statistical extrapolation, which is associated with large uncertainty Dimitrov (2016); van Eijk et al. (2017).

Considering the target annual failure probability of 10^{-4} in standard, van Eijk et al. (2017) claimed a sample of size up to 10^5 needs to be available for an acceptable prediction of 50-years ULS with deterministic and safety factors approach and both for aggregate-before-fitting (i.e. fit on whole data) or fitting-before-aggregate (e.g. binning on mean wind speed suggested by IEC). Because ULS of OWT is interested in rare events, the designer is facing a locking challenge of numerical computations, enhanced by the high computational cost of aero-servo-hydro-elastic simulations Vorpahl et al. (2013).

To palliate these limitations, several approaches have been proposed which replace costly simulations with surrogate models (e.g. GP Huchet et al. (2019); Slot et al. (2020); Cousin (2021); Cousin et al. (2024) or Polynomial Chaos Expansion (PCE) Dimitrov et al. (2018); Slot et al. (2020), Artificial Neural Network Müller et al. (2017); Wang et al. (2023), Bayesian Neural Network (BNN) Dimitrov et al. (2022) or auto-regressive with exogenous input model (mNARX) Dimitrov et al. (2022), Schär et al. (2023)) with the possibility to use a traditional Monte-Carlo (MC) reliability strategy. Alternately, one can directly reduce the number of calls to the simulator in the integration with e.g. Bayesian quadrature combined to kernel herding Fekhari et al. (2024). Another way to lighten the computational burden is to use well known optimisation approaches in reliability that

are First-Order Reliability Method (FORM) or Second-Order Reliability Method (SORM) Lemaire et al. (2009). However, FORM and SORM assume linear and quadratic limit states respectively which may be not relevant for the non-linear dynamics of OWT Velarde et al. (2019). To avoid such limitations, it is also possible to use variance reduction techniques like Importance Sampling Dimitrov et al. (2018); Muskulus and Schafhirt (2015); Murangira et al. (2015). Finally, another way that has been suggested is to assume that LT variation of parameters dominate over ST (typically 10 min) ones on the limit states, allowing to reduce the integral over the input parameters multi-dimensional domain to a contour on 50-years joint probability Winterstein et al. (1993); Vanem (2018); Velarde et al. (2019). However, contour methods will provide loads corresponding to a return period rather than failure probability.

If these approaches reduce the complexity they have however been insufficient to allow the common use of the reliability methods in industrial design of OWT. In this report, we investigate several new ULS methodologies with the goal to evaluate their feasibility for the design of representative use cases of OWT. The following sections first present the probabilistic formulation of ULS used in this report. We distinguish the case of stationary events from that of transient events which correspond to different dedicated methods. Section 4 compares on a simplified 2D benchmark four methods : Environmental Contours, BNN, GP with Sequential Sampling, and Outcrossing with Optimization of Long-Term (LT) and Short-Term (ST) parameters. Only the GP with Sequential Sampling was selected for giving acceptable accuracy on the annual failure probability with feasible computations. Section 5 similarly presents a method for the case of a transient event combining gust measurements selected in 16 years of measurements during WP2 of HIPERWIND project Kelly and Vanem (2022) with a possible loss of grid connection.

Once the annual probability of failure is estimated, assuming the design was appropriately done with a safety margin, the designer would like to take advantage of this knowledge to reduce the CAPEX for instance by removing material in some components. When going to this perspective, one enters the very challenging world of Reliability-Based Design Optimisation (RBDO). Indeed, as discussed in Stieng and Muskulus (2020); Cousin (2021), the problem then becomes a double loop very expensive to solve, inner loop for the reliability and outer loop for the design optimisation. Several approaches are proposed to avoid it, the more known being the sequential optimization and reliability analysis (SORA) method of Du and Chen (2004) decoupling the two loops into a sequence of deterministic optimization and reliability analysis, and the Single Loop Approach (SLA) reformulation Chen et al. (1997), both assuming linearity of the limit state (FORM). In Cousin (2021), for the fatigue of mooring lines of a Floating OWT constrained by maxima on the floater kinematics, a reformulation using Extreme Value Theory and an adaptive kriging in the LT parameter space is shown to converge efficiently. Alternately, Stieng and Muskulus (2020) assumes an uncoupling between a design-dependent deterministic part of the limit state and a design-independent reliable part to obtain a computationally feasible procedure. RBDO was out of the scope of HIPERWIND project. Nevertheless, we present in section 6 an interesting simplified approach to get a new design, with saved material and reduced conservatism, for the OWT case study supported on a monopile which is based on Teesside wind farm of EDF in UK for which ULS drove the design of the monopile. The failure probability associated to the critical limit state (von Mises stress at mudline) is computed with the GP with sequential sampling approach. The feasibility of the same approach is also demonstrated for a second

case study with a floating OWT for the IEA15MW turbine on UMaine semi-submersible floater in South Brittany site.

To enforce further the validation of these feasible estimate of failure probability, one may consider its robustness with regard to the confidence on the multiple source of uncertainties which have been selected. Indeed, a weakly justified probabilistic distribution may induce significant approximation in the reliability evaluation of a design. Among these sources, one may first consider the one on wind and wave conditions at the beginning of the OWT modeling chain. It was shown during WP2 of HIPERWIND, that significant uncertainty on the tail of the probabilistic distribution of wind and wave LT parameters could occur due to the arbitrary choice of the statistic model Vanem et al. (2023). To study the consequence, one may desire to perform a global sensitivity analysis. In Robertson et al. (2019), a simple screening with Elementary Effect approach (see details in the reference) was used to avoid unfeasible computational cost of usual sensitivity approaches like the Sobol indices one requiring MC sampling. More recently, Shittu et al. (2022) presented a Stochastics Sensitivity Analysis employing a quadratic interpolation of the limit states in the parameter space. As discussed in Robertson et al. (2019)'s introduction, this could however lead to significant approximation for ULS reliability. In section 8, we chose to replace the sensitivity information by a simpler robustness one. The uncertainty on wind and wave LT parameter distributions was propagated to the failure probability of Teesside case study, by exploiting the results of the ULS GP with sequential sampling.

3 Probabilistic ULS formulation for OWT design

Let us first recall that, as already discussed in section 2, we neglect in the present work possible heterogeneity both on the loading (e.g. wake influence for operational turbine ULS, varying water depth) and on the resistance of OWT components (e.g. different turbines or foundation configurations) within a wind farm. Hence, we will consider directly the case of a single representative OWT which is submitted to extreme ambient wind conditions encompassing the conditions seen by all turbines of the wind farm.

As usual in offshore engineering, we assume a timescale separation in the energy spectral density of stochastic processes representing the wind speed at hub height and the wave elevation. This assumption enables to distinguish ST variation of these processes on a duration ΔT and LT variation over the service life or annual quantities for what concerns ULS in IEC (2019b); DNV (2021) standard. The ULS failure probability of a component of an OWT over ΔT can then be written as follows:

$$p_f = \mathbb{P}_{\zeta,\eta(.,\xi),\nu(.,\xi)}\left(\max_{[0,\Delta T]} s\left(t;\zeta,\eta(.,\xi),\nu(.,\xi)\right) > \rho\right) \tag{3.1}$$

where:

- ΔT is set to ten minutes for the fixed-case or one hour for the floating case study;
- ζ is a random vector representing the model uncertain parameters;
- ξ is a random vector composed of not independent random variables representing the uncertainties on the LT environmental parameters. These parameters correspond to the wind and wave statistics over $[0, \Delta T]$;
- $t \rightarrow \eta(t,\xi)$ and $t \rightarrow \nu(t,\xi)$ represent respectively the ST sea elevation and wind velocity. They are both a time-dependent random process parameterized by ξ;
- s is the quantity of interest. It is a time-dependent output of a numerical simulator such at the stress as some location of the structure for example;
- ρ is a given resistance threshold.

The values of ΔT are assumed to be long enough to get stationary conditions for the case of stationary events.

It is to be noticed that despite p_f is a failure probability over ΔT, both the LT and ST uncertainties are considered in the failure probability.

Considering that a year is composed of N independent periods of duration ΔT, the annual failure probability p_f^{year} can be computed from (3.1) as[1]:

$$p_f^{year} = 1 - (1 - p_f)^N \tag{3.2}$$

where N is the number of intervals of duration Δt over one year. For $\Delta T = 10$ minutes, $N = 52596$ and for $\Delta t = 1$ hour, $N = 8766$.

In this report, four cases are introduced for which a ULS failure probability that can be written as equation (3.1) need to be estimated. For each case, the properties and the

[1] Denoting A_i the event "the QoI exceeds the threshold ρ over the i-th interval of length ΔT", we have $p_f^{year} = \mathbb{P}\left(\cup_{i=1}^N A_i\right) = 1 - \mathbb{P}\left(\cap_{i=1}^N A_i^c\right) = 1 - \prod_{i=1}^N \mathbb{P}\left(A_i^c\right) = 1 - \prod_{i=1}^N \left(1 - \mathbb{P}\left(A_i\right)\right) = 1 - (1 - p_f)^N$, where A_i^c is the complement event of A_i and p_f is the failure probability over ΔT.

physical meanings of ΔT, ζ, ξ, η, ν, s and ρ vary. Thus, a description of the objects is given at the beginning of the section introducing each case.

The estimation of p_f is a challenging task since a naive approach would require to sample many realizations of the different sources of uncertainty and to perform as many costly simulation. The smaller p_f is, the greater the number of simulations, since the probability must be estimated accurately. Different strategies are introduced in this deliverable to compute p_f efficiently depending on the ST processes being stationary or not.

Finally, we introduce the random variable Y defined by:

$$Y = \max_{[0,\Delta T]} s\left(t; \zeta, \eta(.,\xi), \nu(.,\xi)\right) \tag{3.3}$$

which depends on the LT and ST uncertainties.

4 Methodologies for stationary ULS

In this section, we use a simplified benchmark 2D study (in wind speed mean and standard deviation space) to compare four ULS reliable methods dedicated to the case of stationary events: environmental contours, GP with sequential sampling, BNN and outcrossing optimization in joint ST-LT space. The simplification also concerns for all methods the use of a surrogate replacing the OWT multiphysics simulator to lighten the computational cost. The final objective of this section is to select the more appropriate method in terms of accuracy and associated computational cost to apply it on the complete fixed foundation (section 6) and floating (section 7) OWT case studies. The stationarity concerns the ST wind speed process and the wave elevation process for given fixed LT parameters which are respectively denoted η and ν in 3.1.

4.1 Description of the methods

4.1.1 Environmental Contours

The environmental contours approach is a well established method, that is recommended in DNV's recommended practice (DNV, 2021). Different variants of this method exist (Haver and Winterstein, 2009; Huseby et al., 2013; Leira, 2008; Silva-González et al., 2013; Montes-Iturrizaga and Heredia-Zavoni, 2015; Li et al., 2016; Lutes and Winterstein, 2016; Haselsteiner et al., 2017; Chai and Leira, 2018; Manuel et al., 2018; Ross et al., 2019; Haselsteiner et al., 2021), and several applications of this approach are reported in the literature, especially ocean engineering applications (Niedzwwecki et al., 1998; G.S. and Moan, 2001; Baarholm et al., 2010; Muliawan et al., 2013; Vanem, 2018), but also for offshore wind (Velarde et al., 2019), earthquake engineering (van de Lindt and Niedzwecki, 2000) and bridge design (Giske et al., 2018; Castellon et al., 2022).

This approach does not aim directly to estimate a probability of failure as defined in equation (3.1) but to find the sets of LT parameters (denoted ξ in equation (3.1)) with a given return period. The ST uncertainty is introduced by considering a sample with different random seeds for wind and wave processes, taking high quantiles to be conservative. This information can then be used to estimate the distribution of Y (i.e. the maxima of the quantity of interest) defined in equation (3.3).

4.1.2 Bayesian Neural Network

Surrogate modelling is a popular approach for simplifying an analysis by mapping the outputs of a complex model or a physical system with simple, computationally efficient, and analytical functions. The simplification comes at the expense of introducing an additional uncertainty in terms of 1) model uncertainty (since the surrogate model is not a perfect mapping of the actual model), and 2) statistical uncertainty, as the finite sample size used for model training means the variable space is not explored fully.

Typical surrogate modelling approaches employ Machine Learning (ML) or other model fitting procedures. While the majority of ML techniques provide deterministic models, in the present work we are particularly interested in models that capture uncertainty and possibly provide probabilistic outputs (the so-called stochastic simulators). One of the primary models of choice is the Bayesian Neural Network (BNN) Blundell et al. (2015),

which is a probabilistic adaptation of the commonly used Feedforward Neural Networks (FNNs, Goodfellow et al. (2016)). BNNs introduce *variational layers*, where the weights and biases are probabilistic, represented by their joint distribution (means and variances) rather than a single deterministic value. As the name suggests, BNNs use Bayesian inference to calibrate the probabilistic parameters. The classical Bayesian inference approach Tiao and Box (1992) involves determining the most likely posterior joint distribution of the parameters, typically including the full covariance matrix for all parameters. This is well suited for calibrating a model with a few parameters, but it would fail for the case of Neural Networks due to the very large number of parameters in the network. Therefore, BNNs apply a crucial simplification by assuming that a set of suitable model parameters can be found that are sufficiently uncorrelated so that their joint distribution can be represented by their mean values and a diagonal covariance matrix. This assumption can be applied to the cross-correlations of parameters within a single layer of the BNN. The assumption may be justified by the fact that Neural Network parameters have no physical meaning and are randomly initialized. Dependencies between parameter distributions in different layers can be estimated through chain differentiation as with regular neural networks Blundell et al. (2015). Therefore, inferring the main diagonal of the covariance matrix along with the parameter means is sufficient. Subsequently, the total number of parameters to be inferred in a BNN is not more than two times larger than in a regular FNN. BNNs can be tailored to represent epistemic (model) uncertainty, as well as aleatoric uncertainty caused by variations in the data that are not explained by any of the input variables. The probabilistic parameters in the variational layers are a representation of model uncertainty. Further, the output layer of a BNN can be chosen to return output distribution parameters rather than a single value. With this setup, the outputs have a probability distribution whose expected value is conditional on the input variables, while the variance is a representation of the aleatory uncertainty. Figure 4.1 illustrates how different BNN setups affect its behavior.

Running a single model prediction with a BNN will result in a realization with scatter similar to the actual dataset, as illustrated in Figure 4.2.

The BNN method can thus be used to predict the distribution of Y defined in equation (3.3) given a set of LT parameters. If this prediction is accurate, the failure probability of equation (3.1) becomes fast to evaluate since the BNN can replace the costly simulator.

4.1.3 GP and sequential sampling

We denote $\boldsymbol{X} = (\xi, \zeta)$ the random vector grouping the LT and the model uncertainties and is described by joint probability distribution $f_{\boldsymbol{X}}(x)$. Given a realization $\boldsymbol{x}$ of this random vector, the maxima of the quantity of interest (load on the OWT component) denoted Y in section 3 is a random variable with an (unknown) probability density function $g_{Y|\boldsymbol{X}}(y|\boldsymbol{x})$ and whose uncertainty comes from the random wind and wave processes. The distribution of Y can then in principle be found with:

$$g_Y(y) = \int g_{y|\boldsymbol{X}}(y|\boldsymbol{x}) f_{\boldsymbol{X}}(\boldsymbol{x}) dx. \tag{4.1}$$

In the present case, the distribution $g_{y|\boldsymbol{X}}(y|\boldsymbol{x})$ is not known, but samples from $g_{Y|\boldsymbol{X}}(y|\boldsymbol{x})$ can be obtained by running simulations of the structural response. In principle, the integral 4.1 can then be estimated through a brute-force MC approach. However, this is still a

computational demanding task, and may in many cases be impossible if simulating the structural response is computational demanding.

In the following, we present the ULS methodology GP regression and sequential sampling described in Gramstad et al. (2020), see also Mohamad and Sapsis (2018) to estimate the integral 4.1. The main steps in the methodology can be summarized as follows:

1. Introduce a parametric distribution $\hat{g}_{Y|\boldsymbol{X}}(y|\boldsymbol{x},\boldsymbol{\theta}(\boldsymbol{x}))$ for the ST response (i.e. $\hat{g}_{Y|\boldsymbol{X}}(y|\boldsymbol{\theta}(\boldsymbol{x}))$ represents an approximation of the "true" distribution $g_{Y|\boldsymbol{X}}(y|\boldsymbol{x})$).
2. A GP regression model is used to represent the distribution parameters $\boldsymbol{\theta}(\boldsymbol{x})$, which are fitted based on a limited number of ST response simulations.
3. The estimated LT response distribution is obtained from 4.1 by replacing $g_{Y|\boldsymbol{X}}(y|\boldsymbol{x})$ with $\hat{g}_{Y|\boldsymbol{X}}(y|\boldsymbol{\theta}(\boldsymbol{x}))$.

Parametric model for the ST response In the present work two different models $\hat{g}_{Y|\boldsymbol{X}}(y|\boldsymbol{\theta}(\boldsymbol{x}))$ for the ST response have been considered: the Gumbel-distribution and the generalized extreme value (GEV) distribution. See also Dimitrov (2016) for a detailed comparison of several asymptotic load techniques including other choices of distribution and strategies for de-clustering of local maxima. The Gumbel distribution has two parameters $\boldsymbol{\theta} = (\alpha, \beta)$ location and scale, and the GEV distribution has three parameters $\boldsymbol{\theta} = (\alpha, \beta, \gamma)$ location, scale and shape.

From n_{seeds} random response simulations for a given input $\boldsymbol{x}$, the best fit distribution parameters $\boldsymbol{\theta}(\boldsymbol{x})$ are found as the maximum likelihood estimate (MLE) for the given observations $y = (y_1, ..., y_{n_{seeds}})$. An important part of the present methodology is to include the uncertainty in the distribution parameters throughout the analysis. This is achieved by considering the likelihood of the distribution parameters under the given observations, i.e. $p(y|\boldsymbol{\theta})$.

In order to incorporate this uncertainty into the GP-model, the Gumbel and GEV likelihoods are approximated by 2- and 3-dimensional Gaussian likelihoods, respectively. The best-fit Gaussian likelihood is found by drawing samples from the distribution proportional to $p(y|\boldsymbol{\theta})$ using Markov Chain Monte-Carlo (MCMC). From the MCMC-samples, the means and covariance matrix of the distribution parameters are estimated. The set of MCMC samples are increased in batches until three consecutive estimates of the means and covariances are within 1% of each other. This procedure is illustrated in Figure 4.3, for different number of data (n_{seeds} ST simulations) used to fit the distributions. The upper row of Figure 4.3 shows the "true" likelihood of the Gumbel-parameters under the observed data, the corresponding MCMC-samples, and the resulting best-fit Gaussian likelihoods. The second row shows the corresponding Gumbel-distributions, with 95% confidence intervals for the "true" and fitted Gaussian likelihoods. As expected, the uncertainty in the distribution parameters decrease with more data. So does the consistency of the Gaussian fit, which becomes much better for larger needs.

GP-model for distribution parameters The fitted Gaussian likelihood for the distribution parameters (i.e. the mean vector and covariance matrix) is then used to fit a GP model. In the following we consider the general case that the GP have m-dimensional output (i.e. models m distribution parameters $\boldsymbol{\theta} = (\boldsymbol{\theta}^{(1)}, ..., \boldsymbol{\theta}^{(m)}) \in \mathbb{R}^m$) and d-dimensional input (i.e. is a function of $\boldsymbol{x} \in \mathbb{R}^d$). In the present case $m = 2$ or $m = 3$ for the Gumbel and GEV

distributions, respectively.

That is, we consider a GP given as a prior over functions $\boldsymbol{\theta} : \mathbb{R}^d \to \mathbb{R}^m$:

$$\boldsymbol{\theta}(\boldsymbol{x}) \approx GP(\boldsymbol{\mu}(\boldsymbol{x}), K(\boldsymbol{x}, \boldsymbol{x})), \tag{4.2}$$

where the prior mean $\boldsymbol{\mu}(\boldsymbol{x}) = [\mu_1(\boldsymbol{x}), ..., \mu_m(\boldsymbol{x})]^T$ is here assumed zero, and where K is the diagonal matrix:

$$K(\boldsymbol{x}, \boldsymbol{x}) = \begin{bmatrix} K_1(\boldsymbol{x}, \boldsymbol{x}') & 0 & 0 \\ 0 & \ddots & 0 \\ 0 & 0 & K_m(\boldsymbol{x}, \boldsymbol{x}') \end{bmatrix} \tag{4.3}$$

where each K_j here is of the Matérn 3/2 type as in Gramstad et al. (2020). Given some training data, i.e. observed distribution parameters $\tilde{\boldsymbol{\theta}}_j = (\tilde{\theta}_j^{(1)}, ..., \tilde{\theta}_j^{(m)})$ for points $\boldsymbol{x}_j : D = (\boldsymbol{x}_j, \tilde{\boldsymbol{\theta}}_j)_{j=1}^N$ one can derive the posterior predictive distribution for "new" points under the observed training data. As described in section 4.2.2 the distribution parameters are assumed to come with Gaussian noise, so that $\tilde{\boldsymbol{\theta}}_j = \boldsymbol{\theta}(\boldsymbol{x}_j) + N(0, \Sigma_j)$, where Σ_j is the covariance matrix of each set of the m distribution parameters, as estimated using the procedure described in section 4.1.3.

Simulation of response from GP-model Given the GP-model that enables drawing random samples of the distribution parameters for any LT parameter $\boldsymbol{x}$, a "full" MC estimate of the response distribution is obtained. First, distribution parameters $\boldsymbol{\theta}_j$ are sampled from the GP-model for each LT condition $\boldsymbol{x}_j, j = 1, ..., 10000 \times 365.25 \times 24 \times 6$ in the 10 000-year LT simulation. Then, for each $\boldsymbol{\theta}_j$ a ST response y_j is sampled from the Gumbel- or GEV distribution $g_{Y|\boldsymbol{X}}(y|\boldsymbol{\theta}_j)$. From the 10 000 years of responses, the relevant return values are estimated.

Sequential update of the GP-model As described in Gramstad et al. (2020), a sequential update of the GP-model is applied, where a new point $\boldsymbol{x}_{new}$ for which to run new ST response simulations is selected based on a trade-off between increasing accuracy in the areas of the LT input space that contributes to the extreme response (here responses above the estimated 100-year level) and areas where the uncertainty is large. More specifically, the following acquisition function is applied

$$\boldsymbol{x}_{new} = \arg\max_{\boldsymbol{x}} f_s(\boldsymbol{x}) \left| \sigma_{\boldsymbol{\theta}(\boldsymbol{x})} \right|, \tag{4.4}$$

where $\boldsymbol{\sigma}_{\boldsymbol{\theta}(\boldsymbol{x})} = (\sigma_1(\boldsymbol{x}), ..., \sigma_m(\boldsymbol{x}))$ are the standard deviations of each of the distribution parameters as function of the LT variables $\boldsymbol{x}$, and $f_s(\boldsymbol{x})$ is the probability density function of responses above the 100-year return value, which is estimated using kernel density estimation.

This approach is illustrated in 4.4, which shows the acquisition function 4.4 used to select the new point to add to the GP-model.

Return period or failure probability estimation Once the GP model has been built, it can be used either to estimate the distribution of Y given a set of parameters $\boldsymbol{x}$, or to estimate a probability of failure by following the principles below.

The failure probability p_f defined in equation (3.1) can by written as

$$p_f = \mathbb{E}_{\mathrm{X},\rho}\left[\mathbb{P}_{Y|\mathrm{X}=\mathrm{x}}\left(Y > \rho\right)\right] \tag{4.5}$$

where

$$\mathbb{P}_{Y|\mathrm{X}=\mathrm{x}}\left(Y > \rho\right) = 1 - \mathbb{P}_{Y|\mathrm{X}=\mathrm{x}}\left(Y < \rho\right) = 1 - G_{Y|\boldsymbol{x}}(\rho) \tag{4.6}$$

with $G_{Y|\boldsymbol{x}}(\rho)$ the cumulative distribution function of $Y|\mathrm{X}=\mathrm{x}$. We thus have:

$$p_f = \mathbb{E}_{\mathrm{X}}\left[\int_{\Omega_\rho}\left(1 - G_{Y|\boldsymbol{x}}(\rho)\right) f_\rho(\rho) d\rho\right] \tag{4.7}$$

with f_ρ the pdf of the resistance ρ. The GP model provides the parameters of the CDF $G_{Y|\boldsymbol{x}}(\rho)$. Therefore the integral in equation 4.7 involves analytical functions and can be estimated with a simple 1D numerical integration.

4.1.4 Outcrossing approach in the joint ST-LT space

Mathematical formulation. In the following to alleviate notation, except the uncertain variables associated to the wind, all other variables associated to environmental conditions will be fixed. In this context, our goal is the estimation of the following failure probability

$$p_f^{year} = \mathbb{P}_{\overrightarrow{\xi},\nu_{\overrightarrow{\xi}}}\left(\max_{[0,n_T\times\Delta T]} s\left(t;\nu_{\overrightarrow{\xi}}\right) > \rho\right) \tag{4.8}$$

where

- n_T is the number of slices of $\Delta T = 10$ minutes in $[0,T]$ ($T = 60\times 10\times n_T$ seconds);
- $\overrightarrow{\xi} = \{\xi_i, i\in\{1,\ldots,n_T\}\}$ is a set of i.i.d. random vectors according to a reference random vector ξ. For each i, ξ_i gathers the LT environmental parameters defining the wind statistics over the i-th $\Delta T = 10$ minutes interval.;
- $\nu\left(.;\xi_i\right)$ represents the ST wind velocity. It is a 10min-stationary GP whose spectral density is parameterized by ξ_i;
- $\nu_\xi = \{\nu\left(.;\xi_i\right)\}_{i=1,\ldots,n_T}$ represents a random vector gathering the wind loads;
- ρ is the material resistance threshold;

The function s is the computationally costly output of a multi-physics (aero-hydro-servo-elastic) wind turbine simulator defined as:

$$s\left(t;\nu_\xi\right) = \sum_{i=1}^{n_T} s(t;\nu_{\xi_i}(t))\mathbb{1}_{I_i}(t). \tag{4.9}$$

where

- $s(.;\nu_\xi(.))$ is a piecewise supposed stationary random process representing the quantity of interest, output of a numerical simulator (Deeplines Wind^{TM}, DIEGO, HAWC2);
- $I_i = [(i-1)\Delta T, i\Delta T]$ with $\Delta T = 10$ min ;
- $\nu_{\xi_i}(t) = \left(\nu\left([0,t];\xi_i\right)\right)$ represents the wind velocity in a $[0,t]$ time interval.
- For fixed values of ξ_i, $s(.;\nu_{\xi_i}(.))$ is a 10 min-stationary random process ;

The statistical nature of ρ, ξ, $\nu\left(.;\xi_i\right)$ is described in section 4.2.1.

From time-dependent-reliability to standard reliability with the outcrossing approach. In the following only the LT and ST 3D wind parameters will be considered. The main formulation of the studied reliability problem involves the maximum of a piecewise stationary random process. We shall for a moment note $S(t)$, instead of $s\Big(t;\nu_\xi\Big)$, the output random process to alleviate notations. Let us consider S as a random process verifying appropriate smoothness hypothesis, for instance presented in Azäis and Wschebor (2009), such that the random one-dimensional Kac's counting formula defines the outcrossing (upcrossing) number as

$$N(\rho,T) = \lim_{\delta\to 0}\frac{1}{2\delta}\int_{[0,T]} S'^{+}(t)\mathbb{1}_{\{|S(t)-\rho|<\delta\}}(t)dt \tag{4.10}$$

$$= \int_{[0,T]} S'^{+}(t)\delta_{S(t)=\rho}dt \tag{4.11}$$

where the prime superscript denotes the time derivative of the function, $S'^{+}(t) = \sup(0, S'(t))$, δ stand for the Dirac function and $\mathbb{1}$ for the indicator function. The random instantaneous outcrossing, also named outcrossing rate, is defined as

$$N_\rho(t) = S'^{+}(t)\delta_{S(t)=\rho}. \tag{4.12}$$

The outcrossing rate mean is therefore given by

$$\mathbb{E}[N_\rho(t)] = \int_{\mathbb{R}} s' p(\rho, s'; t)ds' \tag{4.13}$$

where $p(.,.;t)$ stands for the joint probability distribution of the random vector $(S(t), S'^{+}(t))$. Another formulation, derived in the PHI2 approach, used for instance in Andrieu-Renaud et al. (2004) is given, under appropriate assumptions, by swapping integrals and limits in equation (4.10) and using the fact that for a realization of $(S(t), S'^{+}(t))$

$$\lim_{\delta\to 0}\frac{s'^{+}(t)\mathbb{1}_{\{|s(t)-\rho|\leq\delta\}}(t)}{2\delta} = \lim_{\Delta t\to 0}\frac{\mathbb{1}_{\{s(t-\Delta t)\leq\rho\}}(t)\mathbb{1}_{\{s(t+\Delta t)>\rho\}}(t)}{2\Delta t}.$$

Then the Andrieu-Renaud et al. (2004) formulation of the mean outcrossing rate boils down to

$$\mathbb{E}[N_\rho(t)] = \lim_{\Delta t\to 0}\frac{\mathbb{P}\Big(S(t-\Delta t)\leq\rho, S(t+\Delta t)>\rho\Big)}{2\Delta t} \tag{4.14}$$

and the mean outcrossing number to

$$\mathbb{E}[N(\rho,T)] = \int_{[0,T]}\mathbb{E}[N_\rho(t)]dt. \tag{4.15}$$

We can now come back to our setting. In our context, the piecewise continuous process S does not fulfill the required hypothesis on the full interval $[0,T]$ but only on the stationarity intervals of size $\Delta T = 10min$. However, by conditioning on ξ, using a simple complementary set argument and the i.i.d hypothesis on the ST processes ν_{ξ_i} conditional to the ξ_is, the failure probability over a year (4.8) can be written, similarly to (3.2), as

$$p_f^{year} = 1 - \mathbb{E}_\xi\Big[\Big(1-p_f(\xi)\Big)^{n_T}\Big] \tag{4.16}$$

with

$$p_f(\xi) = \mathbb{P}_{\nu_\xi}\Big(\max_{[0,\Delta T]} s\Big(t;\nu_\xi\Big) > \rho|\xi\Big). \tag{4.17}$$

For all t let us denote $s(t) = s\Big(t;\nu_\xi\Big)$ the process s conditioned on ξ and the outcrossing number on the interval $[0,\Delta T]$ by $N(\rho,\Delta T)$ given by (4.15) with the integral taken on the interval $[0,\Delta T]$ with integrant s. To alleviate notation, in the sequel we will not explicitly write the conditioning w.r.t. ξ in the probabilities. With the introduced notation, we moreover have

$$p_f(\xi) = \mathbb{P}_{\nu_\xi}\Big(s(0) > \rho\Big) + \mathbb{P}_{\nu_\xi}\Big(N(\rho,\Delta T) \geq 1, s(0) \leq \rho\Big).$$

For some values of the LT parameters the probability $\mathbb{P}_{\nu_\xi}\Big(s(0) > \rho\Big)$ will clearly be negligible. In this latter case

$$p_f(\xi) = \mathbb{P}_{\nu_\xi}\Big(N(\rho,\Delta T) \geq 1\Big). \tag{4.18}$$

Applying first the Markov inequality and then the stationarity hypothesis to (4.18)

$$\begin{aligned} p_f(\xi) &\leq \mathbb{E}_{\nu_\xi}\Big(N(\rho,\Delta T)\Big) = \int_{[0,\Delta T]} \mathbb{E}_{\nu_\xi}\Big(N_\rho(t)\Big)dt \\ &= \Delta T \mathbb{E}_{\nu_\xi}\Big(N_\rho(t_s)\Big). \end{aligned}$$

We can now use this bound within the expression (4.17) along with the i.i.d hypothesis of the LT parameters ξ which leads to

$$\begin{aligned} p_f^{year} &\leq \mathbb{E}_\xi\Big[1 - \Big(1 - \Delta T \mathbb{E}_{\nu_\xi}\Big(N_\rho(t_s)\Big)\Big)^{n_T}\Big] \\ &= T\bar{N} - O\Big(\Big(T\bar{N}\Big)^2\Big) \end{aligned} \tag{4.19}$$

with

$$\bar{N} = \mathbb{E}_\xi\Big[\mathbb{E}_{\nu_\xi}\Big(N_\rho(t_s)\Big)\Big]. \tag{4.20}$$

Another approximation can be obtained under mixing hypothesis on the random process S leading, on a stationarity interval, to the independence of its peaks and therefore a Poisson approximation of the associated outcrossing number such that using the stationarity hypothesis and for instance the Law of Large Numbers (LLN) we get

$$p_f^{year} \approx 1 - \mathbb{E}_\xi\Big(e^{-T\mathbb{E}_{\nu_\xi}[N_\rho(t_s)]}\Big). \tag{4.21}$$

We can notice that, on the LT scale, the hypothesis of independent peaks seems more relevant than in a short stationarity interval. But in the LT, because of the discontinuities, the outcrossing approach requires particular definitions and analysis. Nevertheless this should ends up with non-homogenous Poisson approximation and, with the i.i.d assumption on the ξ_is, to identical approximations unless failure at the initial time of each interval cannot be neglected.

Finally using Jensen inequality, switching the expectation $\mathbb{E}_\xi$ with the exponential in (4.21), we end-up with

$$p_f^{year} \leq 1 - e^{-T\bar{N}}. \tag{4.22}$$

Notice that both (4.19) and (4.22) are equivalent when the quantity $T\bar{N}$ is very small.

Following the work of Schall et al. (1991), Perdrizet and Averbuch (2011) proposed to use (4.21) in the general setting (4.8) and involved in addition a ρ uncertain parameter. After the same developments, they proposed to not apply Jensen approximation with respect to ρ leading to

$$p_f^{year} \leq 1 - \mathbb{E}_\rho\Big[e^{-T\bar{N}(\rho)}\Big]. \tag{4.23}$$

In our context, the main problem sums up to the estimation of the quantity $\bar{N}$ defined in (4.20), with fixed ρ, as

$$\bar{N} = \mathbb{E}_\xi\Big[P_\rho^+(t_s;\xi)\Big]$$

with

$$P_\rho^+(t_s;\xi) := \mathbb{E}_{\nu_\xi}\Big(N_\rho(t_s)\Big) = \lim_{\Delta t\to 0} \frac{\mathbb{P}\Big(S(t_s-\Delta t;\nu_\xi) \leq \rho, S(t_s;\nu_\xi) > \rho\Big)}{\Delta t}. \tag{4.24}$$

We can further notice that at this stage the time dependent reliability problem has been reformulated into a time-independent one thanks to the stationary assumption.

We will now on consider the LT parameter fixed and simplify notation such that ν_ξ defined on the 10-minutes interval will just be denoted ν and $P_\rho^+(t_s;\xi)$ simply $P^+(t_s)$ when ξ is fixed. We can also notice that for a chosen small enough value of Δt, we wish to estimate the numerator in the limit term which can be reformulated as $\mathbb{P}\Big(h(\nu) < 0\Big)$ with $h(\nu) = \max\Big(S(t_s-\Delta t;\nu) - \rho, -S(t_s;\nu) + \rho\Big)$. Using the Karuhnen-Loève (KL) representation of the ST wind coupling (4.30) with (4.28) such that ν is fully characterized by the set of random vector α^{KL} denoted to alleviate notation α, the estimation of $P^+(t_s)$ boils down to estimating the probability

$$\mathbb{P}\Big(h(\alpha) < 0\Big) = \mathbb{E}_q[\mathbb{1}_{h(\alpha)<0}] \tag{4.25}$$

where q is the probability density of the high dimensional ($M_{KL} = 168$) random vector α. Since we assume that $\{h(\alpha) \leq 0\}$ is a rare event (i.e., $P^+(t_s) \leq 10^{-4}$), performing standard MC simulation can be prohibitively expensive i.e. we require a large number ($\propto 10^2 P^+(t_s)$) of i.i.d. samples $\alpha_i \sim q$ for an accurate estimation of $P^+(t_s)$.

In our setting the input distribution is a standard Gaussian $\alpha \sim \mathcal{N}(0, I_D)$. In the case of non-Gaussian distributions, iso-probabilistic transformation are commonly used prior performing rare event probability estimation via Rosenblatt or Nataf transformations (Rosenblatt, 1952; Nataf, 1962; Lebrun and Dutfoy, 2009a,b)).

4.2 Benchmark on a simplified 2D case study

4.2.1 2D Benchmark Case Study

Response calculations for different environmental conditions are performed with Hipersim (https://gitlab.windenergy.dtu.dk/HiperSim/hipersim), used to generate turbulence wind

box, and a mNARX surrogate model based on the combination of dimension reduction and auto-regressive modelling developed by ETH Zürich (Schär et al., 2023). This model is described in HIPERWIND deliverable D4.1 (Dimitrov et al., 2022), and has been trained from OpenFAST (NREL, 2021) simulations of the NREL (National Renewable Energy Laboratory) 5MW reference wind turbine (Jonkman et al., 2009). It takes a wind box as input and returns the corresponding maximum flapwise blade root bending moment M_y^{Bld}. Two case studies are considered, with offshore wind turbines at two different locations, i.e. Teesside and South of Brittany. For both cases, joint statistical models for the relevant input variables were taken as given, as described in (Kelly and Vanem, 2022; Vanem et al., 2023). Note, however, that the statistical models were initially fitted to higher-dimensional data, but only mean wind speed and turbulence are considered in this study. The fitted omni-directional joint distribution at Teesside, not documented in previous references for confidentiality reasons, is considered for the 2-dimensional exercise with the following parameters:

- Mean wind speed (U): 10-minute average horizontal wind speed at hub height (83 m).
- Turbulence (σ_U): the temporal standard deviation of the wind speed at hub height.

This has been fitted based on measurements over a period of four years. The fitted omni-directional joint distribution at South Brittany (Vanem et al., 2023) is considered for the 2-dimensional exercise with the following parameters:

- Mean wind speed (U): 1-hour average horizontal wind speed at hub height ($150m$). This is obtained by down-sampling 10-minute average horizontal wind speed to match the hourly wave conditions for the full joint distribution model.
- Turbulence (σ_U): the temporal standard deviation of the wind speed at hub height for same duration than U.

This distribution is fitted to hindcast data from the ANEMOC (Digital Atlas of Ocean and Coastal Sea States) database[2], covering 32 years of data from the years 1979 to 2010. It should be noted that these data do not include the turbulence variable, σ_U, and therefore a conditional distribution for turbulence, conditioned on mean wind speed, was established based on the normal turbulence model described in (IEC, 2019a), i.e., a conditional lognormal distribution as also outlined in (Vanem et al., 2023). It should be noted that the ETH response model has been trained on the NREL $5MW$ turbine whose hub is at $90m$, and the mean wind speed U is not translated to the hub height $90m$ in this exercise. Hence, the actual response estimates cannot be used directly, but this is deemed appropriate for a comparison exercise, as long as the same wind input is used in all cases that are to be compared. The response model is only applicable between the cut-in speed ($3m/s$) and cut-out speed ($25m/s$), so sets of random variables with mean wind speed U below cut-in wind speed or above cut-out wind speed were discarded. However, these conditions are not assumed to contribute to the LT extreme responses for these turbines, so this is deemed reasonable.

In the following, extreme maximum flapwise root bending moment corresponding to a return period of 50 years will be computed using both environmental contours and a sequential sampling approach for the two case studies. The two approaches assumes the same

[2]URL: http://anemoc.cetmef.developpement-durable.gouv.fr/

statistical distribution for the wind variables, and the same models for the response calculations, as outlined above. However, one critical assumption is implicit in the environmental contours approach. Indeed, this approach assumed that the largest responses occur in the most severe environmental conditions. In other words, it assumes that the effect of the LT variability of the wind conditions is more important for the extreme response than the ST variability of the response condition on wind conditions. This need not be assumed with the sequential sampling approach, and this study will shed some light on the appropriateness of this assumption for the offshore wind response cases.

4.2.2 2D results with Environmental Contours

Teesside To estimate the extreme response of the wind turbine at Teesside, the 2-dimensional environmental contour method based on DS (direct sampling) (Huseby et al., 2013, 2015) and IFORM (inverse first-order reliability method) (Winterstein et al., 1993; Haver and Winterstein, 2009) is considered. The predefined surrogate model of deliverable D4.1 Dimitrov et al. (2022) is used to calculate the ST extreme response (i.e. maximum flapwise blade root bending moment M_y^{Bld}). Environmental contours corresponding to n-year extreme of 10-minute conditions are calculated, i.e. corresponding to an exceedance probability of

$$P_e = \frac{1}{365.25 \times 24 \times 6 \times n} \tag{4.26}$$

For 50-year return period $n = 50$ and $Pe = 3.8E-07$. The DS and IFORM environmental contours based on the fitted omni-directional joint distribution at Teesside are shown in 4.5 for 1-year and 50-year return periods. One immediate observation is that the contours from the different contouring methods are quite similar, with only slight difference for both the 1-year and 50-year extreme conditions. The points on the 50-year return period contours are taken as input for the surrogate model (mNARX). There are 68 input points from the 50-year DS-contour, and 40 input points from the 50-year IFORM-contour. In total 1000 seeds are run with mNARX (10-minute simulation) for each input point on both the DS-contour and IFORM-contour. However, points corresponding to wind conditions below the cut-in wind speed ($3m/s$) and above the cut-out wind speed ($25m/s$) are disregarded. The response model is not applicable for these conditions, and it is tacitly assumed that these conditions will not contribute to the LT extreme response. Hence, for wind conditions outside the operational range of the wind turbine, the response is simply set to a zero. It is noted that the mNARX model sometimes gives NaN (not a number) for certain seeds for some wind conditions. This is most likely due to negative or extremely high instantaneous winds speeds since this model is not trained neither at negative wind speed nor at extremely high wind speeds. This could occur for example for a combination of high mean wind speed and high turbulence, remembering that the turbulence wind generator used (Turbgen of HIPERSIM Dimitrov (2023)) create a realization of a 3D Gaussian process. In such cases, another seed is simply selected to avoid that mNARX gives NaN. The LT extreme responses of maximum flapwise blade root bending moment (50% fractile, 90% fractile, 99% fractile of the ST distributions) are taken out from 1000 seeds based on 50-year DS and IFORM contours, respectively. That is, for each wind condition along the contours, $N = 1000$ response simulations are performed, and the distribution of maximum responses from these 1000 simulations are used to extract the quantiles of interest. According to (DNV, 2021), the choice of quantile is highly case-dependent, and there are no definitive recommendations on which quantile to use. Hence, results for three different quantiles are reported. The

results are listed in 4.1. It appears that the LT extreme estimations of flapwise blade root bending moment are comparable for the two contour methods when considering the 50% fractile, i.e., 20.59 MNm using the DS contours and 20.40 MNm from the IFORM cotours, with similar combination of mean wind speed (U) and turbulence (σ_U). The results are also close for the 90% fractile based on these two approaches, i.e., 25.85 MNm from the DS approach and 25.17 MNm from the IFORM with similar combination of mean wind speed and turbulence. As for the results from 99% fractile, even though the extreme responses do not differ too much, i.e., 34.01 MNm from the DS approach and 34.96 MNm from IFORM, the combination of mean wind speed and turbulence is quite different, i.e., the mean wind speed leading to the extreme response according to the DS approach is 22.74 m/s and the corresponding turbulence is 5.17 m/s while the mean wind speed leading to the extreme response for IFORM is 13.14 m/s and the corresponding turbulence is 5.30 m/s. According to DNV-RP-C205 (DNV, 2021), extreme values in a random process are random variables with a statistical variability. Generally the relevant factor and fractile will be larger for strongly nonlinear problems, and an appropriate high fractile should be chosen for the characteristic LT response. The appropriate fractile level is case-specific, and a fractile in the order of 85% to 95% will often be a reasonable choice for use in design. In this exercise, the results from the contour method will later be compared with results from brute force simulations in order to consider which quantile levels are most appropriate.

Direct sampling		
U [m/s]	σ_U [m/s]	M_y^{Bld} [MNm]
12.66	5.33	20.59 (50% fractile)
14.56	5.36	25.85 (90% fractile)
22.74	5.17	34.01 (99% fractile)
IFORM		
U [m/s]	σ_U [m/s]	M_y^{Bld} [MNm]
13.14	5.30	20.40 (50% fractile)
14.51	5.30	25.17 (90% fractile)
13.14	5.30	34.96 (99% fractile)

Table 4.1: Long-term extreme responses of flapwise blade root bending moment M_y^{Bld} [MNm] with estimated 50-year return period based on DS and IFORM, respectively. Teesside case.

Figures 4.6 to 4.8 show the 50-year DS-contour and the corresponding LT extreme response of the maximum flapwise blade root bending moment by using 50% fractile, 90% fractile and 99% fractile of the ST extreme response distributions, respectively. The rainbow color denotes the range of the maximum value and the blue cross denotes the combination of the wind speed and turbulence leading to the maximum flapwise blade root bending moment on the 50-year DS-contour.

Figures 4.9 to 4.11 show the 50-year IFORM-contour and the corresponding estimated LT extreme response of the maximum flapwise blade root bending moment by using 50% fractile, 90% fractile and 99% fractile, respectively, of the ST maximum response distri-

bution. The rainbow color denotes the range of the maximum value, and the blue cross denotes the combination of the wind speed and turbulence leading to the maximum flapwise blade root bending moment on the 50-year IFORM-contour. It is observed that for both contour methods, the response tend to be largest for relatively moderate mean wind speeds around 12 - 15 m/s, but that it tends to grow with turbulence and gets its largest values for the highest values of turbulence.

South Brittany To estimate the extreme response of the wind turbine at South Brittany, 2-dimensional environmental contours based on IFORM (inverse first-order reliability method) is considered for the mean wind speed and turbulence variables. The predefined surrogate model of deliverable D4.1 Dimitrov et al. (2022) is used to calculate the ST extreme response (i.e. maximum flapwise blade root bending moment M_y^{Bld}) in selected wind conditions. Environmental contours corresponding to n-year extreme of 1-hour conditions are calculated, i.e. corresponding to an exceedance probability of:

$$P_e = \frac{1}{365.25 \times 24 \times n} \tag{4.27}$$

For 1- and 50-year return period ($n = 1, 50$), $P_e = 1.14E-04$ and $2.28E-06$, respectively. The IFORM environmental contours based on the fitted omnidirectional joint distribution at South Brittany are shown in 4.12 for 1- and 50-year return periods. The points along the 1- and 50-year IFORM contours are taken as input for the surrogate model (mNARX). There are 94 input points from the 1-year IFORM-contour, and 74 input points from the 50-year IFORMcontour. In total 100 seeds are run with mNARX (1-hour simulation) for each input point on the IFORM-contours. The LT extreme responses of maximum flapwise blade root bending moment (50%, 90% and 99% fractiles) are taken out from 100 seeds based on 1- and 50-year IFORM contours, respectively. The results are listed in 4.2. Note that the 99% fractile should be used with caution since these results are based on only 100 seeds and the 99% fractile estimate is therefore not very reliable. Notwithstanding, the results are included in the table, and the estimates corresponding to the 90% fractile are presented in bold, since this seems to be the most reasonable choice.

The LT extreme estimations of flapwise blade root bending moment from the 50-year contour is slightly higher than the LT extreme estimations of flapwise blade root bending moment from the 1-year contour, assuming the 99% fractile, i.e., 15.87 MNm from 1-year contour and 16.54 MNm from 50-year contour with similar combination of mean wind speed and turbulence. Figures 4.13 and 4.14 show the 1- and 50-year IFORM-contour and the corresponding LT extreme response of the maximum flapwise blade root bending moment by using 99% fractile, respectively. The rainbow color denotes the range of the maximum value, and the blue cross denotes the combination of the wind speed and turbulence leading to the maximum flapwise blade root bending moment on the IFORM-contour.

4.2.3 2D results with BNN

Aeroelastic simulations are relatively time-consuming, which becomes an important challenge when dealing with large samples such as in reliability problems considering small probabilities. If a simplified (surrogate) model can effectively replace the aeroelastic simulations, it will lead to significant savings of computational efforts. A surrogate model trained by a least-squares or a max-likelihood fit will typically perform well in predicting the

IFORM - 1year		
$U[m/s]$	$\sigma_U[m/s]$	M_y^{Bld} [MNm] (1-h)
11.11	2.57	14.95 (50% fractile)
11.11	**2.57**	**15.87 (90% fractile)**
10.63	2.53	16.88 (99% fractile)
IFORM - 50 year		
U [m/s]	σ_U [m/s]	M_y^{Bld} [MNm] (1-h)
13.31	3.04	15.53 (50% fractile)
12.69	**2.99**	**16.54 (90% fractile)**
13.31	3.04	17.54 (99% fractile)

Table 4.2: Long-term extreme responses of flapwise blade root bending moment M_y^{Bld} [MNm] based on 1- and 50-year IFORM contours, respectively. South Brittany case.

main bulk of the dataset. However, its performance in predicting the tails is not guaranteed as the extreme behavior may follow a different distribution.

In order to test the possibility of replacing the aeroelastic simulations with the BNN surrogate model discussed briefly in 4.1.2, we tested the performance of the BNN model in predicting the tails of aeroelastic load distributions. For the purpose, we carried out a large number of simulations (2×10^6 samples in the 2D input space with mean wind speed and turbulence as input variables) with the mNARX blade load time series simulator. The mNARX model is convenient for such a study as it provides time series with strong similarity to actual aeroelastic simulations, but at a small fraction of the computational cost. A BNN model (see Section 4.1.2) assuming jointly Gaussian distributed parameters was fit to 50,000 of the samples. The BNN considered both model uncertainty (variational layers) and aleatoric uncertainty (output is in terms of distribution parameters). The BNN was used to predict blade root flapwise moments for all input samples, and the tail distribution (in terms of exceedance probabilities) was compared to the tail distribution of the simulated data. The comparison is shown in Figure 4.15. It is clear that the behaviour predicted by the BNN is heavily dictated by the choice of distribution (Gaussian in this case), while the blade load tail distribution seems to deviate from a Gaussian distribution. Due to this, we concluded that our current implementation of BNNs would be helpful when considering the bulk of the data (such as in e.g. fatigue analysis) but it is not suitable for problems when the far tail of the data needs to be modelled accurately. Based on some additional tests, we determined that other implementations with more flexible output distribution assumptions (such as e.g. a Gamma distribution) could provide better performance but ultimately a different modelling approach was taken, using sequential sampling.

4.2.4 2D results with GP and sequential sampling

In the following, results from the sequential sampling approach are presented in terms of the 50- and 100-year return values, which in the following are estimated as in the distribution of the annual maximum response, respectively. The empirical distribution of the annual

maximum response is, as explained above, estimated from a 10 000-year simulation in each iteration of the sequential sampling approach. In addition, the failure probability p_f^{year}, defined as the annual probability that the response exceeds $27.112MNm$ is considered.

Brute-force results In order to have a reference to which to compare the sequential sampling results, brute-force estimations of the 100-year return value for M_y^{Bld} were carried out, through a direct MC approach. While, the mNARX surrogate model is too computationally expensive to carry out an intensive sample of the full 10 000-year period, a reliable estimate could be obtained by excluding LT conditions from which there are none or very small contribution to the 100-year return value. Two set of brute-force samples were carried out, applying two different truncations of the LT distribution, as summarized in 4.3. Effectively, the truncation of the LT distribution can be viewed as a simple form of importance sampling where it is implicitly assumed that responses outside the cutoff regions are zero. Hence, only return levels for which there are minor contribution from the discarded LT conditions could be reliably estimated. However, as seen from Figure 4.16, this is a valid assumption for M_y^{Bld} larger than about 26.0. Hence, it is believed that the 100-year return value of 27.112 MNm, as obtained from the 10 000-year of samples is a reasonable accurate estimate. The estimate based on 1 000 year of data is obviously even less affected by the truncation of the LT distribution, but more affected by statistical uncertainty.

duration [years]	cutoff U [m/s]	cutoff σ_U [m/s]	100-year M_y^{Bld} [MNm]	50-year M_y^{Bld} [MNm]
1 000	3.0	5.0	26.334	24.649
10 000	3.5	8.0	27.112	25.093

Table 4.3: Overview of the brute-force estimation of the 100-year return value for the response M_y^{Bld}.

Sequential sampling results As described in section 4.2.2, the GP-model represents the distribution parameters in the distribution of the 10-minute maximum response. The distribution parameters are fitted based on n_{seeds} 10-minute simulations. Different distribution models and different number of seeds (i.e. number of 10 minute response simulation) were tested. Below results for the Gumbel distribution for 6, 18 and 90 seeds (i.e. 1-hour, 3-hours and 15-hours of response simulations in each LT condition) and the GEV distribution for 18 and 90 seeds are reported. The results, in term of estimated 100- and 50-year return values as well as failure probability p_f, as function of the number of ST simulations (i.e. the number of LT conditions used to train the GP) are shown in Figure 4.17. As seen from this figure, the estimated 50- and 100-year return values converges to values in relatively good agreement with the brute-force results within 10-20 iteration of the sequential sampling approach. For the case using the GEV-distribution with $n_{seeds} = 18$, the convergence is somewhat slower, which can be explained by the fact that large uncertainties in the distribution parameter estimates (i.e. large variation when sampling distribution parameters from the GP leads to large variations of the responses). Compared with the environmental contour estimates, it is observed that assuming the 90% quantile of the ST response distribution, contour estimates agree reasonably well with the brute-force and the

sequential sampling approach. Assuming the 99%-quantile significantly over-estimates the 50-year extreme response, whereas assuming the median response leads to a significant under-estimation of the extreme response. However, the 90%-quantile agrees well, with only a slight over-estimation of the response, which corresponds to slightly conservative designs.

As shown in the top-right picture of Figure 4.17, the annual failure probability converges with more difficulty toward a value slightly underestimating the reference obtained with Brute force sampling. To investigate what could explain this bias, let's try to check the distribution of points in the LT space, after 50 enrichments (Figure 4.18). The points seem well distributed according to the enrichment criterion shown on the right picture. Another possibility may be due to some outliers complicating the Gumbel fitting of ST maxima. Indeed, this assumption is confirmed in several examples of exceedance curves shown in Figure 4.18 where outliers are highlighted by surrounding circles. The origin of such outliers in the max quantity predicted by mNARX surrogate have not been identified by lack of time but may probably due to an application of mNARX out of its training domain, which is also justified by some points giving Not a number (Nan) outputs. We assume in the following that such problem will not appear when using physical simulators of offshore wind turbine dynamics and consider the Sequential Sampling method to be the most efficient for computing stationary ULS reliability.

Results South Brittany For the South Brittany case the results of the sequential sampling are shown in Figure 4.20. Here, only the Gumbel distribution was considered. Note also that for South Brittany the period over which the LT variables (U, σ_U) are assumed stationary is one hour, so that e.g. $n_{seeds} = 3$ in Figure 4.20 corresponds to running three one-hour response simulations. The Gumbel distribution was, however, still fitted to 10-minutes maximum responses as for Teesside. That is, each one-hour response time series was split in six 10-minutes parts, from which the 10-minute maximum values were extracted. It is interesting to note that for South Brittany the contour approach underestimates the 50-year return value significantly. It is likely that is due to the fact that the main contribution to the 50-year response is coming from LT parameters well inside the contour. Hence, this represents a situation where extreme ST responses in relatively common LT conditions dominates the extreme response. This is illustrated in Figure 4.21, which shows the area in the LT plane that have responses exceeding the 50-year return level. It is observed that for Teesside, the LT conditions giving rise to extreme responses are much closer to the contour lines compared to South Brittany. It is not clear exactly why the ST variability is so much more dominating in the South Brittany case. It could either be due to specifity in the wind parameter joint distribution, or to the longer runtime of simulations (1h instead of 10min).

4.2.5 2D results with the outcrossing approach in the joint ST-LT space

The mNARX model output. For reasons of time limitations, the stationary case analysis will be carried out with the surrogate mNARX model developed by the partner ETH-Zurich in WP4 (Schär et al., 2023). The mNARX model considers LT and ST wind conditions as inputs. The output of the mNARX model at time t: $S(t;.)$, is a function of the discretized (y, z) windbox sections from time 0 up to the largest discretization time below t. Before the output calculation, each 19×19 (y, z) section is represented with a discrete cosine transform (DCT) and only the 16 lowest frequency components are kept. Therefore the DCT is a

sum of 16 cosines, 4 for each dimension (y, z) with period $2 \times 19/i$ with $i = 1, ..., 4$ such that the highest frequency correspond to a period $19/2$ which covers half the discretized dimension. In order to not eliminate any frequencies, the discretization must be fine enough to retain at least 4 points for each y and z dimension (which means we have at least 2 points to correctly identify the highest frequency cosine). We could therefore have used an even coarser discretization in y and z (at least 5×5).

Stationary Wind spectral representation. Wind space-time series are generated with the HiperSim tool box (Dimitrov, 2023) by combining multi-dimensional Fourier basis and Gaussian coefficients with variances derived from the Mann spectral density (Mann, 1998). This description of the wind is called in the literature spectral representation. We will consider a Mann spectrum combined with two dependent LT parameters $\xi = (U, \sigma_U)$ which are the time average mean speed and its related standard deviation measuring the turbulence. The ST wind representation and the LT parameters are supposed independent such that on a 10-min interval the wind field, in the turbine direction, is represented as:

$$\nu(t, y, z; \xi) = U \times \mathcal{U}(y, z) + \sigma_U \times \nu_F(tU, y, z) \tag{4.28}$$

where $\mathcal{U}(y, z)$ is the vertical wind shear, ν_F is a zero mean stationary GP with Mann spectral density: $\mathcal{M}(\omega)$ such that:

$$\nu_F(x, y, z) = \sum_{i=1}^{M_F} \alpha_i^F \psi_i^F(x, y, z) \tag{4.29}$$

where for $i = 1, ..., M_F$ the set of α_i^F are the so-called ST parameters such that $\alpha_i^F \sim \mathcal{N}(0, \sigma_i^2)$ with $\sigma_i^2 = \mathcal{M}(\omega_i)d\omega_i$ and $d\omega_i = \omega_i - \omega_{i-1}$. The set of functions ψ_i^F are the 3d Fourier basis at frequency ω_i (Shinozuka and Deodatis, 1991).
Given ξ the variance of ν will be expressed as $\sigma_U^2 \times \sigma_{Mann}^2$ where σ_{Mann}^2 is supposed to be one. Nevertheless we can notice that the covariance of ν will also involve the U quantity with an expression that is not straighforward.
With the introduced wind representation, the stationary part of the wind on a 10 minutes interval is independent of the LT parameters ξ and is characterized by M_F ST random parameters of the order of several hundreds.
In order to construct the space-time wind (4.28) from a 3D-space wind ν_F independent of the sampled U we considered a maximum mean wind speed of $25m/s$ such that with the maximum time of $75s$ the x component is defined on the interval $[0m, 1875m]$ (with upper bound calculated by the product $25 \times 75 = 1875m$). The discretization in the x dimension is of 1501 points (for $75 \times 20 + 1$). The y variable is defined on the interval $[-68.5m, 68.5m]$ with a discretization of 19 points and the z variable on the interval $[14m; 151.5m]$ with also 19 discretization points.

Unsupervised wind dimension reduction: Karhunen-Loève (KL) expansion. In order to achieve the reliability analysis in our time variant setting, discretizing the wind into thousands of wind values leads to a high dimensional representation which will face any method to the curse of dimensionality (Taylor, 1993; Zimek et al., 2012). We need to have access to a reduced parameterization of the wind generation. Instead of manipulating the spectral representation implemented in HiperSim, we used a non-intrusive approach with KL expansion (Loève, 1978; Wang, 2008) of the wind learned on a set of samples from

HiperSim. This latter will enable the access to a size-controled parameterization of the wind box to be involved in the reliability analysis.

It is known that the spectral representation and the KL expansion are equivalent for stationary random processes with infinite support (Huang et al., 2001). On finite support, to achieve a given level of variance explanation, the perfectly estimated (for instance with an analytical solution to the Fredholm equation) KL expansion will require less coefficients than the spectral representation (Huang et al., 2001). When the covariance is estimated well enough, the KL still requires in general less coefficients in the representation for a given accuracy and in particular the more irregular the process, the smaller the number of coefficients is required in comparison to the spectral representation (Huang et al., 2001).

To reduce the number of ST parameters, we propose a KL representation on a smaller time interval than the initial 10 minutes wind stationarity. Indeed we assume that the simulator output will inherit the stationary character of the wind input as a measurable non-linear function of a stationary random process despite some loss of stationarity due to the KL truncation. The stationarity assumption will be discussed in the next paragraph. We estimate the KL expansion of ν_F from $N = 1000$ Mann simulated winds of $t_0 = 75$ seconds with HiperSim such that

$$\nu_{KL}(x, y, z) = \sum_{i=1}^{\hat{M}_{KL}} \alpha_i^{KL} \sqrt{\hat{\lambda}_i} \hat{\psi}_i(x, y, z). \tag{4.30}$$

where $\alpha_i^{KL} \sim \mathcal{N}(0, 1)$ with the $\hat{\lambda}_i$s and $\hat{\psi}_i$s respectively the estimated eigen values and eigen functions involved in the Fredholm equation to be solved in the KL expansion representation (Wang, 2008). The number of kept terms in order to explain 75% of the variability of the initial process ν_F is $\hat{M}_{KL} = 139$. A similar analysis was carried out on an interval of $100s$ leading to $\hat{M}_{KL} = 168$ terms kept to explain the same 75% of the variability. These different estimators are obtained using the SVD approach from OpenTURNS software Airbus-EDF-IMACS-ONERA-Phimeca (2024) which enables the computation of a 3D KL expansion and presented fastest estimations and predictions on a few comparison with others estimation approaches such as the projection approach used in the package fda from R.

We can notice that a KL approach constructed on simulated series with varying LT and ST parameters would give as output non-Gaussian coefficients encompassing the randomness of both LT-ST parameters and disabling the possibility to discriminate the LT from the ST values in a KL simulated wind. For instance it will not be straightforward to find the LT-ST wind representation corresponding to the design point found in the corresponding KL-coefficients space. Nevertheless, putting aside high-dimensional setting issues, the failure probability could still be estimated in this manner. This difficulty is avoided in this work thanks to the independence of the Mann spectral density, characterizing the ST wind, with the LT parameters ξ. It would by contrast be encountered if one use the Kaimal spectrum with NREL TurbSim turbulent wind generator (Kelley and Jonkman, 2007).

Discussion on the stationarity hypothesis When truncated and estimated the KL expansion of a stationary random process loses to some extend the stationarity property as has been demonstrated numerically in Ghanem and Spanos (1991); Field and Grigoriu (2004); Grigoriu (2006); Stefanou and Papadrakakis (2007); Chen et al. (2018). We also confirmed the loss in stationarity with the KL representation of the wind input GP which

implies a loss in stationarity of the output. To display the level of stationarity loss on the flapwise blade root moment, from a wind spectral representation and its estimated KL expansion, we compare the respective output means in Figure 4.22, variances in Figure 4.23 and covariances between $S(t)$ and $S(t+h)$ as a function of t for different lags h in Figure 4.24, 4.25 and 4.26. For fixed $(U, \sigma_U) = (10m/s, 1m/s)$, we sample a thousand ST wind configurations from both spectral and KL representations. The output is then obtained with mNARX and the statistics are estimated on the thousand output samples for both cases. We can notice differences between the variance and covariances obtained from the KL and spectral version of the wind. The order of magnitude could be acceptable for the analysis. Nevertheless, we can clearly notice that overall the estimated mean, variance and covariances are not constant as should be. A first obvious factor that could explain part of this variations from constant is the size of the sample. It could be increased to refine the statistics estimators but the small impact would not explain such variations. Another possible factor could come from the mNARX model which as been trained on winds with different LT parameters and 10 minutes ST generated from a Kaimal (Dimitrov et al., 2022) and not a Mann spectrum. The behavior with respect to stationarity of the mNARX model have not been assessed and seems to us the first source of loss of stationarity. On a real simulator, stationarity must also be assessed since the blade pitch and torque controller might involve discontinuities in the output with respect to the environmental condition inputs and therefore potential loss in stationarity in some areas of the inputs space. Otherwise, if the output behaves continuously w.r.t. the environmental conditions then stationarity can be assumed. From now on, we will consider the output stationary and keep in mind that the results might be altered in practice when using the mNARX model.

We also have to take into consideration the fact that the output time series at time t will depend on the environmental conditions within the interval $[0, t]$ and not only at time t. Therefore under the hypothesis of stationary inputs, the stationary regime expected on the output will require a transition period between the structure being set in motion and the moment it reaches its steady state. The analytical optimal t_s value is not derivable since it depends on the non-linear multi-physics behavior of the black-box numerical simulator but numerical experiments showed that considering the output stationary from $t_s = 75$ seconds or 100 seconds seemed reasonable.

Idea to reduce the loss in stationarity induced by KL based wind. In order to mitigate the truncation impact on the approximation we multiplied the KL expansion by a constant term in order to correct the truncation error. But tuning this parameter by hand is not straightforward. In Chen et al. (2018) (for a one dimensional random process) a modified KL expansion is proposed in order to reduce the loss in stationarity and ergodicity involved by the KL truncation and estimation. They showed that a proper KL correcting factor should depend on t and proposed as correcting factor the inverse of the time dependent KL truncated standard deviation. This latter result would seem to indicate, that a good constant correction factor could be the inverse of the integrated KL truncated standard deviation. We did not implement this strategy in this preliminary work. In futur work, in light of the results in (Chen et al., 2018), quantifying the impact of the KL truncation on the estimated probability or at least on the associated reliability index might be recommended.

Outcrossing method results and challenges. In the PHI2 approach of Andrieu-Renaud et al. (2004), with only ST parameters, a FORM approximation is used. Our initial aim

was to extend the PHI2 approach with joint LT and ST uncertainties as in Perdrizet and Averbuch (2011). Nevertheless the optimisation task involved for the Design Point (DP) estimation happened to be too difficult since all tested optimizer failed to converge to any reasonable solution. The optimizer delivered for instance the design point presented in Figure 4.27 with its associated output in Figure 4.28. The design point norm is approximately 9.3 which corresponds to an approximate mean outcrossing rate in the joint space $\bar{N}$ of the order of 10^{-20} which seems far too low. By setting aside the high dimensional geometry issue to be discussed in the next subsection, two main factors have been detected that could explain the difficulty.

First since we are seeking for a failure event at a specific time t_s, we can anticipate that a small change in the ST-LT parameters might change the configuration from failing to reliable at the given time, meaning that the failure area is not a nice connected set and therefor making the optimization favourable to multiple local minima. Also a main issue is the lack of identifiability between the LT parameter and the ST one. For instance the LT variance term and the ST coefficients can not be distinguished in the optimization process since they multiply themselves in the problem formulation (4.28)-(4.29). In that context, the optimizer seems to get stuck or does not converge in a reasonable number of simulations.
A second issue is the lack of confidence we can have on mNARX responses when more extreme parts of the ST-LT space are explored in the optimization (same remark holds if FORM is performed only w.r.t ST parameters). Indeed, for this work, mNARX has been trained on a limited number of non-extreme set of parameters (Dimitrov et al., 2022). To mitigate the first issue, a two step strategy is proposed (the second issue is put aside in the following since extreme prediction errors are expected to be negligible with a real simulator). We will begin by performing the FORM analysis only w.r.t. the ST parameters for fixed LT. Since each FORM analysis is costly, a Kriging metamodel can be built between the LT parameters and the FORM estimations. For this purpose, the FORM analysis with only the ST parameters should be carried out multiple times according to a DoE of LT parameters values.

We introduce here a new algorithm presented in (Cousin et al., 2024) and called MAKSUR standing for Mean Estimation with an Active Kriging based on a Stepwise Uncertainty Reduction approach. This algorithm dedicated to the computation of expectations, uses a sequential sampling with an enrichment function derived from SUR approach Bect et al. (2012). The DoE of LT parameters values is then composed of an initial DoE to be enriched with this MAKSUR algorithm. Finally the expectation with respect to the LT distribution would be estimated with a direct MC method coupled to the learned surrogate As will be explained below, we stopped at the ST-FORM stage since the standard FORM analysis in high dimension can not be fully trusted in particular in this multiple local minima setting. Suggestion of alternatives to the standard form will also be discussed.

Using the previously introduced notations we seek for the bound

$$p_f^{year} \leq T\bar{N}$$

with $\bar{N} = \mathbb{E}_\xi\left[P_\rho^+(t_s;\xi)\right]$ and $P_\rho^+(t_s;\xi)$ given in (4.24) with ρ fixed for this analysis to $27112\ kNm$ and stationarity supposed reached at t_s to 75 or 100 seconds. The first key step consists in performing the FORM analysis for fixed LT i.e. estimating $P_\rho^+(t_s;\xi)$ for

fixed ξ. The task involves a high-dimensional input vector because of the ST wind high frequency representation encoded in its KL expansion. We will now focus on the FORM analysis in high dimension. We first need to solve the FORM design point research problem:

$$\alpha^*(t_s) = \underset{\alpha \in \mathbb{R}^{\hat{M}_{KL}}}{\arg\min} \|\alpha\| \qquad \text{subject to} \qquad s(t_s, \alpha) \geq \rho \tag{4.31}$$

where $s(t_s, \alpha)$ is the model output at some given time t_s (100 seconds in the following FORM result) obtained from a wind input represented by its KL coefficient vector α. Indeed, following the work of Koo et al. (2005); Jensen and Capul (2006); Sudret (2008), when considering the environmental conditions described as Fourier based GP (Shinozuka and Deodatis, 1991), the outcrossing rate can be formulated with respect to this unique design point instead of the two DP estimation required in the standard PHI2 approach. Following the same logic, under some derivability assumptions introduced in Kadota (1967) when using a KL expansion of the environmental conditions, we derived the corresponding outcrossing formula:

$$P^+(t_s) = \frac{U^2}{2\pi} \frac{\|\alpha^*(t_s)\|_w}{\|\alpha^*(t_s)\|} \exp\left(-\frac{\|\alpha^*(t_s)\|^2}{2}\right)$$

where $\alpha^*(t_s)$ is the design point solution of (4.31), $\|\cdot\|$ stands for the euclidean norm, $\|\cdot\|_w$ for the weighted euclidean norm with weights

$$w_i = \left[\frac{\Psi_i'(Ut_s, y, z)}{\Psi_i(Ut_s, y, z)}\right]^2$$

for $i \in 1, ..., K$ and fixed (y, z) such that:

$$\|\alpha^*(t_s)\|_w^2 = \sum_{i=1}^{\hat{M}_{KL}} w_i \alpha_i^*(t_s)^2.$$

In order to estimate $\alpha^*(t_s)$ the trust region algorithm SQA (Sinoquet and Langoüet, 2013) was used. The latter is a derivative free algorithm and has produced excellent results on large benchmarks with a reduced simulation budget in comparison to algorithm such as iHLRF, NLPQPL, SQPAL and COBYLA (Murangira et al., 2015).

In this setting, we managed to obtain with approximately 1500 to 2000 mNARX simulations a solution to the FORM design point research problem. For fixed LT parameters $\xi = (U, \sigma_U)$ to $(15m/s, 5m/s)$ we obtained a design point norm $\|\alpha\|$ of approximately 5.3 which correspond to an instantaneous failure probability of the order 10^{-5} which has to be weighted by the selected LT probability ($\approx 10^{-11}$) since $\bar{N} = \mathbb{E}_\xi\left(P_\rho^+(t_s; \xi)\right)$. If we suppose such probability as the leading order of magnitude then the associated year failure probability, with the selected LT, would be of the order of 10^{-9} (by multiplying 10^{-16} by a year in seconds). The wind associated to this design point and the corresponding output is depicted in Figure 4.29.

As introduced, the next step would be to average multiple estimations of $P_\rho^+(t_s; \xi)$ w.r.t. the distribution of ξ. However, an additional problem linked to the high-dimensional geometry associated to ST parameters, involved in the computation of $P_\rho^+(t_s; \xi)$ for fixed ξ, could alter the confidence in the final estimate. It is the topic of the next section.

The high dimensional geometry issue. Let us consider that our model inputs (i.e. ST parameters) are all independent and Gaussian (if not an iso-probabilistic transformation can be applied before hand). It is then known (Katafygiotis and Zuev, 2008) that the probability mass of a multivariate Gaussian distribution lies on a strip centered on the ring of radius $\sqrt{d-1}$, for large d, and relatively rapidly decreases as you move away from the high probability ring. In this high-dimensional context, the design point formulation (4.31), by construction, will not find the point of failure with highest probability (since its norm will almost always be smaller than $\sqrt{d}$ for large d) and the linear approximation at that point has not the same interpretation that is expected in low dimension. Different configurations can arise. First we can notice that the failure probability will be characterized by the extend of the intersection of the failure area with the high probability ring. If the failure area is not connected, as depicted in Figure 4.30, it seems then clear that a linear approximation will not lead to any good failure probability estimation (Katafygiotis and Zuev, 2008). In the connected case, a linear approximation should be used if there is a high degree of confidence in the linearity of the limit state otherwise the estimation might be again far from reality (Katafygiotis and Zuev, 2008) as depicted in Figure 4.31. In the connected case, we can nonetheless mention the strategy proposed in Wang and Song (2018); Chiron et al. (2023) that uses the DP but then replace the linear approximation by a conic one to be calibrated and the one from Wang and Der Kiureghian (2017) which implements a strategy based on space-filling (geometrically) samples in the orthogonal plane to the design point direction. To summarize, our numerical test suggests that the mNARX model presents a configuration similar to the sketch presented in Figure 4.30, since small perturbations around the DP can lead to non-failure, and relatively small perturbations around failure points closest to the high probability ring also lead to non-failure.

Summary and perspectives To conclude, we had the hope that the FORM analysis, despite its lack of certification in the estimation (no confidence interval), would enable a rough estimation, at minimal simulation cost, of the sought failure probability. But from our literature analysis and our numerical tests, constrained in time, we finally concluded that achieving a direct FORM analysis in high dimension would not offer a good estimate of the failure probability under the conditions laid down in its original form. More tailored FORM-like approaches such as in Wang and Der Kiureghian (2017); Wang and Song (2018); Chiron et al. (2023) could be recommended when dealing with "connected-enough" failure region. More generally, the high-dimensional geometry involved is complex to grasp and therefore strongly challenges all possible strategies that often will require large number of simulations in the rare event setting. Dimension reduction appears to us to be a recommended or even a mandatory step before or within the reliability task (keeping in mind that learning the effective dimension can also be complex and requires a large number of simulations). Finally, to gain a broader perspective on the applicable methods and their performance in high dimension, a literature review, or at least a picture of it at current time, is proposed in the report Breaz et al. (2024).

4.2.6 Conclusions of the 2D benchmark

Several ULS methods were compared on a simplified 2D benchmark (mean wind speed and turbulence) for the case of stationary events: contour methods, a combination of GP and sequential sampling, a BNN and finally an outcrossing optimization approach in ST-LT

space. The BNN faces limitation in prediction accuracy due to non-Gaussian distribution of the ULS tail distribution. The outcrossing approach is also limited as it introduces high dimension for the ST input parameters which implies non connected local minima for which the FORM approach is not appropriate. Fortunately, the GP with sequential sampling method was successful in predicting with enough accuracy the annual failure probability of ULS, with a feasible computational time (measured by the number of calls to costly multiphysics simulators). A minimum number of stochastic seeds should be considered in order to capture the ST variability. If for Teesside, the Q90 quantile values of the extreme loading compares well between the Sequential sampling and the Contour methods, significant differences have been obtained for the South Brittany case study. These differences are due to high contribution of ST uncertainty inside the domain, in contradiction with the main assumption of the contour approach. Note that simulations are also run with the mNARX simulator trained the on fixed NREL 5MW wind turbine. This difference of failure point distributions between South Brittany and Teesside case studies can thus only be due to a specificity of the joint wind parameter distribution or the longer simulation (1h instead of 10min). Similarly, a more difficult convergence of annual failure probability and slight underestimation when compared to brute force may be explained by a use of mNARX out of its training domain. Given its efficiency for converging in return value load, plus assumption that limitation on annual failure convergence and bias will not appear when using a physical simulator instead of a surrogate like mNARX, we selected this approach for the final application on Teesside 6 and South Brittany case studies 7.

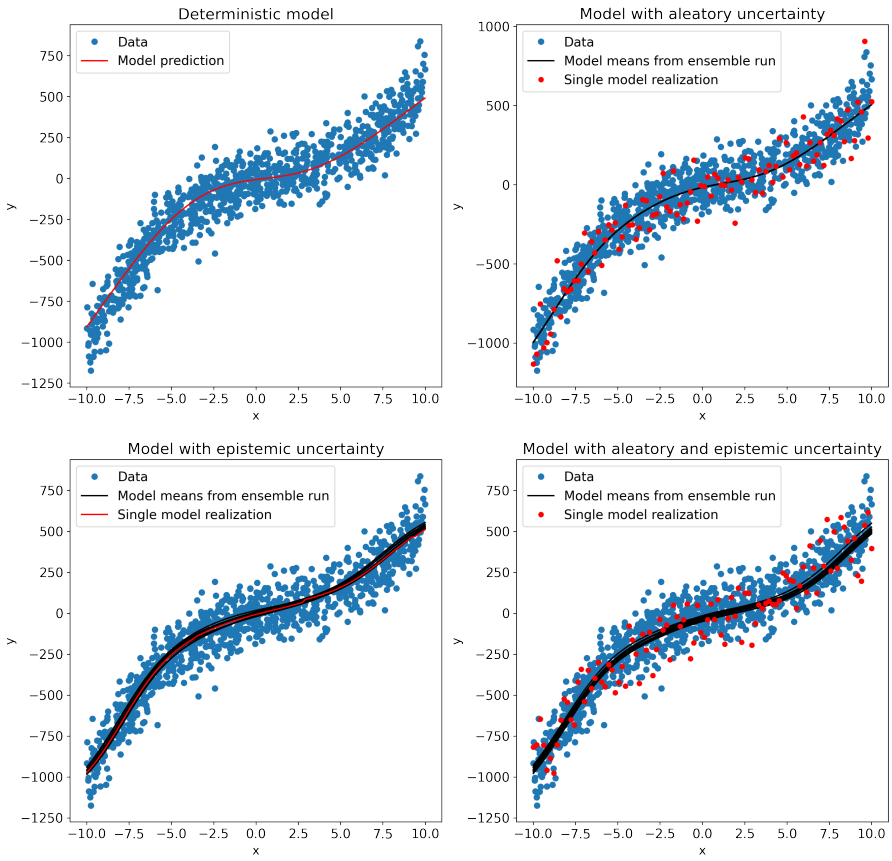

Figure 4.1: Examples of a Bayesian Neural Network (BNN) fit to a simple cubic polynomial curve, illustrating how different uncertainties can be represented by the BNN. Top left: deterministic model not considering any uncertainty, top right: model considering all uncertainty as aleatory, bottom left: model taking only epistemic (model) uncertainty into account, bottom right: a model that considers both epistemic and aleatory uncertainties. Figure reproduced from Hiperwind Deliverable 4.1 Dimitrov et al. (2022).

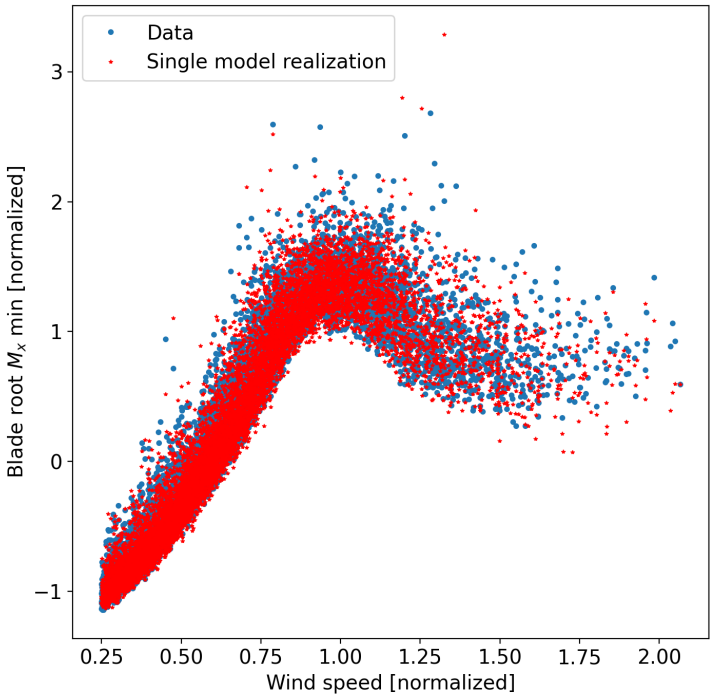

Figure 4.2: Illustration of the scatter from a single realization of a BNN model versus the actual data.

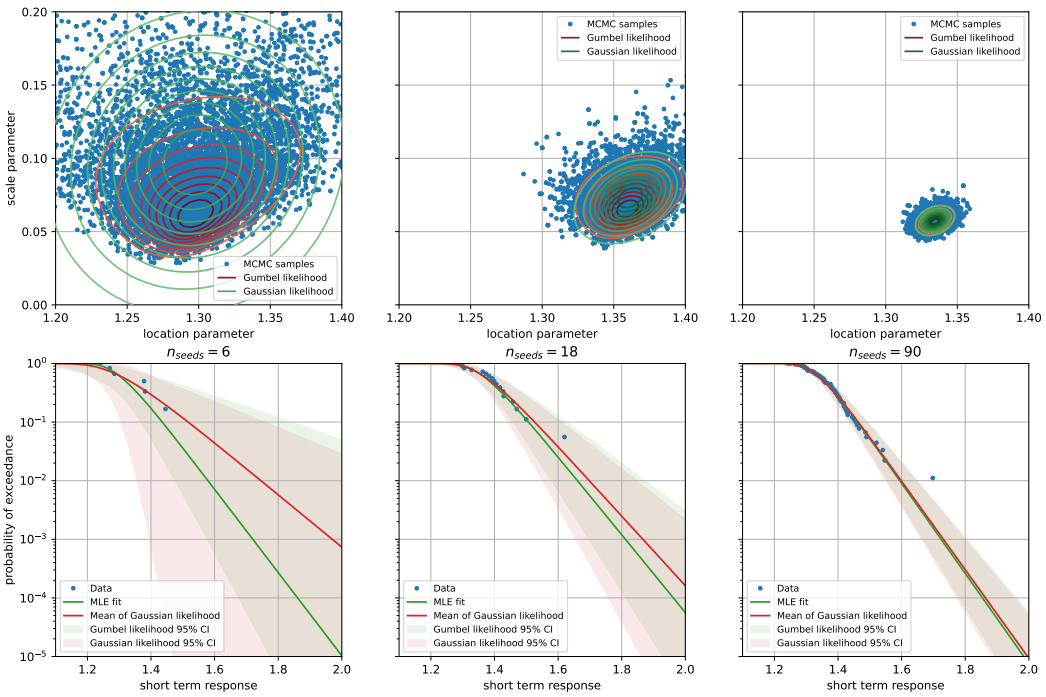

Figure 4.3: Examples of Gaussian likelihood fitting to account for uncertainty in parameter estimates. Upper row: The "true" likelihood of the Gumbel-parameters under the observed data, the corresponding MCMC-samples, and the resulting best-fit Gaussian likelihoods. Second row: The corresponding Gumbel-distributions with 95% confidence intervals based on the "true" and fitted likelihoods.

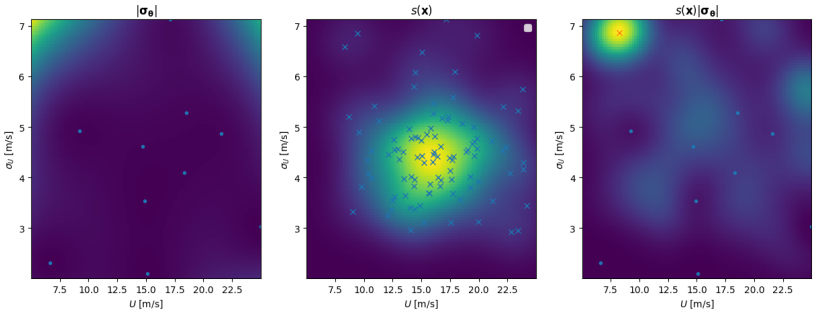

Figure 4.4: Left: the standard deviation of distribution parameters as function of LT parameters $\boldsymbol{x} = (U, \sigma_U)$. Middle: the estimated distribution $s(\boldsymbol{x})$ of responses above 100-year return value). Right: the acquisition function $s(\boldsymbol{x}) \left|\sigma_{\boldsymbol{\theta}(\boldsymbol{x})}\right|$. Blue dots show existing points used to train the GP-model. Blue crosses show points leading to a response above the 100-year return value, and the red cross shows the new point $\boldsymbol{x}_{new}$.

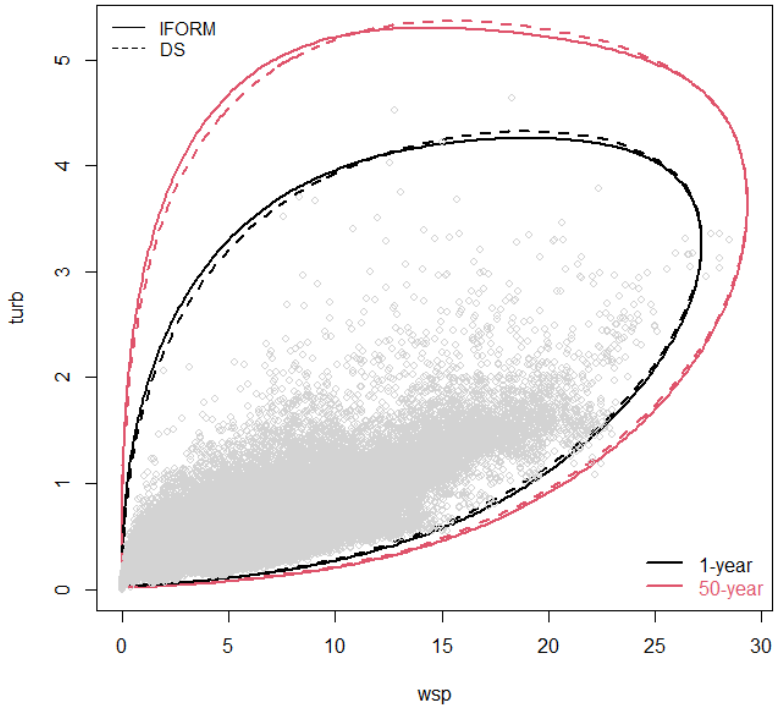

Figure 4.5: IFORM and DS contours for wsp (U) and turbulence (σ_U) with the omni-directional data, Teesside location.

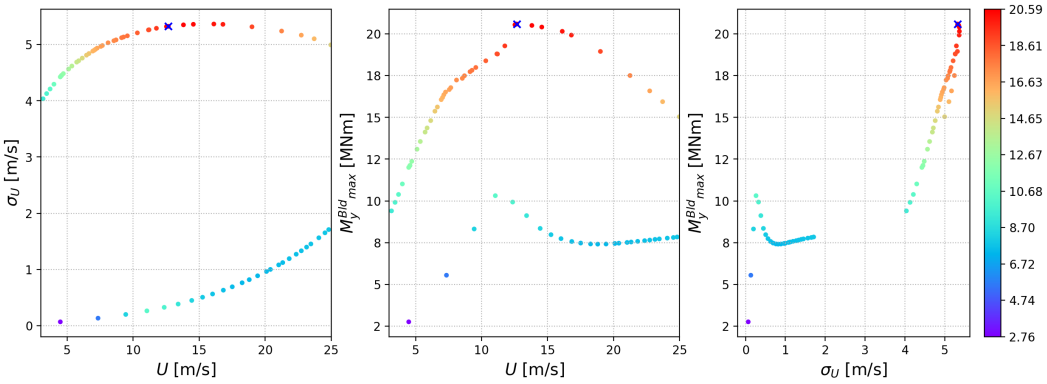

Figure 4.6: DS 50-year contour and corresponding extreme response 50% fractile of flapwise blade root bending moment $M_y^{Bld}[MNm]$, Teesside location.

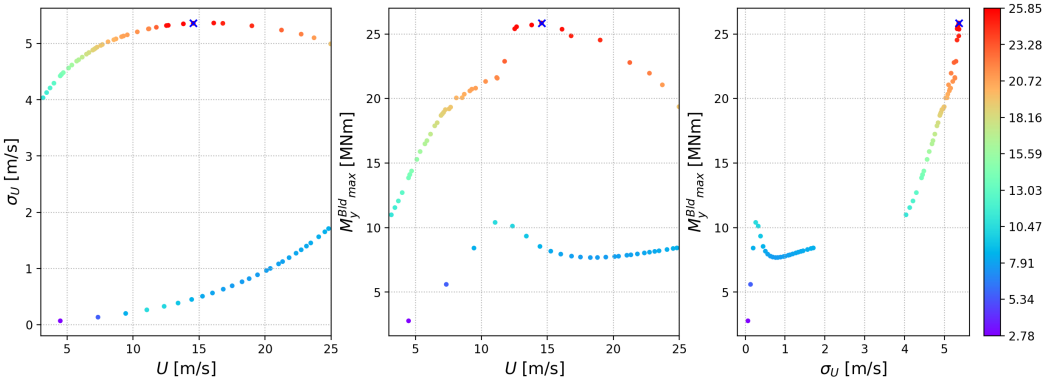

Figure 4.7: DS 50-year contour and corresponding extreme response 90% fractile of flapwise blade root bending moment $M_y^{Bld}[MNm]$, Teesside location.

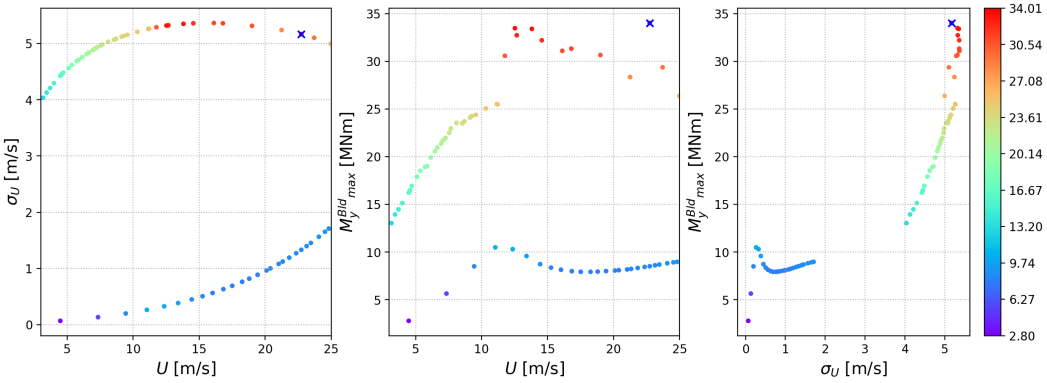

Figure 4.8: DS 50-year contour and corresponding extreme response 99% fractile of flapwise blade root bending moment $M_y^{Bld}[MNm]$, Teesside location.

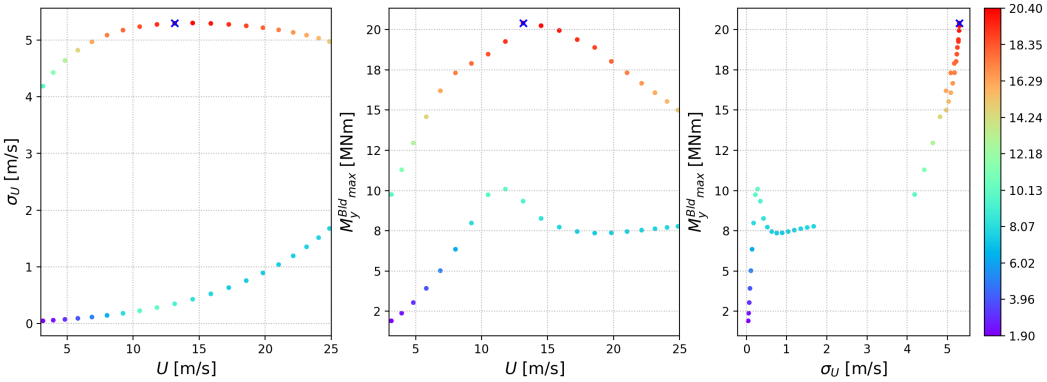

Figure 4.9: IFORM 50-year contour and corresponding extreme response 50% fractile of flapwise blade root bending moment $M_y^{Bld}[MNm]$, Teesside location.

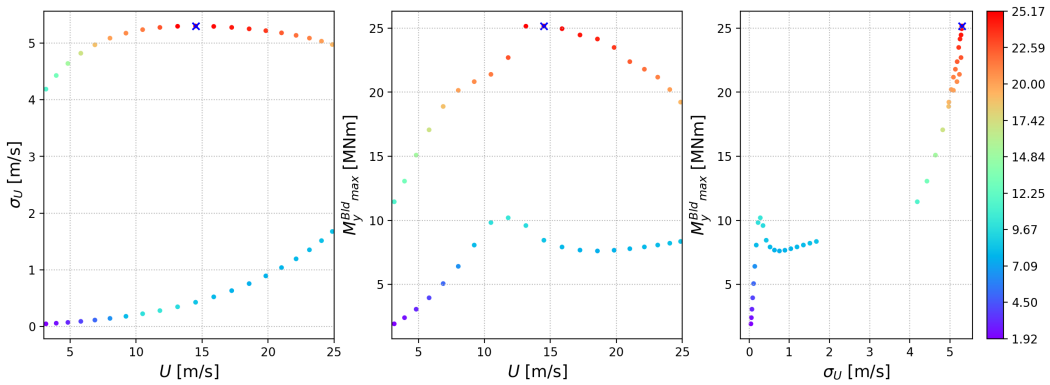

Figure 4.10: IFORM 50-year contour and corresponding extreme response 90% fractile of flapwise blade root bending moment $M_y^{Bld}[MNm]$, Teesside location.

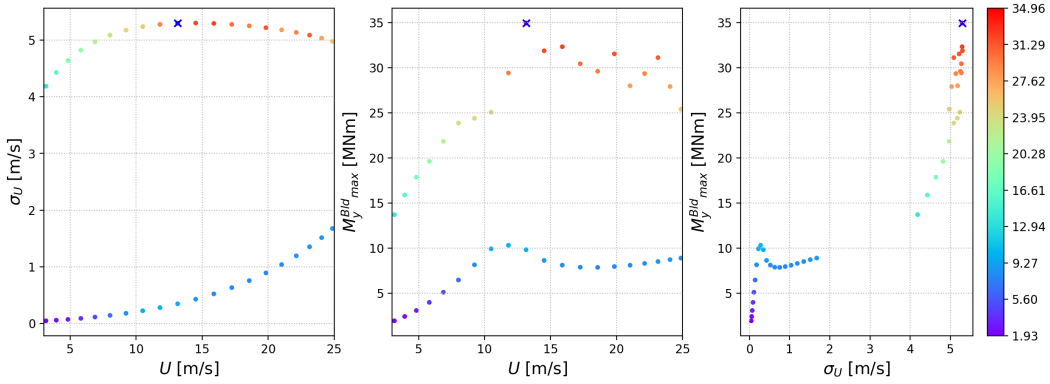

Figure 4.11: IFORM 50-year contour and corresponding extreme response 99% fractile of flapwise blade root bending moment $M_y^{Bld}[MNm]$, Teesside location.

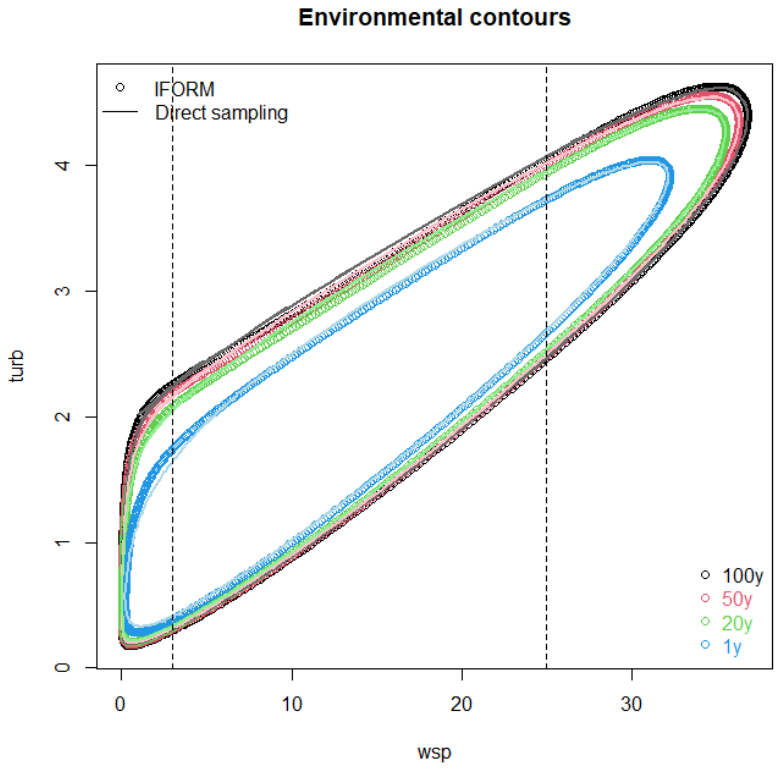

Figure 4.12: IFORM and DS contours for wsp (U) and turbulence (σ_U), South Brittany location.

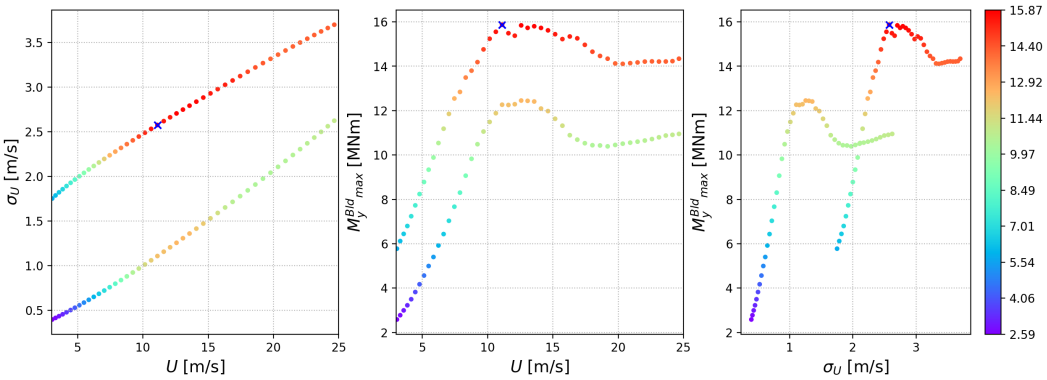

Figure 4.13: IFORM 1-year contour and corresponding extreme response 90% fractile of flapwise blade root bending moment M_{Bld}^{y} [MNm].

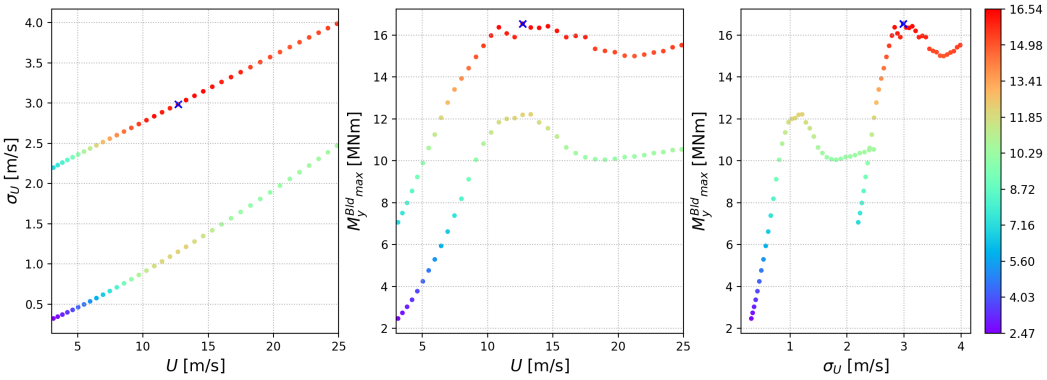

Figure 4.14: IFORM 50-year contour and corresponding extreme response 90% fractile of flapwise blade root bending moment M_{Bld}^{y} [MNm].

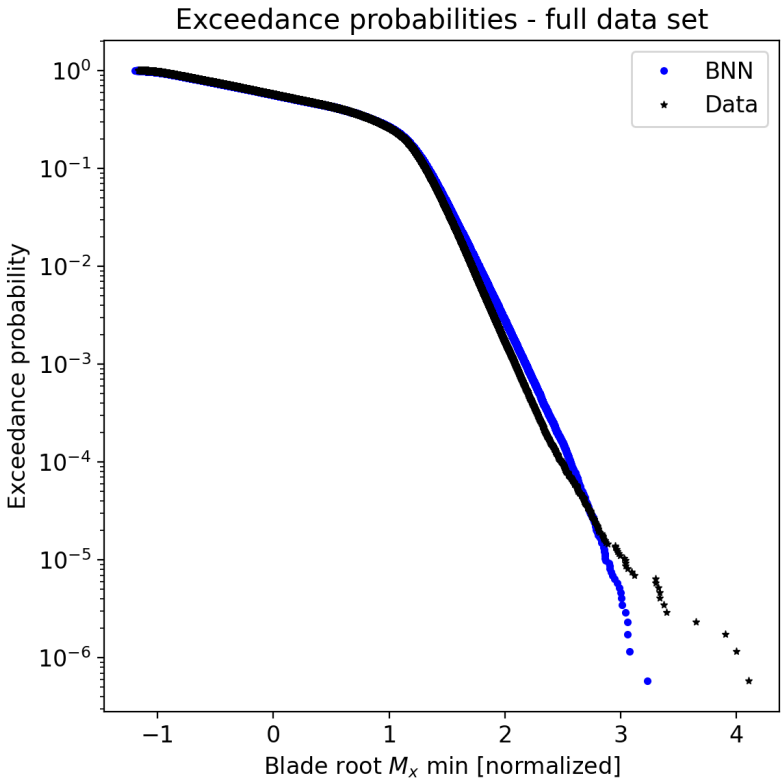

Figure 4.15: Comparison of tail probabilities between simulated data generated with the mNARX blade load time series simulator Dimitrov et al. (2022); Schär et al. (2023) and a BNN fit to the data.

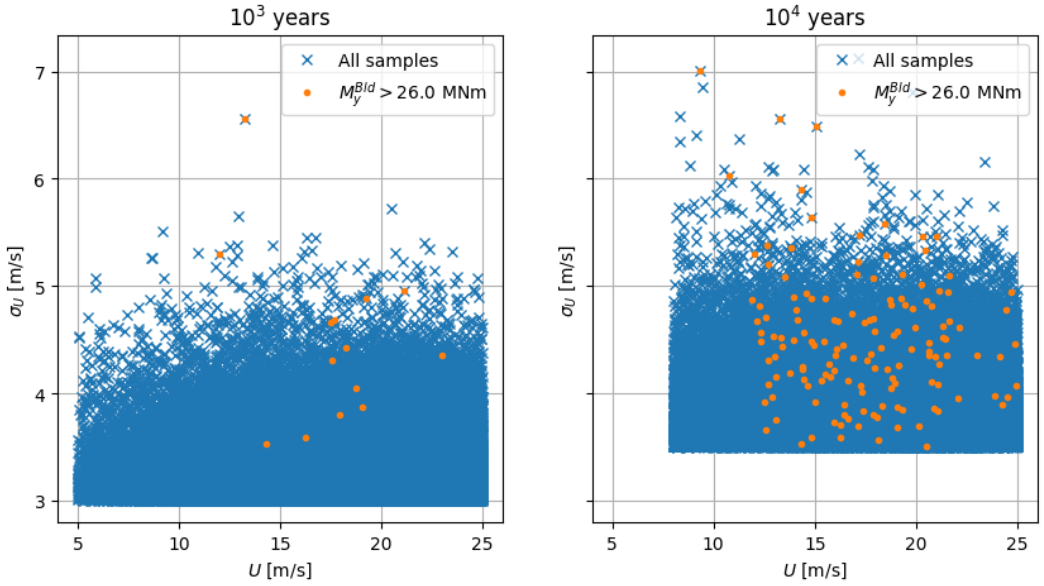

Figure 4.16: Brute force samples for the 10^3-year and 10^4-year periods.

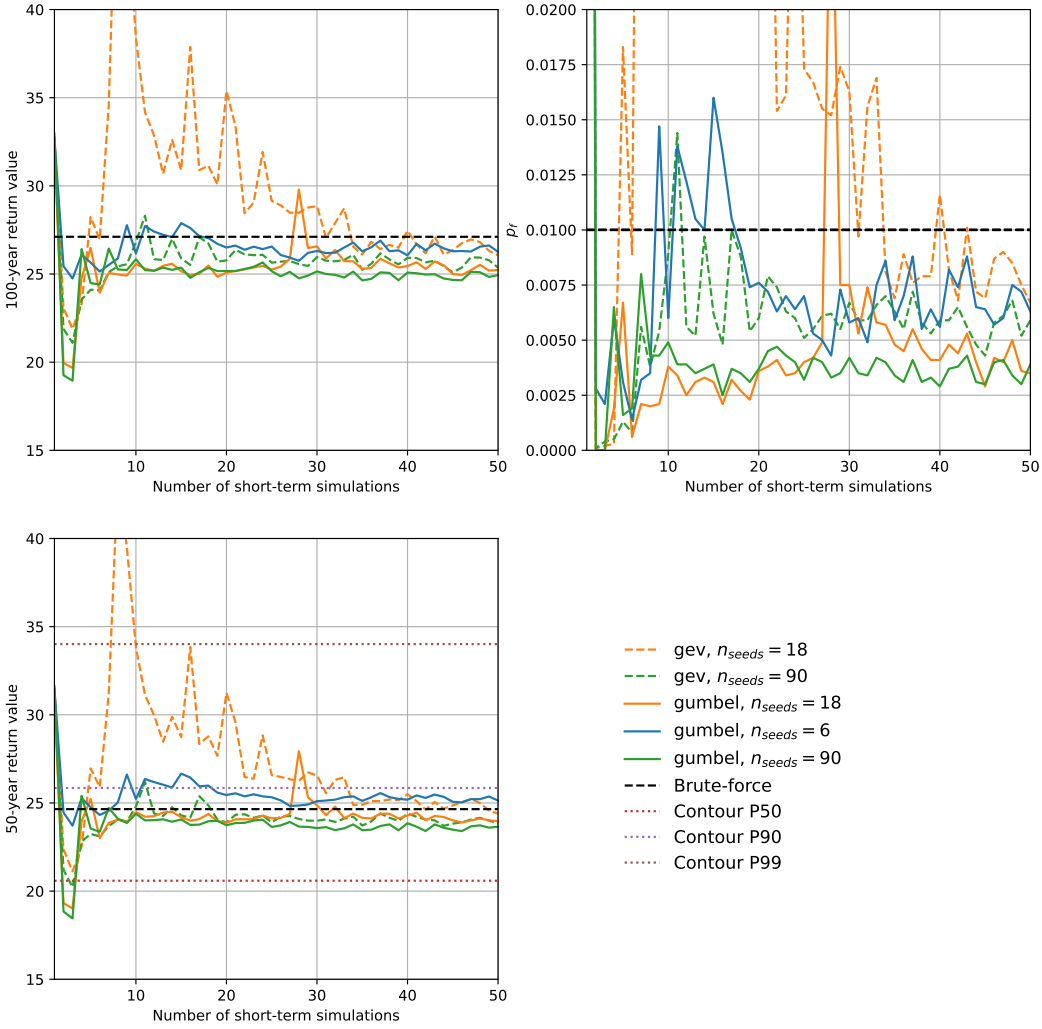

Figure 4.17: Estimated 100- and 50-year return values for Teesside as well as estimated failure probability p_f from sequential sampling, as function of the number of ST simulation used to train the GP. Results from brute-force sampling and from the direct sampling contour method (for 50-year return value) are also included.

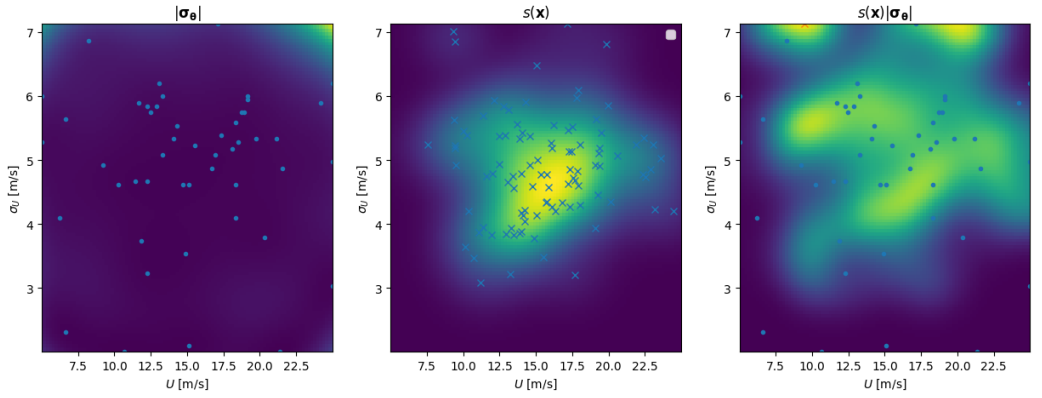

Figure 4.18: Distribution of Sequential Sampling points in the (U, σ_U) space after 50 iterations.

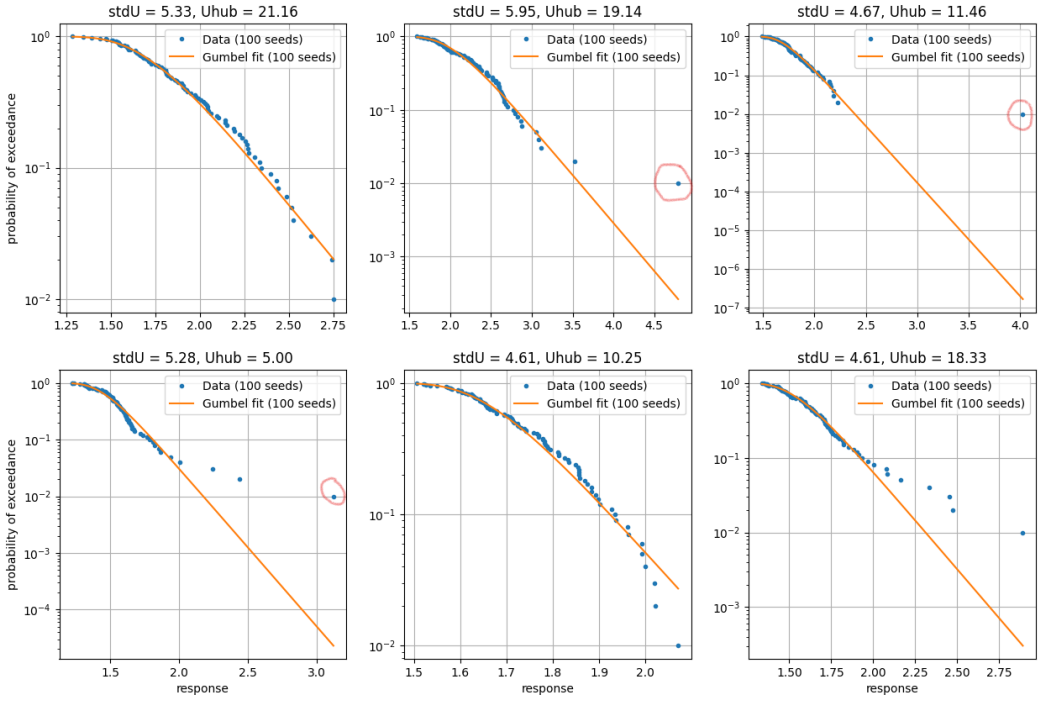

Figure 4.19: Examples of Gumbel fit on exceedance curves for several LT conditions. Outlier point significantly deviating from the tail are highlighted by surrounding circcles.

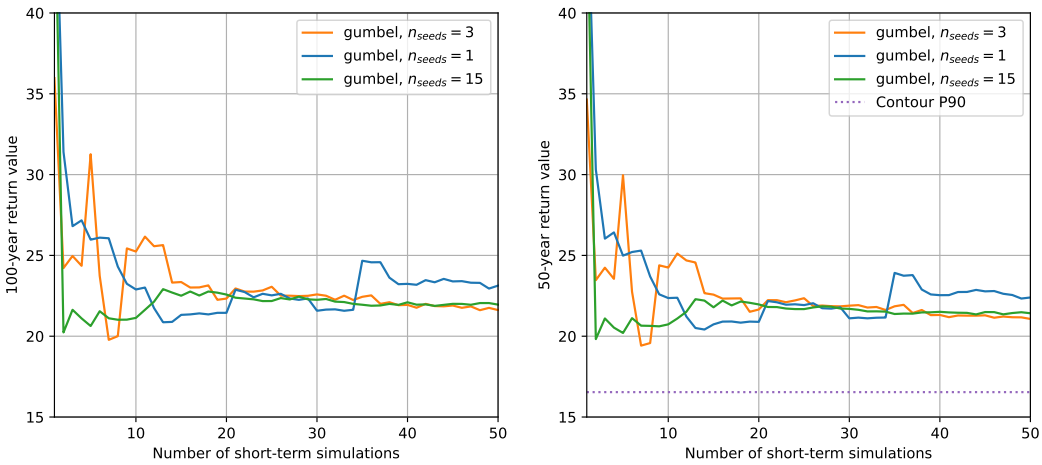

Figure 4.20: Estimated 100- and 50-year return values for South Brittany from sequential sampling, as function of the number of ST simulation used to train the GP. For the 50-year return period the result from the IFORM contour method is shown.

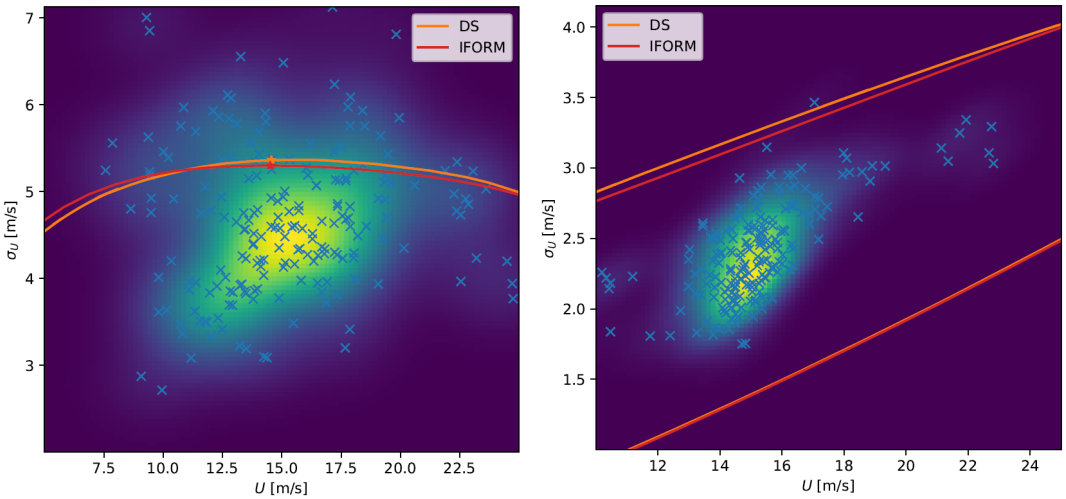

Figure 4.21: Contribution to the 50-year return value as function of LT parameters for Teesside (left) and South Brittany (right).

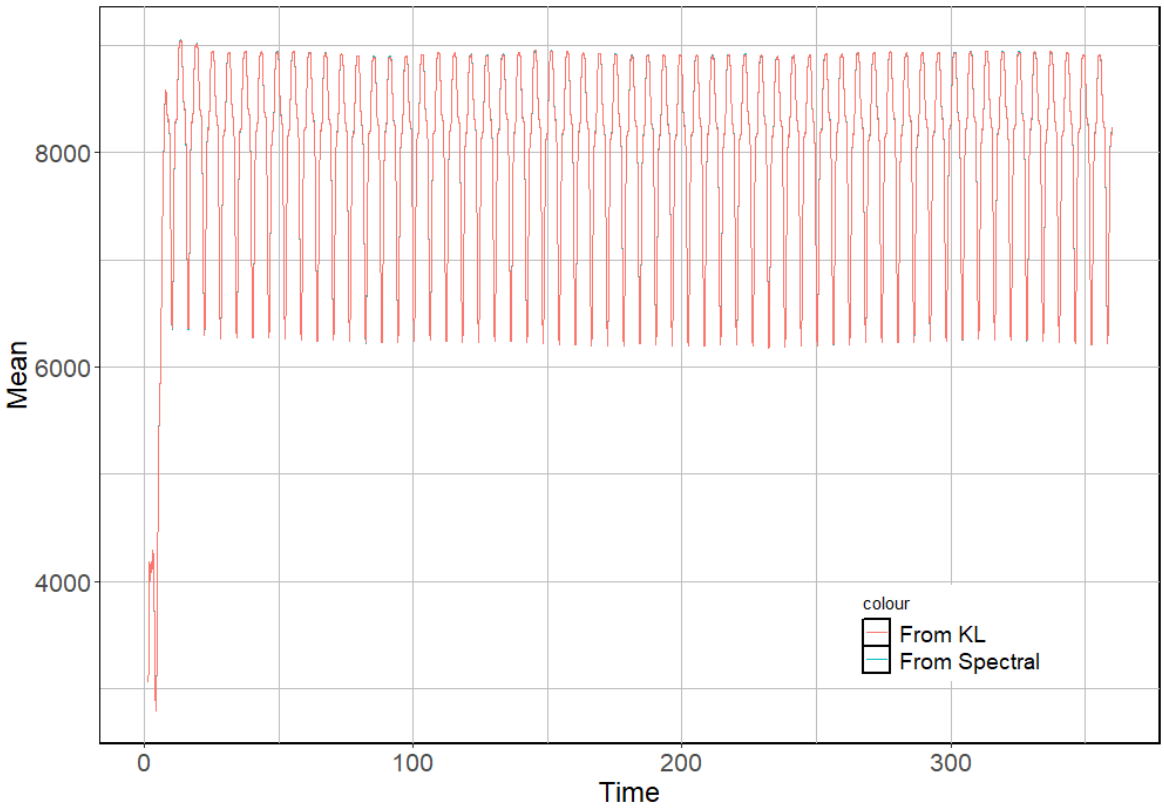

Figure 4.22: Mean with respect to time of the flapwise blade root moment (KNm) obtained from mNARX.

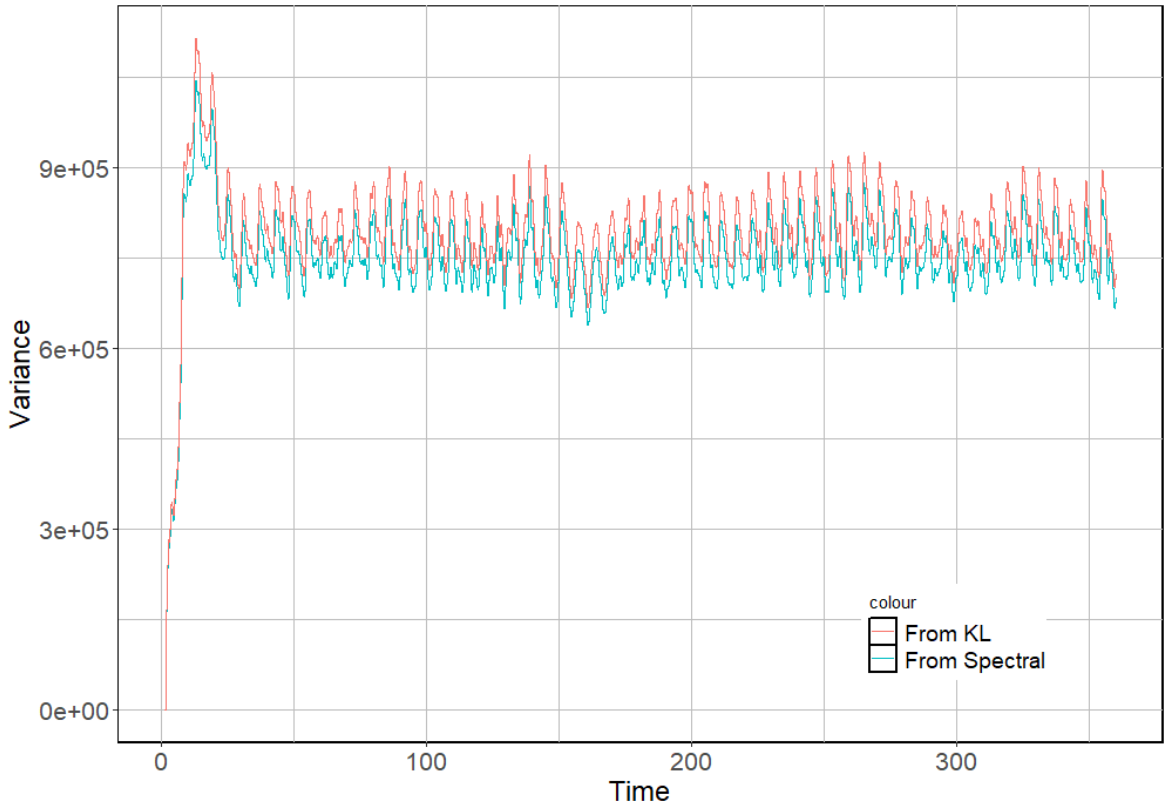

Figure 4.23: Variance with respect to time of the flapwise blade root moment (KNm) obtained from mNARX.

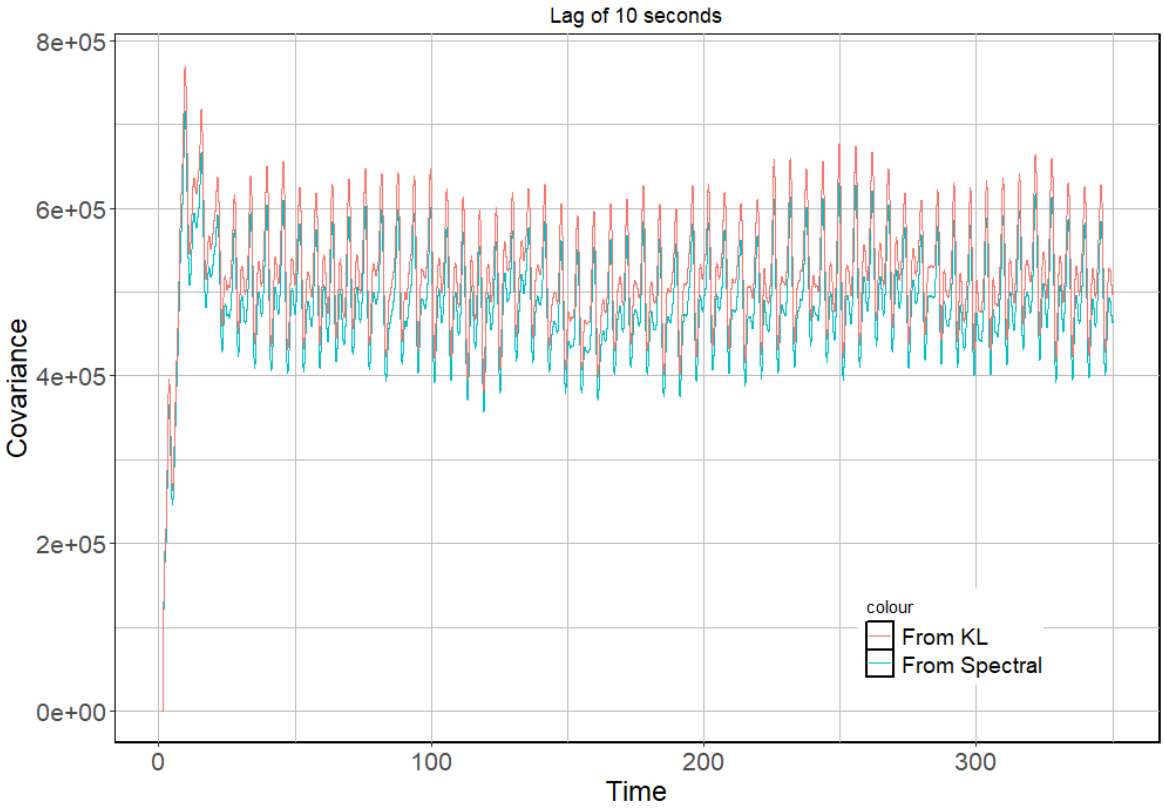

Figure 4.24: Covariance with lag time of 10 seconds of the flapwise blade root moment (KNm) obtained from mNARX.

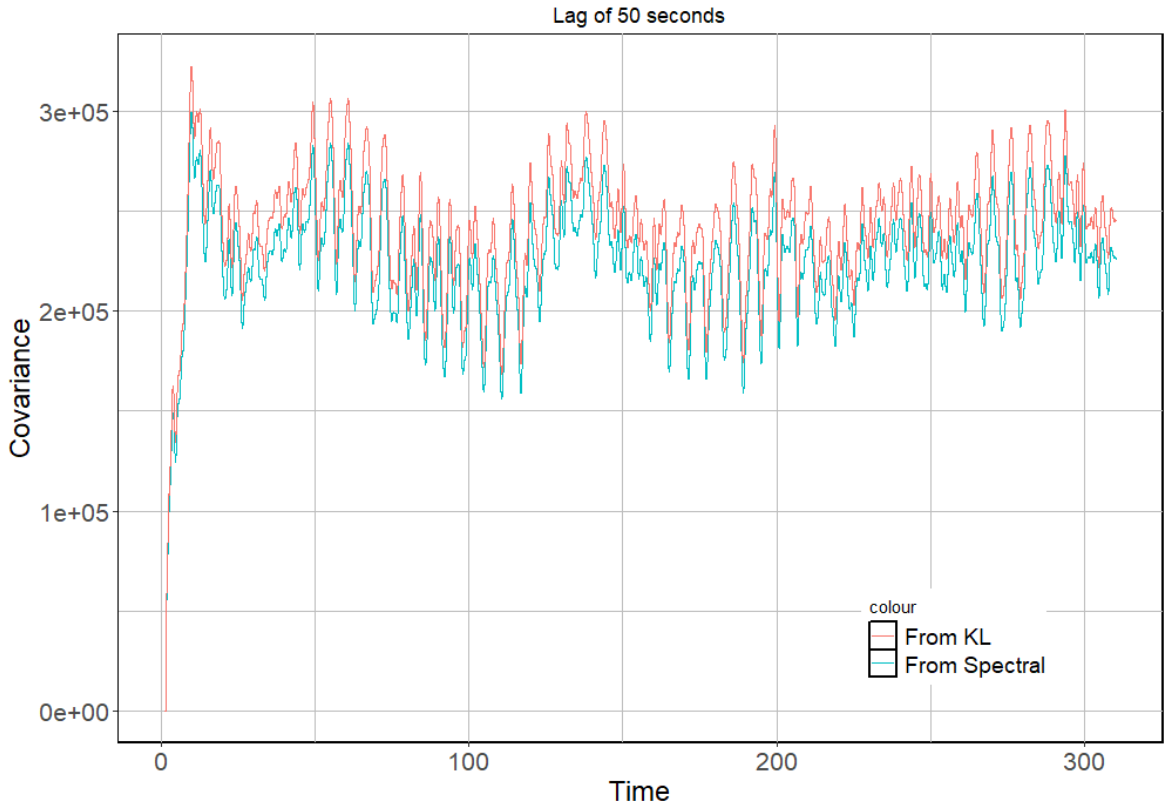

Figure 4.25: Covariance with lag time of 50 seconds of the flapwise blade root moment (KNm) obtained from mNARX.

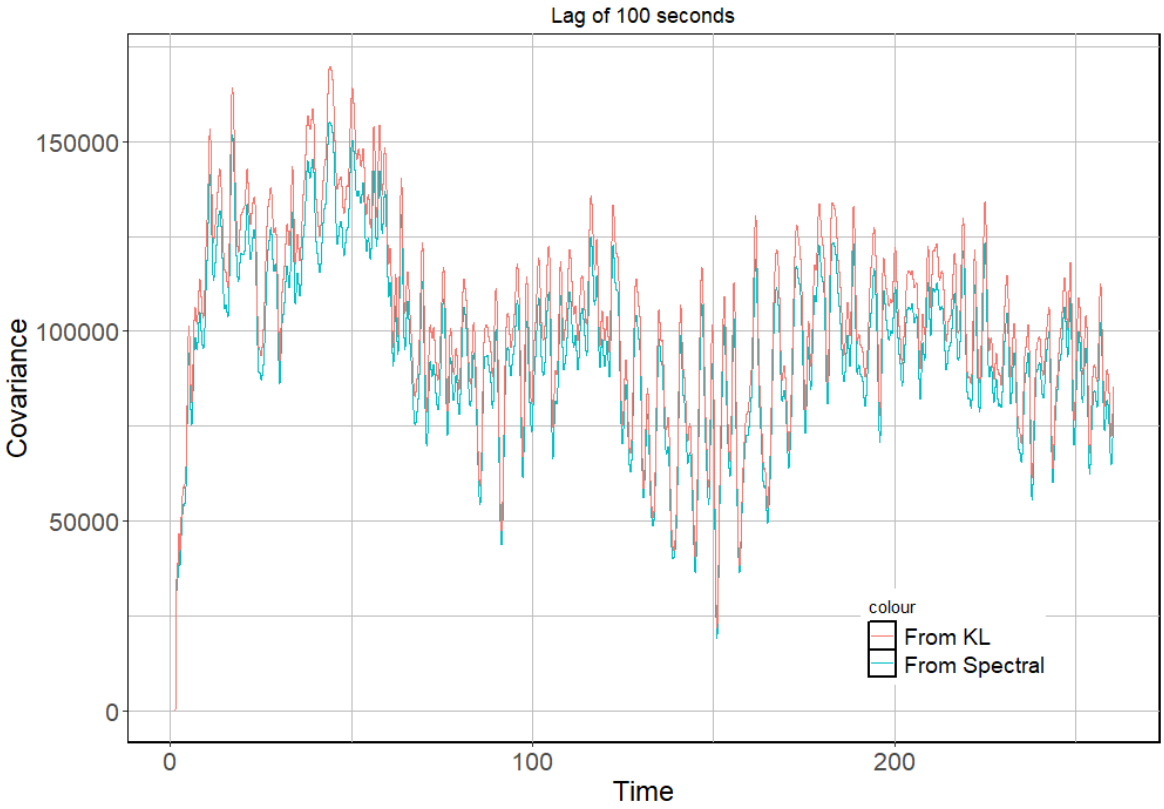

Figure 4.26: Covariance with lag time of 100 seconds of the flapwise blade root moment (KNm) obtained from mNARX.

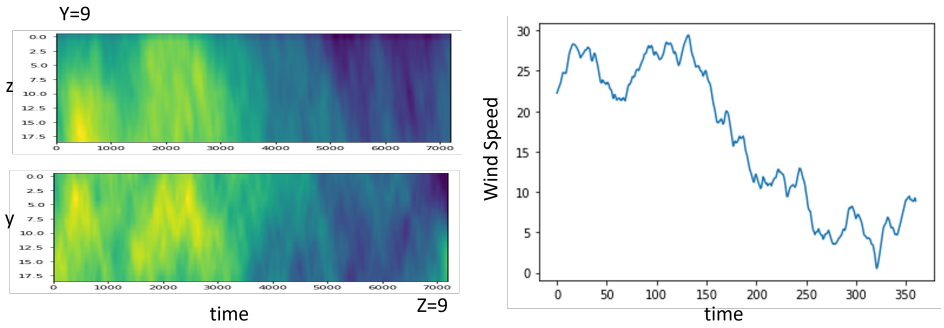

Figure 4.27: Wind speed in m/s associated to the design point estimated in the ST-LT space.

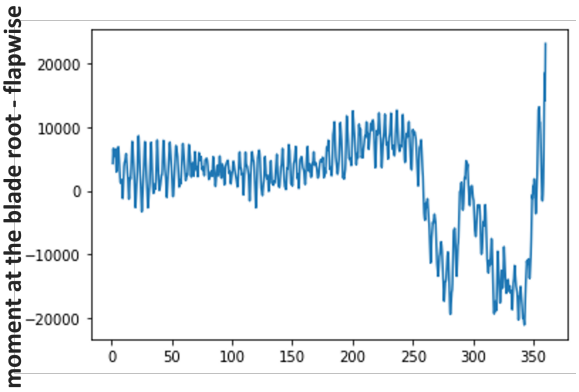

Figure 4.28: Flapwise blade root moment in kNm associated to the estimated DP in the ST-LT space.

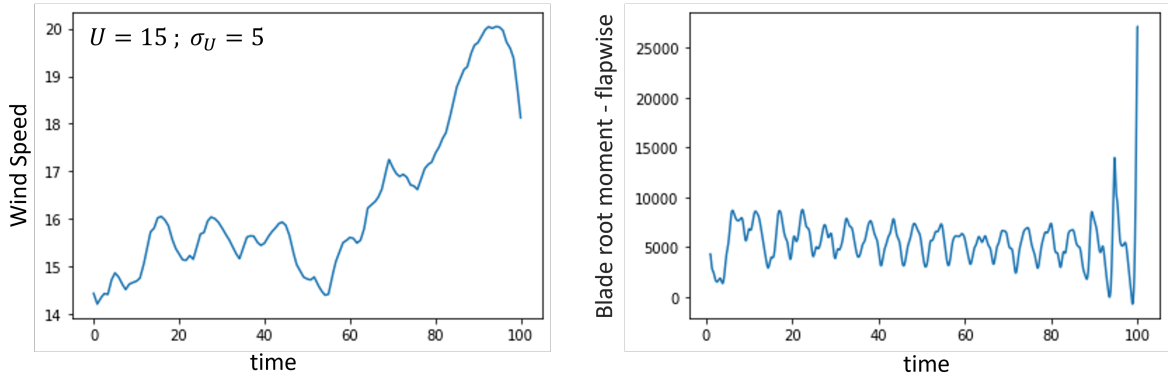

Figure 4.29: Wind speed (m/s) associated to the design point estimated in the ST space and corresponding mNARX output (kNm).

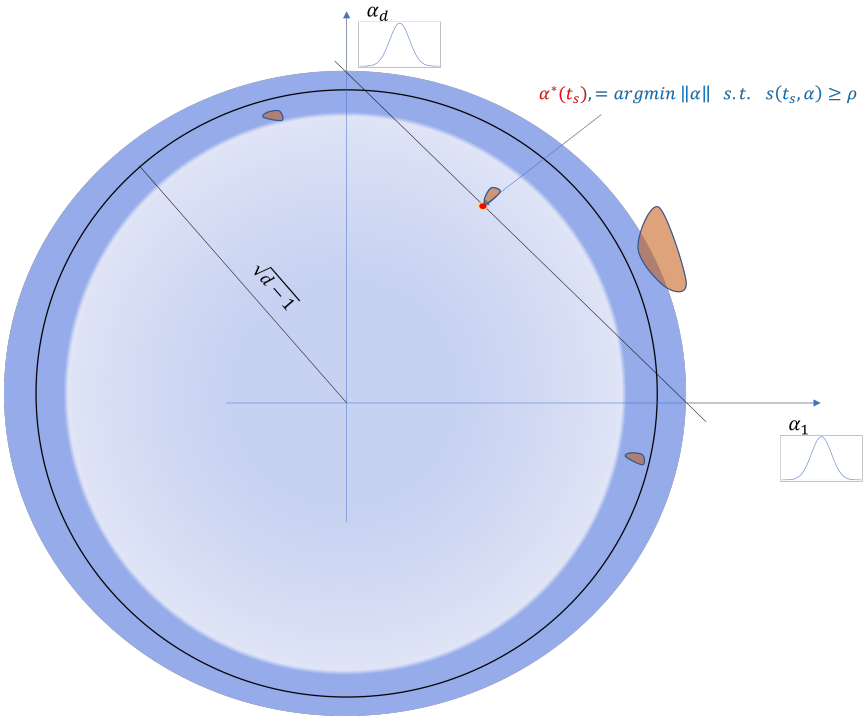

Figure 4.30: Sketch of a standard Gaussian space, design point and disconnected failure area configuration in high dimension.

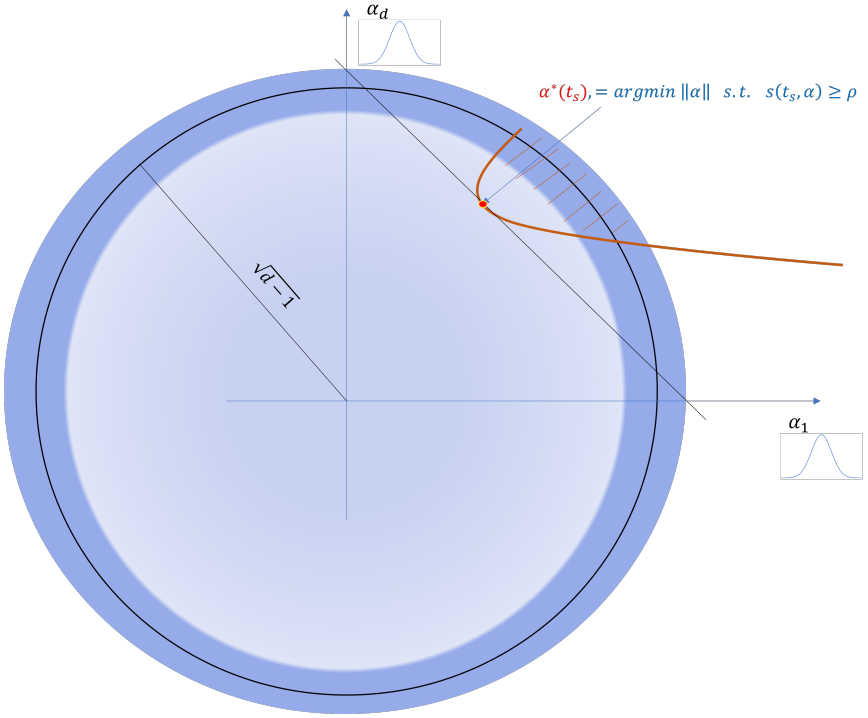

Figure 4.31: Sketch of a standard Gaussian space, design point and connected failure area configuration in high dimension.

5 Methodologies for transient ULS

In this section we focus on the case of a transient event that is composed of a wind gust and or a shutdown due to electric grid loss, as considered for instance in the DLC2.3 of IEC (2019b). A new gust description, fitted from real observations, is compared to the IEC gust, then a methodology is presented to compute the failure probability and analyse the gust and shutdown influence on ULS reliability.

The case study selected for this analysis is an OWT with monopile foundation of the Teesside wind farm case study (EDF, UK) that is described in the stationary input setting in section 6.1 but with transient wind. The structure is similarly parameterized. The quantity of interest, the LT wind parameters and threshold ρ are also similar. The main difference is the consideration of a transient ST wind by adding to a fixed ST wind a gust plus the grid loss.

5.1 Modelling of Transient Events

5.1.1 Turbulence

The turbulent flow field was generated by HiperSim Dimitrov (2023). Originally in the project, the turbulence intensity was set by scaling the flow field according to the standard deviation of the stream-wise velocity. However, it was later discovered that this distorted the acceleration statistics. According to Mann (1994); Kelly (2018), the HiperSim parameters can be related to turbulence intensity through the $\alpha\epsilon^{2/3}$ parameter. The equation used in this work is shown by equation (5.1).

$$\alpha\epsilon^{2/3} = \frac{\left(\frac{\sigma_u}{1.802}\right)^2}{0.69L^{2/3}}. \tag{5.1}$$

Since the turbulence box is generated with finite dimensions and spacing, the underlying frequency spectrum of turbulence is truncated. So the underlying turbulence intensity will appear less than the expected level.

5.1.2 Gusts

Gusts are modeled with equation (5.2) where $u(\boldsymbol{x}, t)$ is the normal turbulent flow and the second term is the gust. The gust is parameterized by the random variables A representing the acceleration, and T denoting the rise time T. The variable t_{gust} determines the time of the gust occurrence. It is assumed that the gust is uniform in the transverse directions.

$$U(\boldsymbol{x}, t) = u(\boldsymbol{x}, t) + \frac{AT}{\pi}\left(1 + \tanh\left(\frac{\pi\left(t - t_{gust}\right)}{T}\right)\right). \tag{5.2}$$

The random variable A follows a log-normal distribution whose parameters are given later on. T is also modelled with a log-normal distribution with a standard deviation $\sigma_T = 0.2$, and the mean is conditioned on A, as shown in equation (5.3), where $\Delta U_{ref} = 6m/s$ and $a_{ref} = 0.4m/s^2$.

$$\mu_T = \sigma_T^2 + \log\left(\frac{\Delta U_{ref}}{a_{ref}\left(1+\left(\frac{A}{a_{ref}}\right)^3\right)^{\frac{1}{3}}}\right). \tag{5.3}$$

Two different distributions were considered for the log-normal distribution of A. The first is based on statistics with a 0.1Hz filter frequency, and the second a $1/3Hz$ frequency. The mean and standard deviation for both of these distributions are given in Table 5.1. Most of the work here is based on the statistics with a $1/3Hz$, however preliminary exploratory work considered $0.1Hz$ statistics as well. These statistics have been determined by M. Kelly during WP2 of HIPERWIND and explained further in Kelly and Vanem (2022).

Table 5.1: Gust acceleration distribution parameters

Filter Frequency $[Hz]$	μ_a	σ_a
$\frac{1}{3}$	-0.08	0.26
0.1	-0.75	0.22

5.1.3 Grid-loss

The time of the grid loss is considered to occur randomly, with a uniform distribution without correlation with any other random variables. When grid loss and gusts are simulated together, the relative timing of these two events becomes a stochastic variable. A total of 700s is simulated, where the gust occurs at 300s and the shutdown can occur at any time in the first 600s. The additional 100s is to capture any transient loads occuring after a late shutdown event.

5.2 The effect of gust shape on loads with comparisons to IEC 61400 design standards

The gust function defined in section 5.1.2 differs from the gust function typically used in the IEC 61400-1 design standard IEC (2019a). A study was carried out to understand the impact of the gust function on the loads.

The IEC gust is described in section 5.2.1. Different modifications of the gust function were created to explore the impact of different aspects, these are described in section 5.2.2. Finally, a MC study was carried out to understand the impact of gust shape on the loads.

5.2.1 The Extreme Operating Gust within the 61400-1 design standards

The Extreme Operating Gust (EOG) defined within the IEC 61400-1 design standard IEC (2019a) is given by equation (5.4) where U_{gust} defines the magnitude and T_{eog} is taken to be $10.5s$. This equation is only valid between the time $t = 0$ and $t = T_{eog}$.

$$U(z,t) = U_{avg}(z) - 0.37U_{gust}\sin\left(\frac{3\pi t}{T_{eog}}\right)\left(1-\cos\left(\frac{2\pi t}{T_{eog}}\right)\right) \tag{5.4}$$

within the standard, U_{gust} is defined as shown in equation (5.5) which gives two possible values. For this application, only the second value is relevant, which depends on the standard deviation of the stream-wise velocity (σ_u), the rotor diameter $D = 93m$ and turbulence scale parameter $\Lambda_1 = 42m$ in this case.

$$U_{gust} = \min\left(1.35\left(V_{e1} - V_{hub}\right); 3.3\left(\frac{\sigma_u}{1 + 0.1\left(\frac{D}{\Lambda_1}\right)}\right)\right). \tag{5.5}$$

5.2.2 Matching acceleration and rise-time with the EOG

Multiple ways of defining the EOG were considered in this study, the first is to use the definitions within the 61400 design standards summarized in section 5.2.1. This definition depends only on the stochastic variable σ_u. Both the U_{gust} and T_{eog} parameters can be varied to match the statistics described in section 5.1.2. This section describes the relationship between U_{gust} and T_{eog} and the A and T values.

The peak acceleration of the EOG is given in equation (5.6),

$$a_{eog} = \frac{6.13 U_{gust}}{T_{eog}}. \tag{5.6}$$

To capture the influence of T from the $\tanh$ gust function, in the EOG gust function, we consider matching the changes in velocity between the two functions. In the first cases, we consider only matching the maximum change in velocity. This leads to the definition of U_{gust} in equation (5.7) in terms of the A and T from the $\tanh$ gust function,

$$U_{gust} = \frac{2AT}{0.74\pi}. \tag{5.7}$$

An alternative change in velocity considers the difference between the minimum velocity and the maximum velocity, this leads to the definition in equation (5.8),

$$U_{gust} = \frac{2AT}{\pi}. \tag{5.8}$$

Figure 5.1 compares the $\tanh$ gust with different versions of the EOG gust. In all cases, the A and T parameters were taken as 0.8 and 6 respectively. The different curves are shifted to highlight how they match in acceleration and the different ΔU values. "EOG acc" only matches the acceleration and retains the $T_{eog} = 10.5$ from the design standards. "EOG max" uses both A and T to match both the acceleration and the maximum velocity. "EOG delta" uses both A and T to match difference between the maximum and minimum velocity. Finally, "TANH" is the $\tanh$ gust function using A and T.

5.2.3 The loads due to gust shape

A MC simulation was carried out to explore the effect of the gust function. A sample of size 100,000 was taken. The considered stochastic space includes the same 5 dimensions than the stationary ULS (wind speed, standard deviation of streamwise velocity, wave height, wave period and wind/wave misalignment). When relevant, the acceleration and gust rise

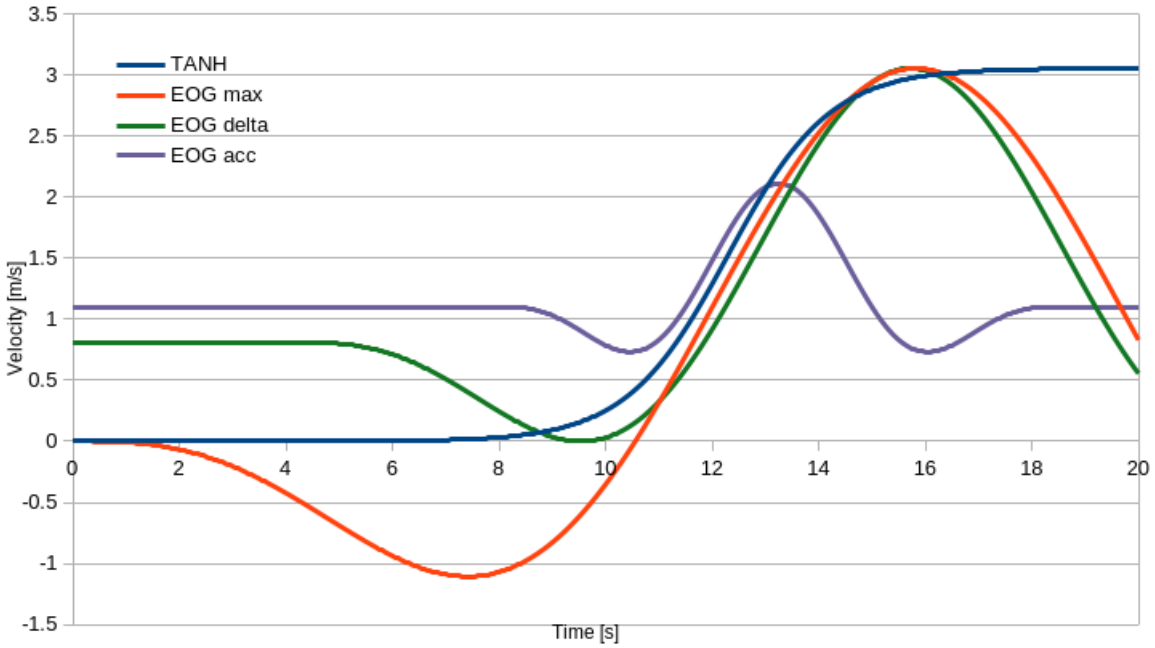

Figure 5.1: Comparison of different EOG functions with the tanh gust.

times were also included to control the strength of the gust. The von Mises stress of the tower base and monopile base were compared.

Figure 5.2 and 5.3 shows the difference between the IEC EOG gust using the standard definition and the tanh gust, for the tower stress and monopile stress respectively. The standard EOG is based on the standard deviation of streamwise velocity, while the TANH gust function and the other gusts are based on the joint (A, T) stochastic space. Since only the standard EOG shows high loads at high wind speed, these loads can be attributed to the gust strength being conditioned on the standard deviation of streamwise velocity. For these simulations, the standard EOG simulations included an EOG with every simulation, it is not clear what is the intended return period of this events, where as the A and T statistics are based on the largest event in any given 10 minute period. However, what these graphs show is how these two different gust and stochastic space definitions effect the overall trends.

The graphs also show how different EOG gusts, defined with the A and T variables compare with the TANH function. The TANH function shows higher loads below rated and lower loads above rated. This is likely due to the fact that the wind speed remains high after the gust, so the simulation is effectively operating at a higher wind speed and thrust operating on different points of the thrust curve.

Comparisons among the different EOG gusts based on A and T shows the effect of varying the T_{eog}. Keeping T_{eog} at $10.5s$ produces the lowest loads, followed by the gust based on matching the difference and finally, the gust based on matching the maximum velocity gave the highest loads. The EOG based on matching difference of velocity gave loads similar to the TANH function.

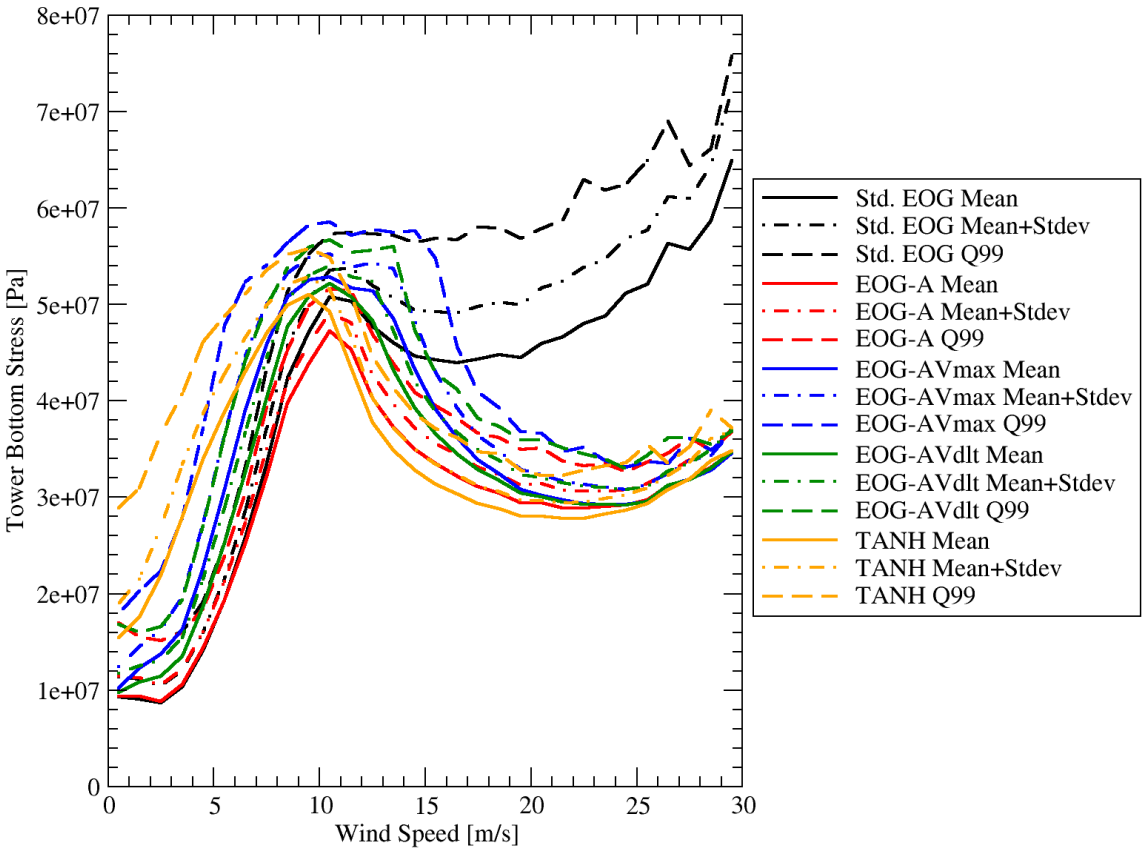

Figure 5.2: Comparison of the tower stress from the standard EOG function and the tanh gust function.

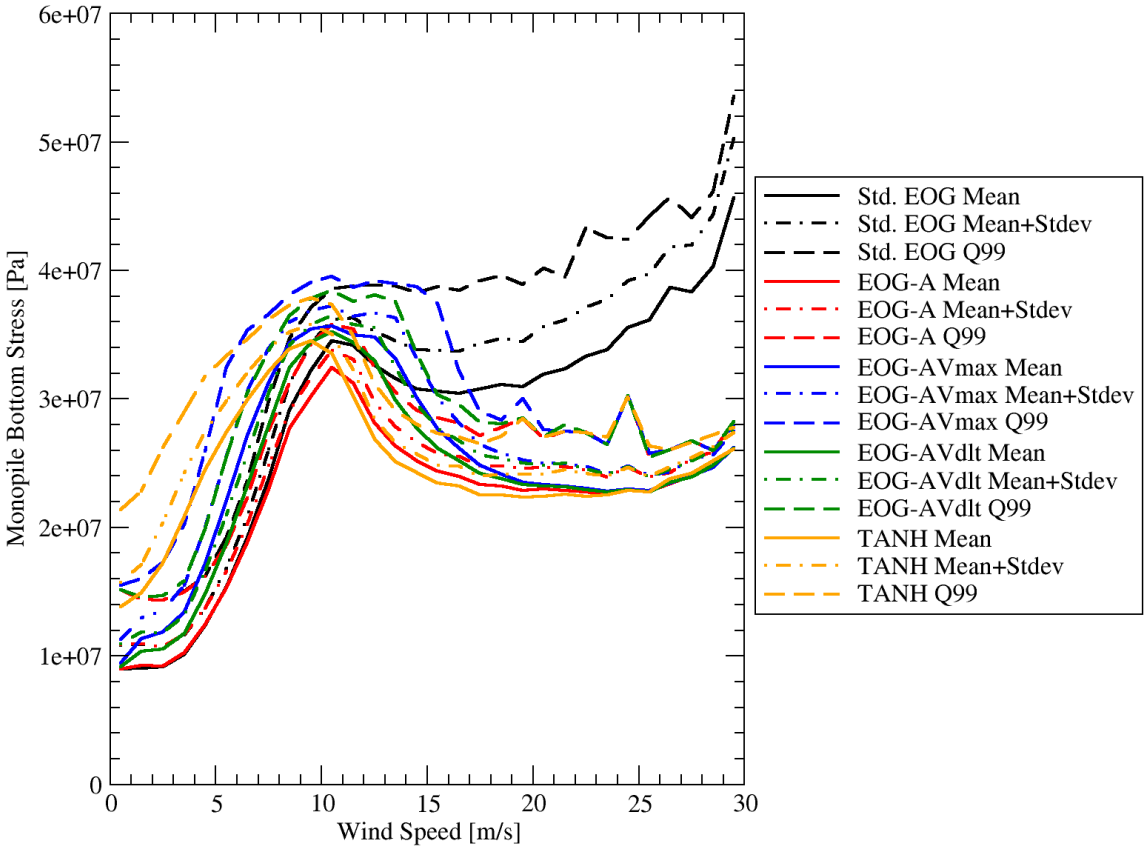

Figure 5.3: Comparison of the monopile stress from the standard EOG function and the tanh gust function.

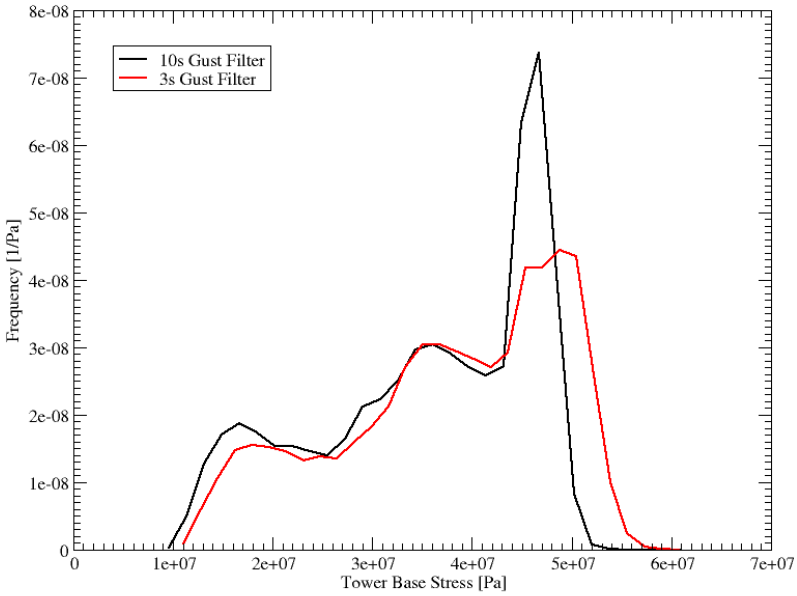

Figure 5.4: The frequency of loads with different gust statistics.

5.3 The impact of the stochastic space of load uncertainty

A series of MC studies were carried out to understand the main drivers of loads for transient ULS simulations. There are two different sets of statistics for the gusts, the effect of these statistics is explored in section 5.3.1. Then the stress in the monopile and tower stress were compared in section 5.3.2. Then the buckling limit state is compared with the stress limit state in section 5.3.3. Then in section 5.3.4 the effect of different transient event on loads it shown. Finally, a preliminary reliability assessment is given in section 5.3.5.

In all cases, the MC simulation was based on 100,000 samples of the Teeside turbine. The simulation uses the same stochastic space as the stationary ULS cases augmented with the gust and grid loss parameters. All the studies were focused on the tower bottom stress, with selected studies looking at the monopile stress and buckling. In most samples, 700s of turbine operation is simulated, where the gust will occur at 300s and the shut-downs will occur at any time between 0-600s.

5.3.1 The effect of gust statistics

Table 5.1 gives two different distributions for gust accelerations. These two sets of gust statistics were included into 2 MC studies. The simulations simulated 100s of operation where the gust would occur at 50s. Figure 5.4 shows the frequency and Figure 5.5 shows the survival function.

5.3.2 Tower and monopile stress

In a number of transient IEC design load cases, the gusts are accompanied by faults or control system actions such as startups and shutdowns. In this study, the MC studies include gusts but not shutdowns or other events. This approach is chosen in order to better compare the impact of the different gust event definitions without other disturbances. In

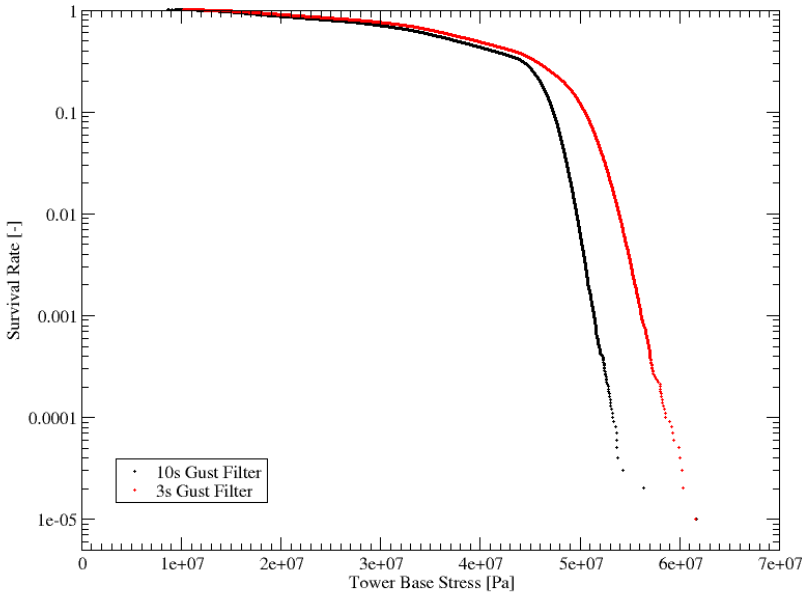

Figure 5.5: The survival function of loads with different gust statistics

both cases, both the tower and the monopile stress was collected and compared in Figures 5.6 and 5.7. The simulations clearly show that tower stress is greater and will be the focus for subsequent studies.

5.3.3 The buckling limit states

This study is based on the same study described in section 5.3.2, instead the buckling limit state was explored in the tower and compared with the stress limit state. The comparison is based on material utilization ratios. The stress utilization ratio is defined as the ratio between the maximum computed stress and the ultimate failure stress, while the buckling utilization ratio is based on the stress in the panels according to the Eurocode standards Eurocode (1993). Figure 5.8 shows for all simulations, that the stress utilization ratio is much greater than the buckling utilization ratio.

5.3.4 The impact of different transient events

A series of different MC studies were carried out to understand what transient events generate the greatest loads. As a reference, the loads from stationary conditions are calculated. Then a simulation is performed with only shutdowns, only gusts and finally gusts and shutdown combined. The results are shown in Figures 5.9 and 5.10. One consequence of the shutdown is the reduction of loads after the event, resulting in a higher frequency of loads at lower levels. Furthermore, the shutdowns alone do not tend to produce loads higher than stationary conditions. Only simulations that included gusts were able to produce higher loads with greater frequency than stationary conditions. Furthermore, simulations with only gusts tended to produce high loads at higher frequency.

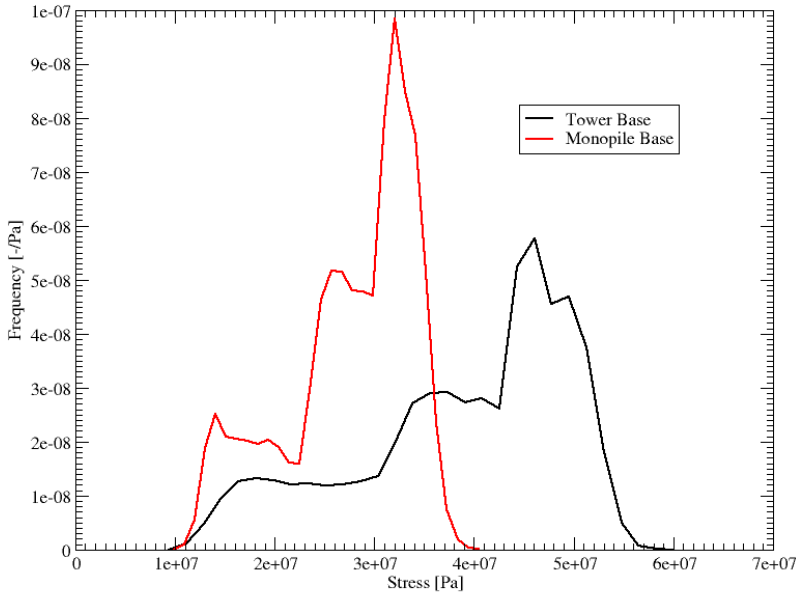

Figure 5.6: Comparison of the probability distributions of tower and monopile stresses.

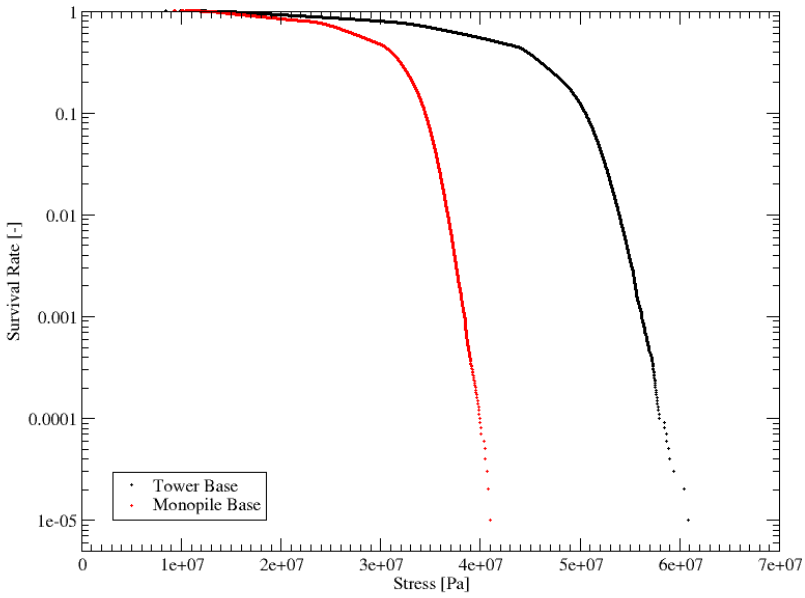

Figure 5.7: The survival function of loads on the tower and monopile.

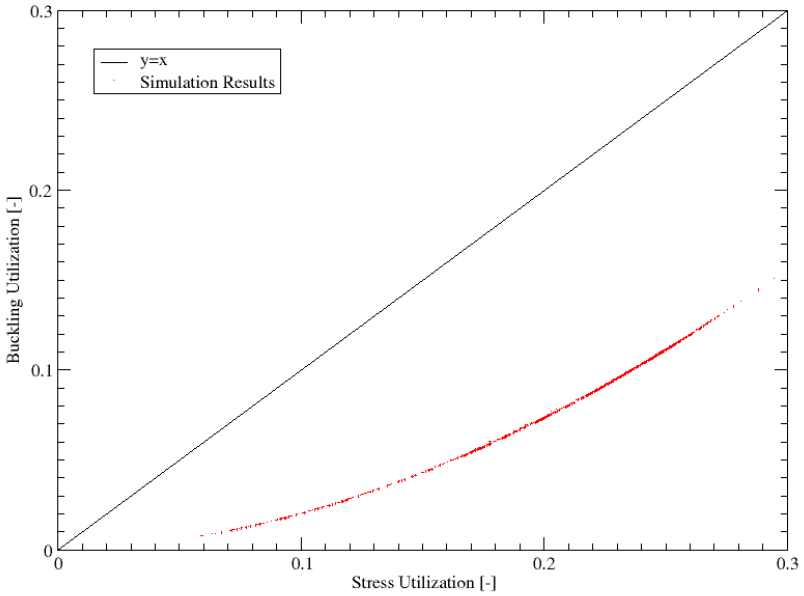

Figure 5.8: Buckling vs stress utilization.

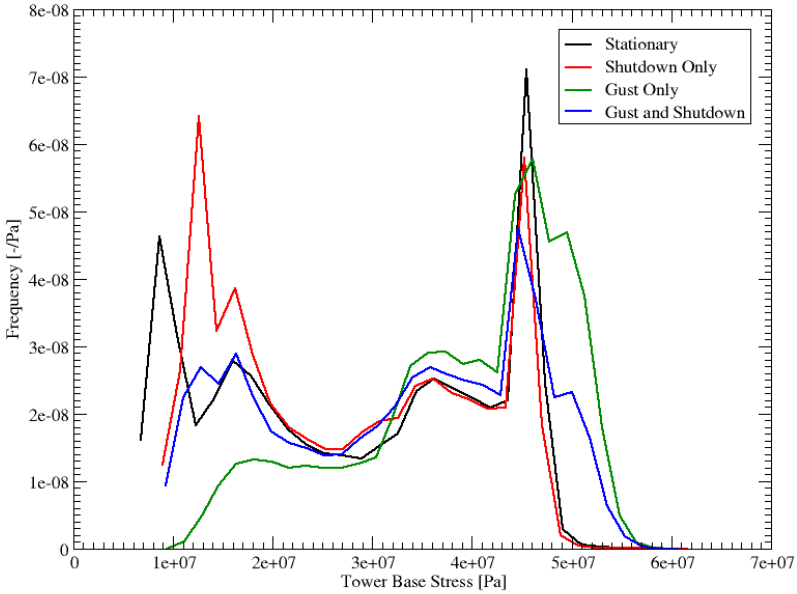

Figure 5.9: The frequency of loads with different transient events.

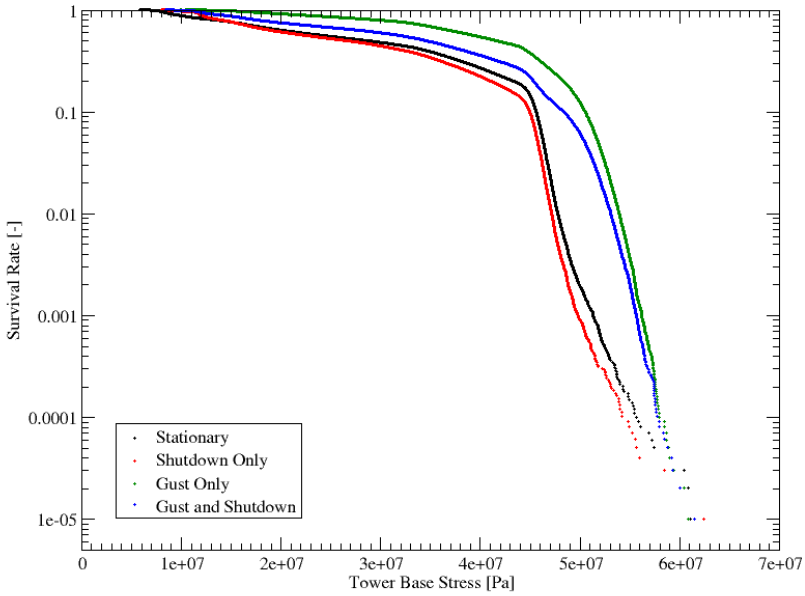

Figure 5.10: The survival function of loads with different transient events.

5.3.5 The dominating load driving events

Finally, the MC that only included gusts was further analyzed to understand the drivers behind the highest loads. This was done by first identify the Pareto front between the distance of samples in the standard stochastic space and the tower stress. This result is shown in Figure 5.11. Then additional points near the Pareto front are collected. From this set, the average direction within the stochastic space of these points is shown in Figure 5.12. The figure shows that the highest loads are driven by the gust acceleration.

5.4 GP model and active learning for the failure probability estimation

5.4.1 Formulation and setting

In this section, the same case study of Teesside OWT is still considered with possible gust and shutdown in operational conditions. For the sake of simplicity, the wave impact on failure is considered of second order and therefore the wave ST seed is fixed, H_s and T_p are fixed to their respective approximated marginal mean: $(3.96m, 3.48s)$, and the wind-wave angle β is set to zero.

We now consider the estimation of the failure probability, on a 620 seconds time interval, characterized by the exceedence of the material resistance threshold ρ by the maximum von Mises stress at the bottom of the OWT tower simulated with Deeplines Wind^{TM}. The von Mises stress will be denoted $\nu_{\mathcal{M}}$ in the following. A total of 7 or 8 continuous input random parameters will be considered: the 10-minutes wind mean: U, the standard deviation: σ_U, the angle between the wind and the nacelle: ζ, the gust acceleration: G_a, the gust rising time: G_{rt}, the gust starting time G_{st}, the shutdown starting time: Sh_t (this parameter is active only when a shutdown is considered) and the failure threshold: ρ.

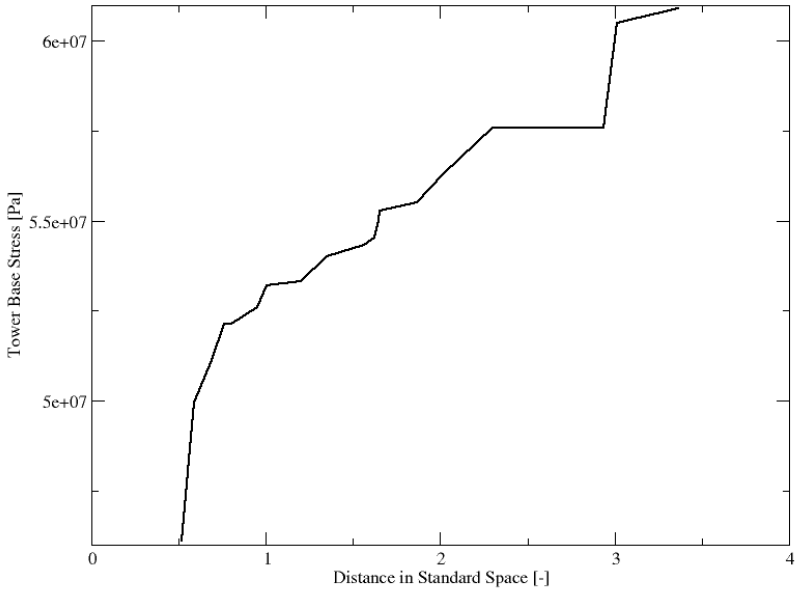

Figure 5.11: The Pareto front between stress and standard space distance.

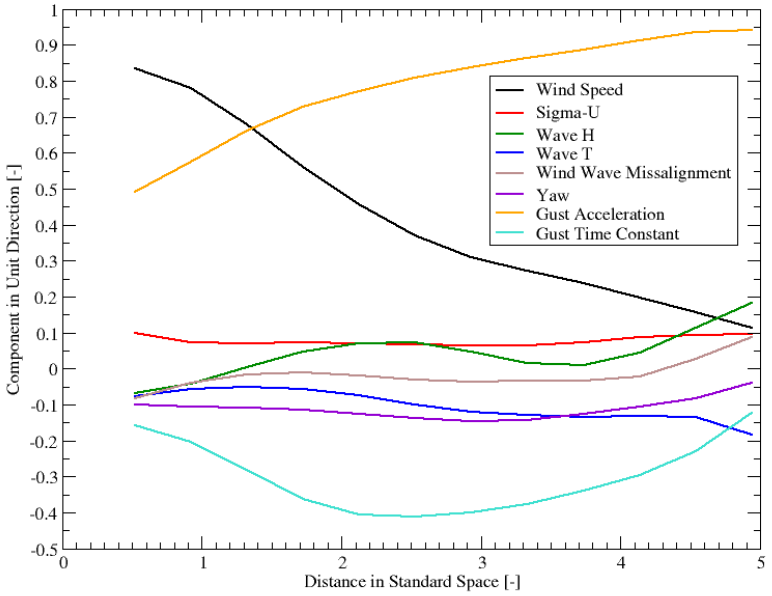

Figure 5.12: The average direction in standard space of points near the Pareto front.

Additionally, two independent random Bernouilli variables are considered: sd which models if a shutdown occurs (1) or not (0) and wd models the two options for the wind direction: open-sea (1) or land (0). Their respective Bernouilli probabilities are $p_{sd} = \mathbb{P}(sd = 1) = 1.9 \times 10^{-4}$ and $p_{wd} = \mathbb{P}(wd = 1) = 0.274$. The value for the shutdown is derived from the 10 per year statistics given by Paz et al. (2023) for Teesside wind farm (worst case of OWT in the farm for Low Voltage number of events 2015 to 2019).

We will denote $\mathbf{X}(sd, wd) = [U(wd), \sigma_U(wd), \zeta, G_a, G_{rt}, G_{st}, \mathrm{Sh}_t(sd)]$ such that $\mathrm{Sh}_t(sd)$ is random if a shutdown occurs and fixed to an arbitrary high value otherwise. Moreover the joint distribution of $(U(wd), \sigma_U(wd))$ is different with respect to the value taken by wd. Therefore, the random vector $\mathbf{X}(sd, wd)$ has dimension 7 when shutdown occurs and 6 otherwise. As previously said, the distribution of the wind and wave that was fitted from met-mast and buoy data in HIPERWIND WP2 cannot be given here for reason of confidentiality. The problem can be formulated as follows:

$$p_f = \mathbb{E}_{sd,wd}\left[\mathbb{P}_{\mathbf{X}(sd,wd),\rho}\Big(S\Big[\mathbf{X}(sd, wd), sd\Big] > \rho \Big| sd, wd\Big)\right] \tag{5.9}$$

where the output S is the following transformation of the von Mises stress:

$$S[\mathbf{X}(sd, wd), sd] = a \times \max_{[0,\Delta T]} \nu_{\mathcal{M}}[t; \mathbf{X}(sd, wd), sd] + b$$

with $\Delta T = 620$ seconds, and the two parameters $(a, b) = (1.1, 135Mpa)$ that were calibrated in order to augment the failure probability and therefore reduce the calculation burden irrelevant for this methodological proof of concept.

5.4.2 Method and results

Two main constraints conditioned our methodological choices: a reduced time to perform the analysis and rare occasional failures of convergence of the Deeplines Wind^{TM} simulator which is not managed by off-the-shelf algorithm. In this context we decided to handle simulation failure manually within an active learning GP strategy.
A brute force approach to estimate (5.9) would require to actively learn four GPs: one for each configuration of the couple of Bernouilli random parameters. But, since the wind direction Bernouilli parameter only impact the wind input distributions and not directly the model, we can only actively learn two GPs respectively with and without shutdown. We will now describe how we build our model when shutdow is active the other case follows the same steps. Let us estimate the probability of failure

$$p_f(1, 1) = \mathbb{P}_{\mathbf{X}(1,1),\rho}\Big(S[\mathbf{X}(1, 1), 1] > \rho \Big| sd = 1; wd = 1\Big) \tag{5.10}$$

where $\mathbf{X}$ is therefore of dimension 7. To alleviate notations and ease the reading we will suppose until specified otherwise sd and wd fixed to one and the conditioning will not be explicitly written. We propose to build a GP surrogate model of the quantity $Y(\mathbf{X}, \rho) = S(\mathbf{X}) - \rho$. Because of the known separability between ρ and S we used a GP model with linear trend: $\beta_0 + \beta_1 \times \rho$. The covariance kernel used is an an-isotropic Matern-$5/2$ with hyper-parameters τ and its length scale vector λ. The full set of hyper-parameters (β, τ, λ) is calibrated by maximizing the model prior likelihood. The learned posterior GP will be denoted $\hat{Y}$. Then the posterior failure probability writes

$$\hat{p}_f = \mathbb{P}_{\mathbf{X},\rho}\Big(\hat{Y}(\mathbf{X}, \rho) > 0\Big)$$

The posterior mean probability (with respect to the GP uncertainty) can be formulated as

$$m_{\hat{p}_f} = \mathbb{E}_{\mathbf{X},\rho}\Big[\Phi\Big(\frac{m(\mathbf{X},\rho)}{\sigma(\mathbf{X},\rho)}\Big)\Big]$$

where Φ is the standard Gaussian cdf, m and σ stand respectively for the posterior mean and variance of $\hat{Y}$. The final proposed estimator of the probability is given by

$$\hat{m}_{\hat{p}_f} = \frac{Vol(\mathcal{X})}{N_{estim}} \sum_{i=1}^{N_{estim}} p(\mathbf{X}_i,\rho_i)\Phi\Big(\frac{m(\mathbf{X}_i,\rho_i)}{\sigma(\mathbf{X}_i,\rho_i)}\Big) \tag{5.11}$$

where p represents the joint distribution of the random vector $(\mathbf{X},\rho)$, $N_{estim} = 10000$, $(\mathbf{X}_i,\rho_i)_{i=1,\dots,N_{estim}}$ is a Sobol sequence generated in the input set $\mathcal{X} = [3m/s, 25m/s]\times[0m/s, 6m/s]\times[-8^o, 8^o]\times[0ms^{-2}, 3ms^{-2}]\times[1s, 23s]\times[0s, 600s]\times[0s, 600s]\times[100s, 600s]$ and $Vol(\mathcal{X})$ is its volume. A pseudo confidence interval is also estimated by using the quantiles of the GP leading to

$$\hat{q}_+ = \frac{Vol(\mathcal{X})}{N_{estim}} \sum_{i=1}^{N_{estim}} p(\mathbf{X}_i,\rho_i)\mathbb{1}_{\{m(\mathbf{X}_i,\rho_i)+2\sigma(\mathbf{X}_i,\rho_i)>0\}} \tag{5.12}$$

and $\hat{q}_-$ similarly defined with $+2$ replaced by -2 in the previous formula.

We can now describe our adaptive strategy. A GP surrogate is build on a relatively small initial DoE $N = 70$. The surrogate is then actively improved using the SUR-Bichon active learning criterion introduced in Duhamel et al. (2023) to augment the DoE, with the aim of accurately estimating the failure domain. Four batches of 25 points and a final one of 30 points are iteratively added following a batch version of the SUR-Bichon criteria. The final number of simulation for learning is therefore two hundred. The SUR-Bichon criteria was optimized on a large discrete set of ten thousand points. Finally a large space-filling design $N_{estim} = 10000$ coupled with the actively learned final GP surrogate is used to estimate the probability with the posterior mean probability estimator (5.11) and the estimated bounds (5.12) are also calculated.

GP model construction with shutdown. In Figures 5.13, 5.14, 5.15 and 5.16 we present the evolution of the GP hyper-parameters along the batch iterations. The constant trend does not change significantly along the different active learning iterations. The coefficient β_1 is estimated to approximately -1 which is indeed the true value. The variance has no particular behavior. The plotted correlation length scales are normalized by the length of the support of their respective variables; so that the greater above 1 the less variation is expected in that dimension and vice versa. We notice that the mean wind, the gust acceleration and the gust beginning time are those that generates the most variation on the output.

In Figures 5.17 we present a parallel plot of the input and corresponding output Y and their associated batch of points. The line are colored by level of the output. The same parallel plot colored by the membership to the batch set (last column) is presented in Figure 5.18. We can notice that the SUR-Bichon iterations enabled to actively add points around the failure area for Y i.e. around zero. It seems clear that the leading parameter to failure is the material resistance. The other variables were considered by the criteria

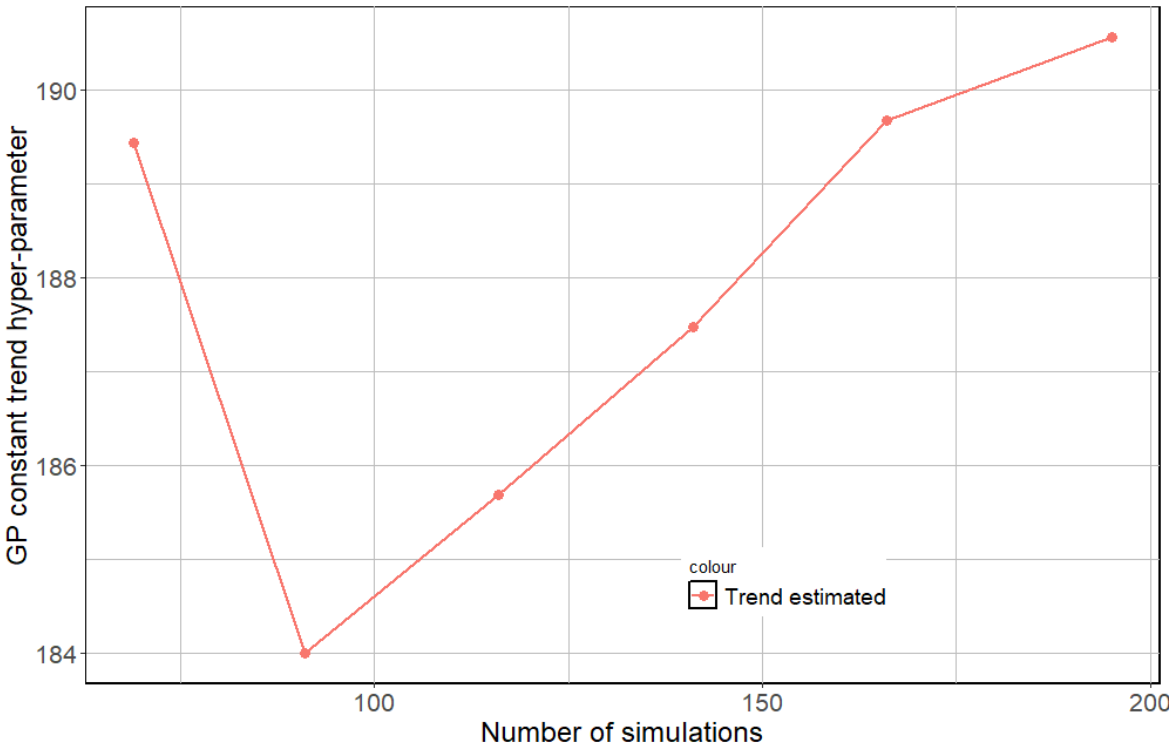

Figure 5.13: Evolution of the constant trend β_0 along the active learning iterations with shutdown in the model.

uniformly important in term of reaching the limit threshold. The enrichment criterion therefore spreads points almost uniformly on the support of these variables. Remember that the distribution of the parameters are not taken into account for learning the GP. Indeed, without a priori, we chose to have a good model on the whole support of the variables. Finally, the integrated mean square error between the GP model and the true response was estimated on an independent LHS-maximin validation DoE of size five hundred at each stage of the active learning process. The IMSE start approximately around 14 and decrease down to approximately 11 at the end of the learning. This seems to indicate that the model has good predictive quality since the standard deviation of the response overall the input space is of the order of 150.

GP model construction without shutdown. In Figures 5.19, 5.20, 5.21 and 5.22 we present the evolution of the GP hyper-parameters along the batch iterations. The same conclusion, as in the shutdown case, can be drawn for the trend coefficients and the variance hyper-parameter. In term of length scales the mean wind and gust acceleration remain important and here are joined by the gust length time and σ_U. In Figures 5.23 and 5.24 we present the same parallel plot, as in the shutdown case, of the input and corresponding output Y and their associated batch of points. The same conclusion can be drawn about the first order importance of the material resistance parameter ρ. Also, the same predictive quality of the GP model was observed.

Failure probability estimation. We now present in Figures 5.25, 5.26, 5.27 and 5.28 the failure probabilities and their bounds estimated for the four possible cases. By weight-

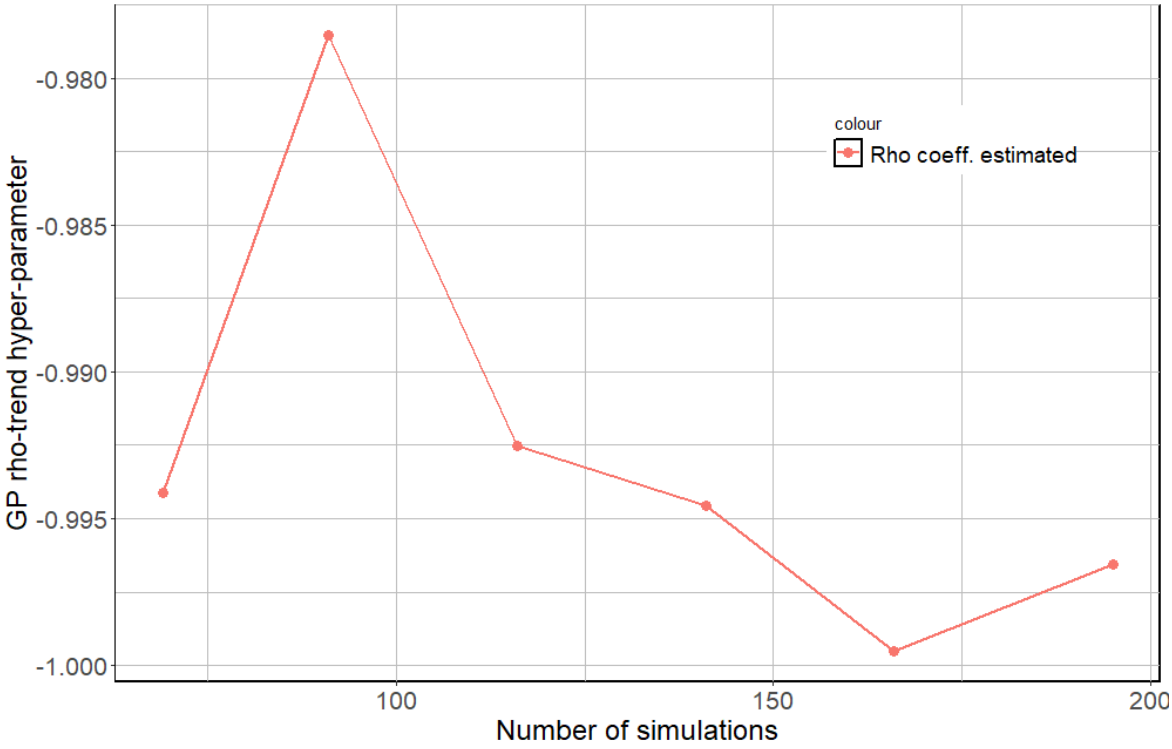

Figure 5.14: Evolution of the ρ coefficient β_1 along the active learning iterations with shutdown in the model.

ing these four probabilities by the corresponding probabilities $\mathbb{P}(sd, wd)$ the overall failure probability is estimated to be of the order of 10^{-8}. The evolution of the estimation of p_f given (5.9) is depicted in Figure 5.29. One may note a significant reduction of the pseudo bound distance on the failure probability with shutdown and with wind coming from land at simulation 132 (Figure 5.28) which would be interesting to further investigate.

Opening We can mention that with more time to introduce an automatic management of the hidden simulator failure, we would suggest to tackle (5.9) with the Bayesian subset simulation strategy (Bect et al., 2017) which seems well adapted to a setting with dimension less than a dozen and time consuming simulations.

5.5 Conclusions of the Transient ULS study

This section presented ULS reliable methods dedicated to the transient event with a gust or a grid loss. The gust was defined according to a new function fitted from several years of observations in Kelly and Vanem (2022) and compared to the EOG of IEC standard IEC (2019a). Then a massive MC sampling underlined the role of the gust acceleration in increasing the maximum von Mises stress on tower base when compared to ULS stationary event conducted on similar statistics. To reduce the computation cost of the MC sampling, a method is presented which involves a GP surrogate iteratively enriched according to the SUR-Bichon active learning criterion of Duhamel et al. (2023). We were able to prove that with two hundred simulations a stable estimation of the transient failure probability could be estimated (1.09×10^{-8}). The pseudo confidence interval is nonetheless relatively

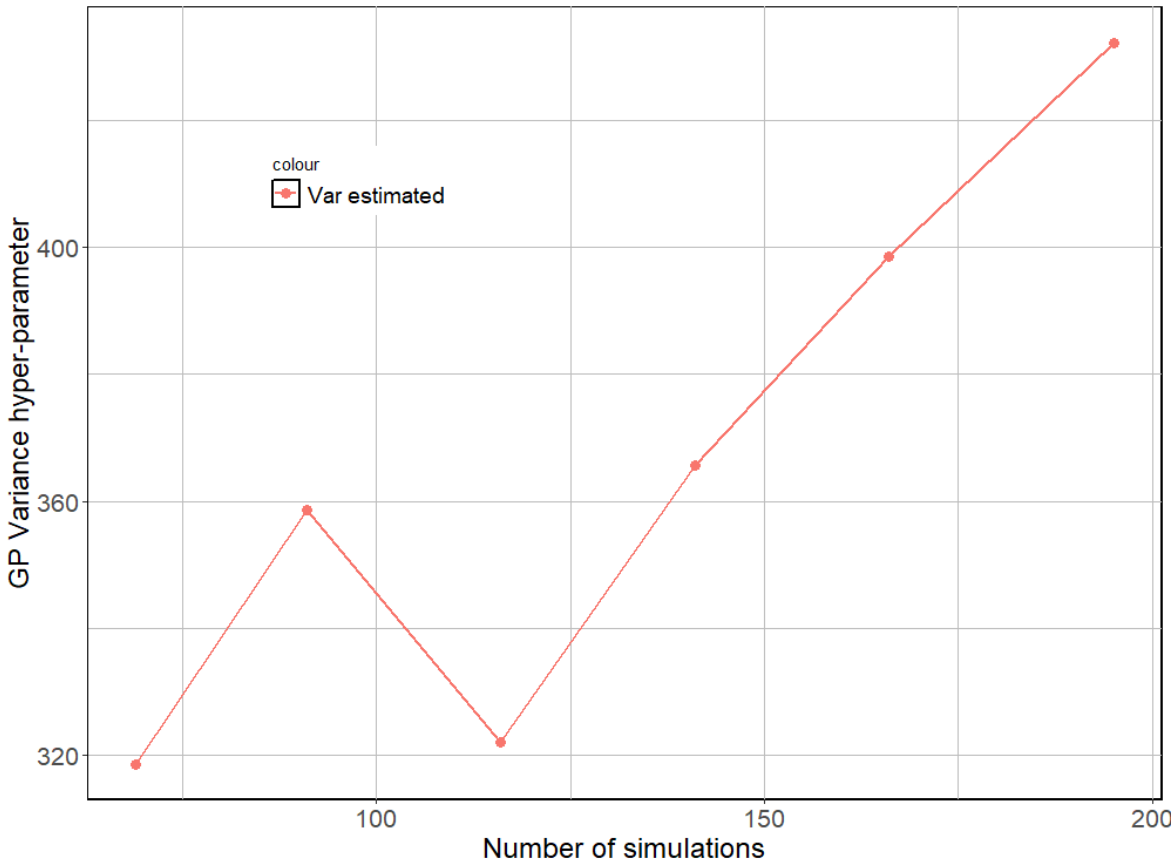

Figure 5.15: Evolution of variance τ along the active learning iterations with shutdown in the model.

large $[3.78 \times 10^{-10}, 1.45 \times 10^{-7}]$ and could be improved. Moreover the active GP model seems to strongly indicate that at first order the material resistance is of most importance w.r.t. failure. Reducing uncertainty on this latter seems essential. The gust acceleration and the wind speed mean seem also to be strong source of variation of the difference Y between the maximum von Mises stress S on tower base and the material resistance ρ. To better understand the impact of the parameters (other than the resistance) on the studied moment we would suggest to directly build an active GP model on S instead of Y. This would help to compare the results obtained with the analysis of the correlation lengths on Figure 5.22 and that of the average distances around a Pareto front in Figure 5.12.

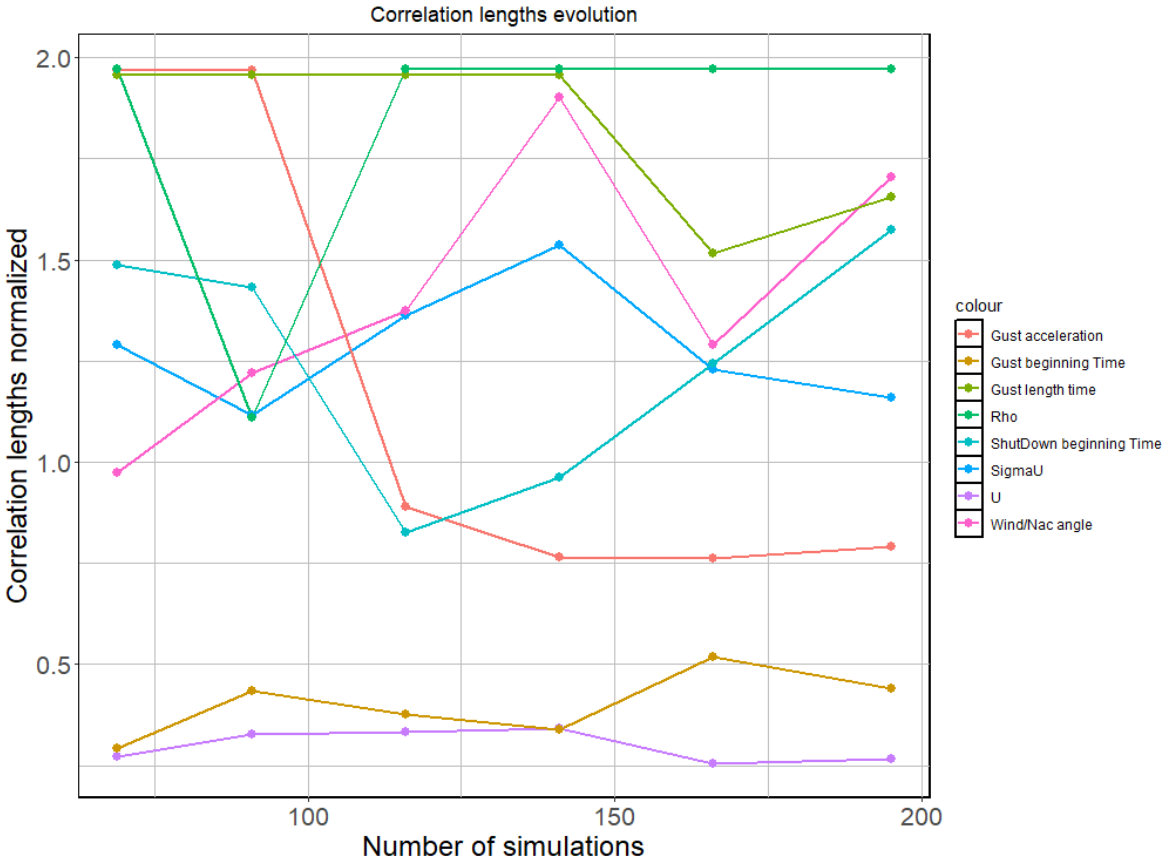

Figure 5.16: Evolution of the correlation lengths hyper-parameters along the active learning iterations with shutdown in the model.

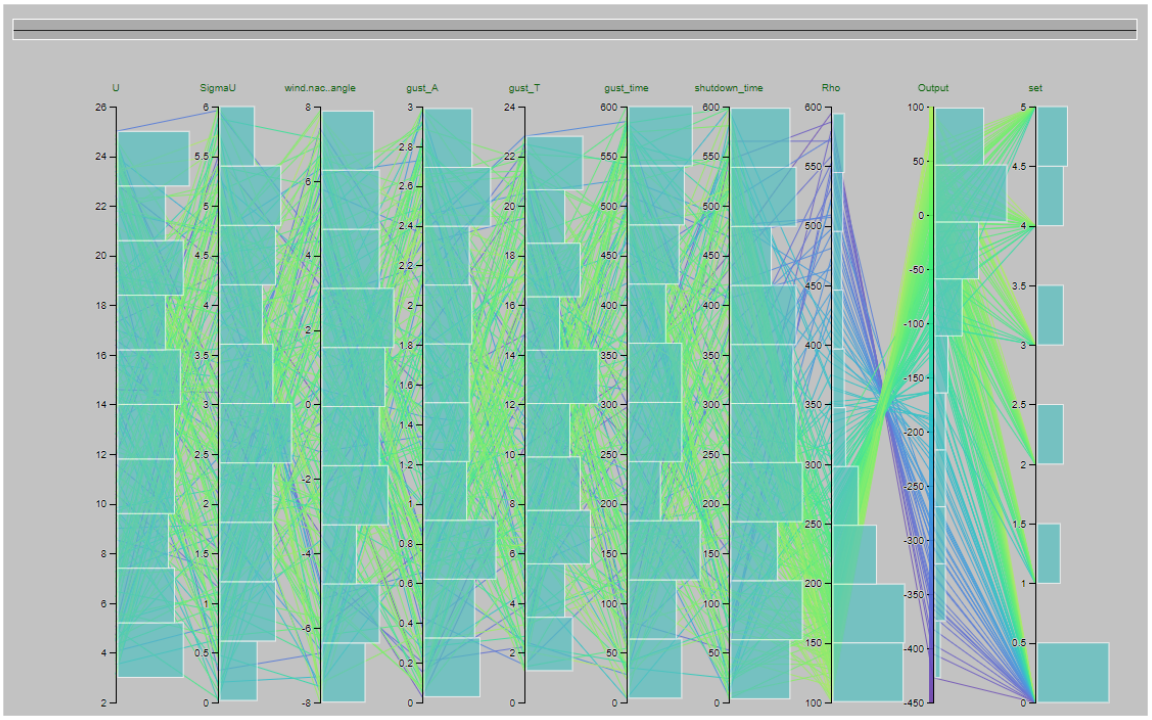

Figure 5.17: Parallel plot showing the Input and Output (Y) distribution of the training and learned design points for the goal-oriented GP construction with shutdown. Coloration by level of the output.

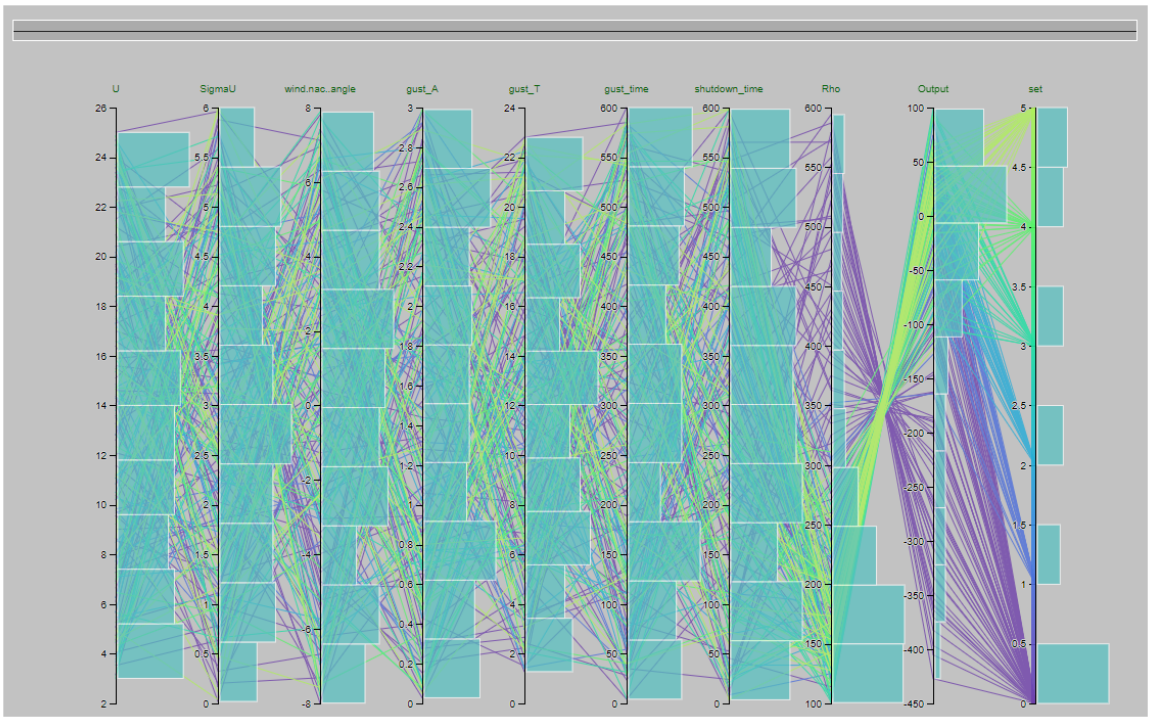

Figure 5.18: Parallel plot showing the Input and Output (Y) distribution of the training and learned design points for the goal-oriented GP construction with shutdown. Coloration by membership to the corresponding batch of points.

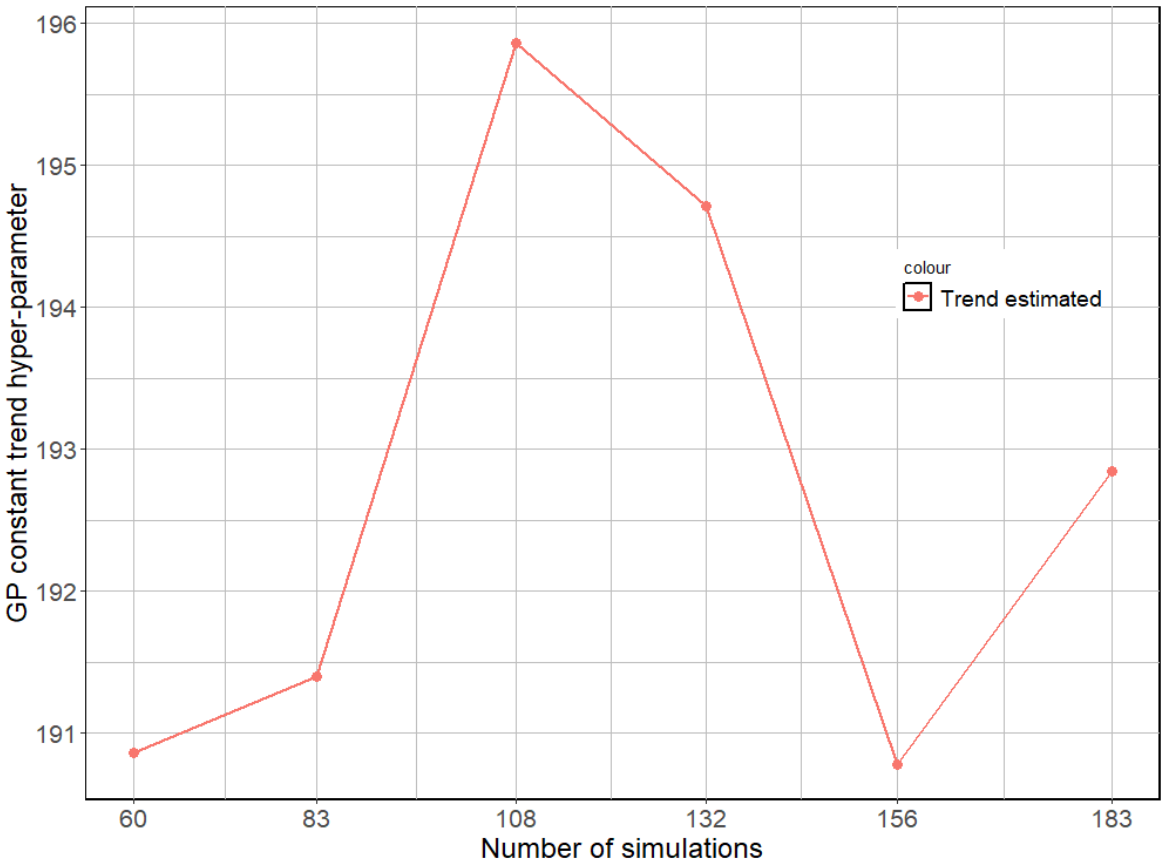

Figure 5.19: Evolution of the constant trend β_0 along the active learning iterations without shutdown in the model.

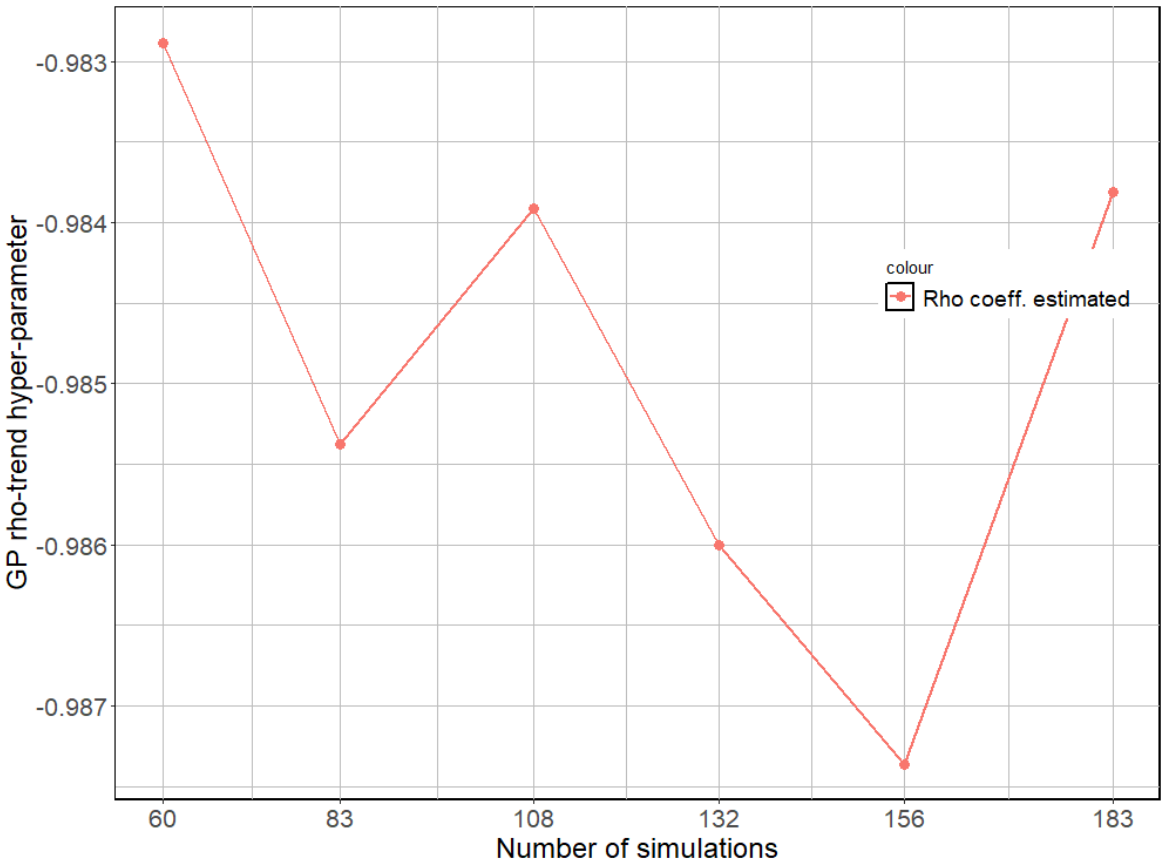

Figure 5.20: Evolution of the ρ-coefficient β_1 along the active learning iterations without shutdown in the model.

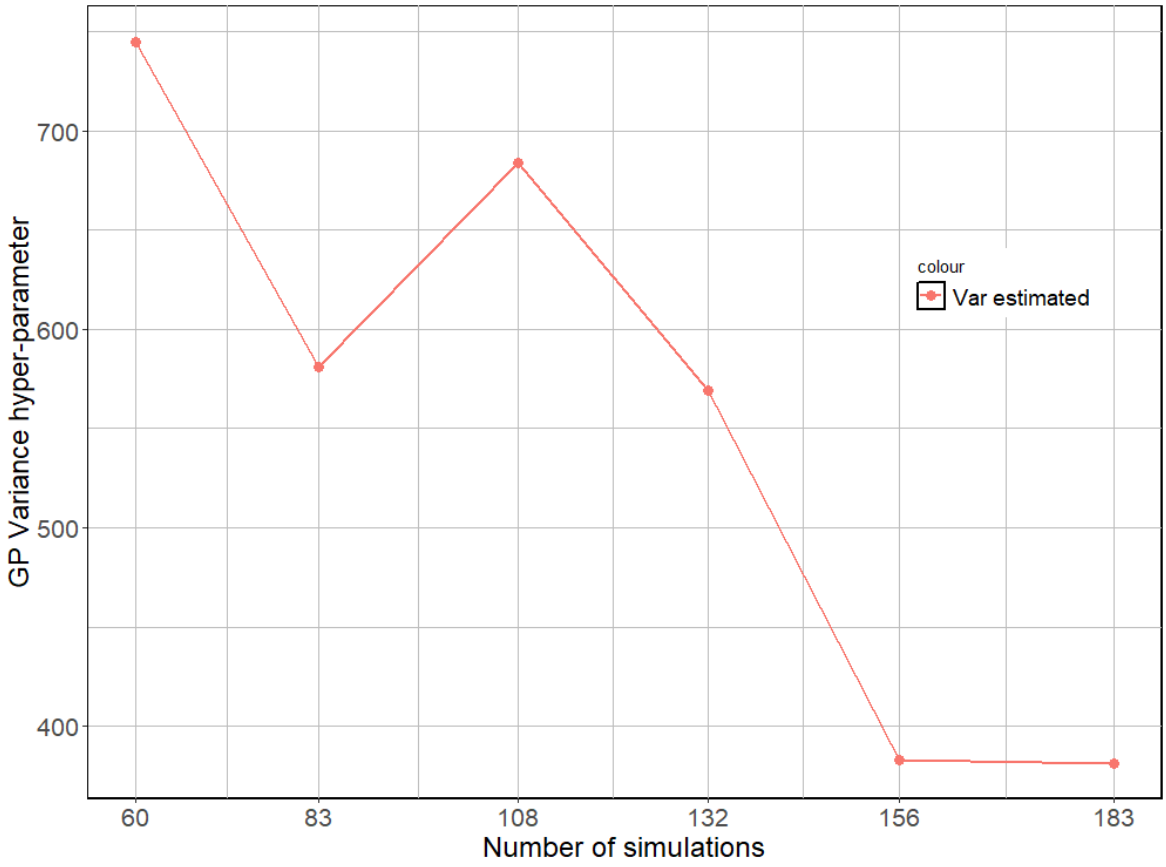

Figure 5.21: Evolution of the variance τ along the active learning iterations without shutdown in the model.

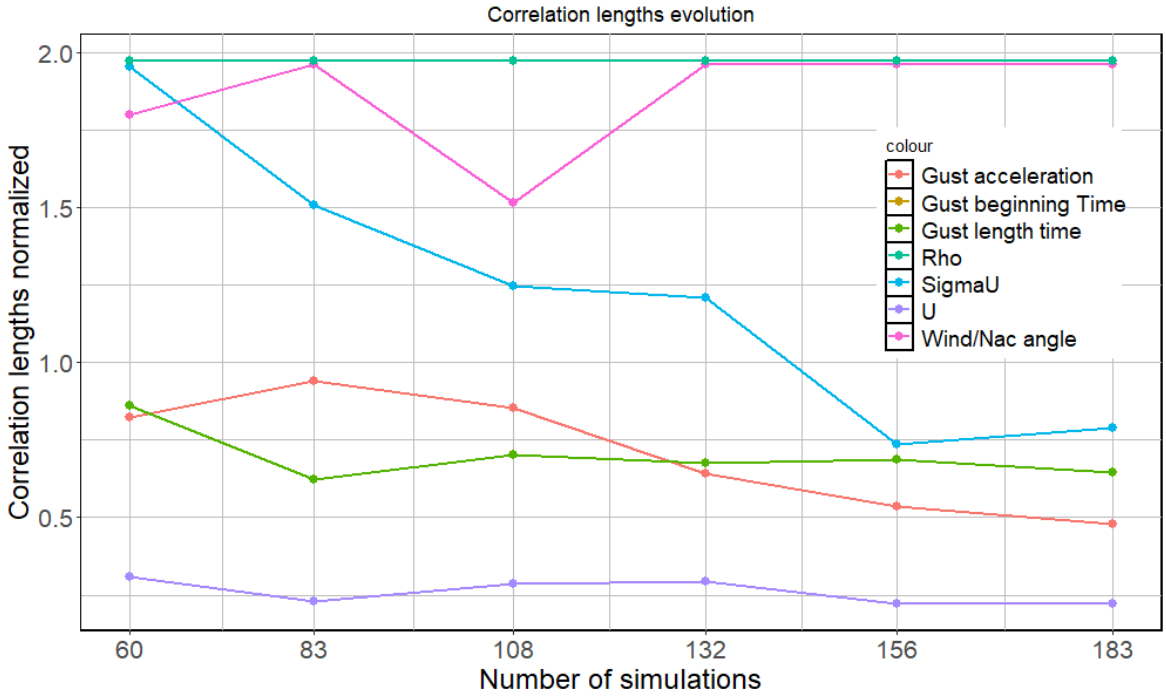

Figure 5.22: Evolution of the correlation lengths hyper-parameters along the active learning iterations without shutdown in the model.

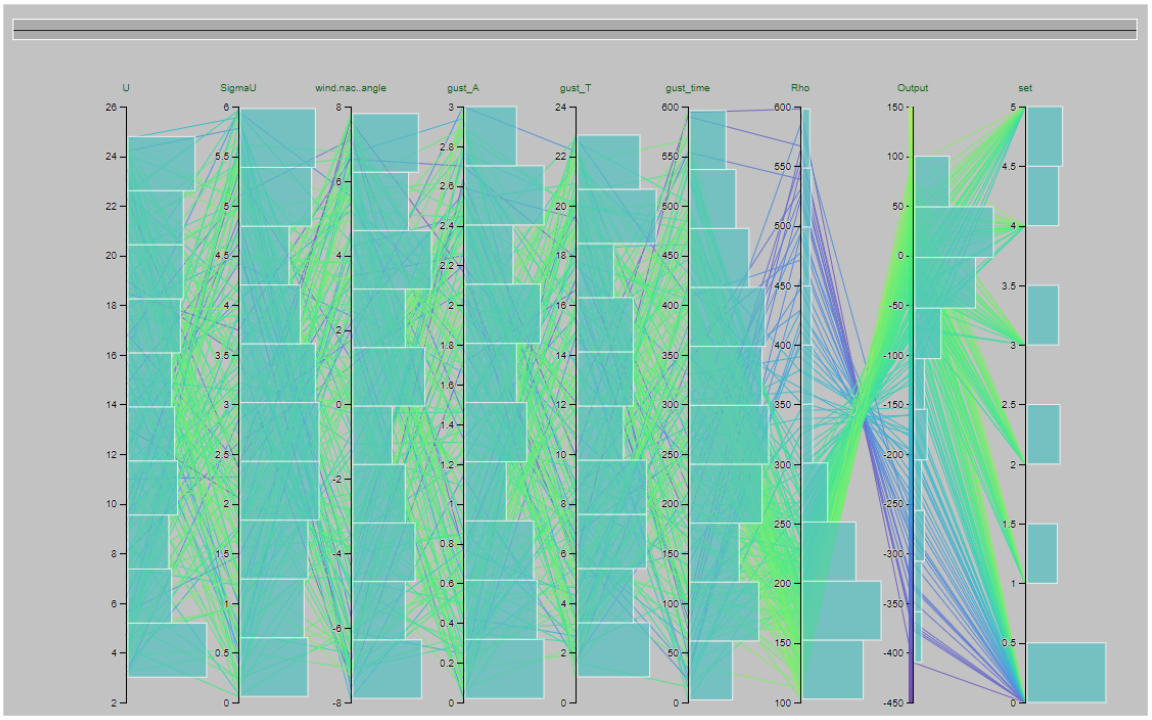

Figure 5.23: Parallel plot showing the Input and Output (Y) distribution of the training and learned design points for the goal-oriented GP construction without shutdown. Coloration by level of the output.

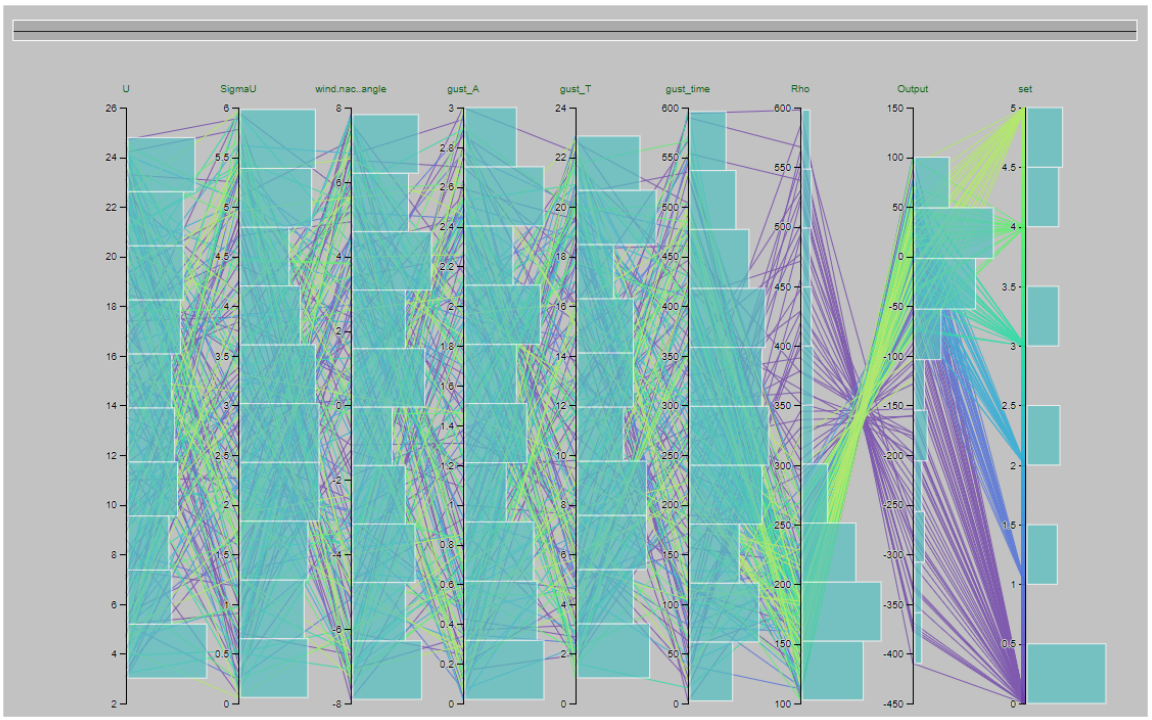

Figure 5.24: Parallel plot showing the Input and Output (Y) distribution of the training and learned design points for the goal-oriented GP construction without shutdown. Coloration by membership to the corresponding batch of points.

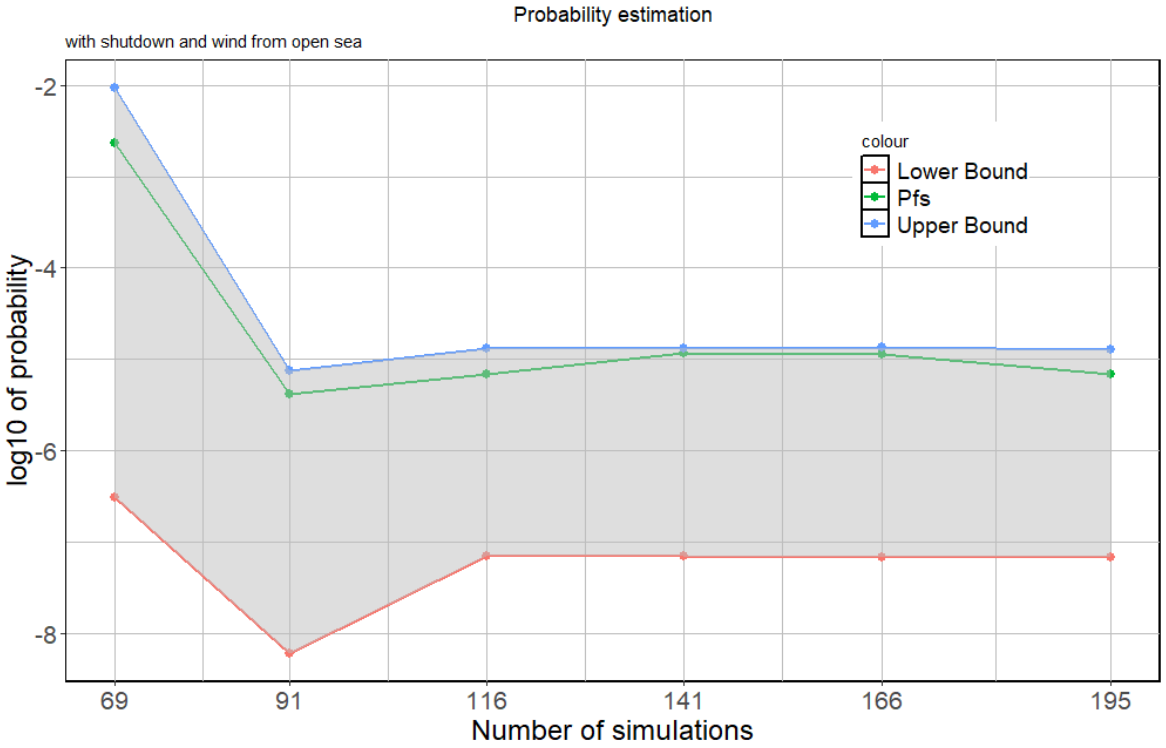

Figure 5.25: Failure probability estimation with shutdown and wind from open sea along the active learning iterations.

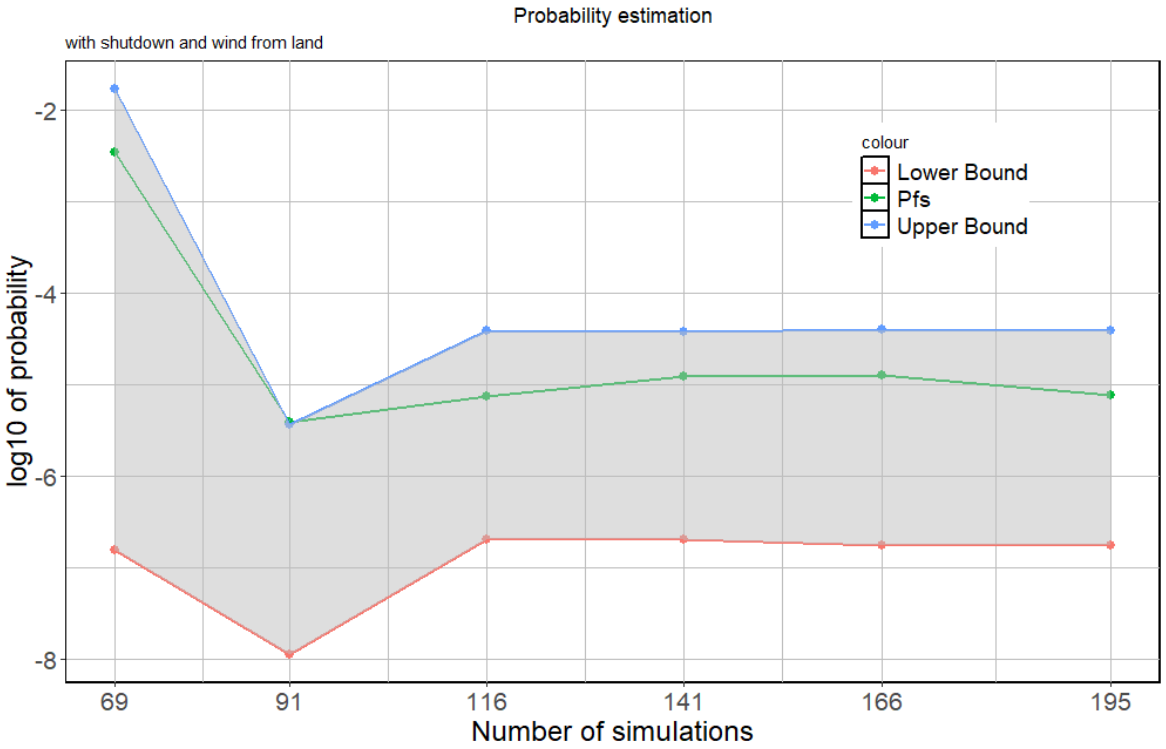

Figure 5.26: Failure probability estimation with shutdown and wind from land along the active learning iterations.

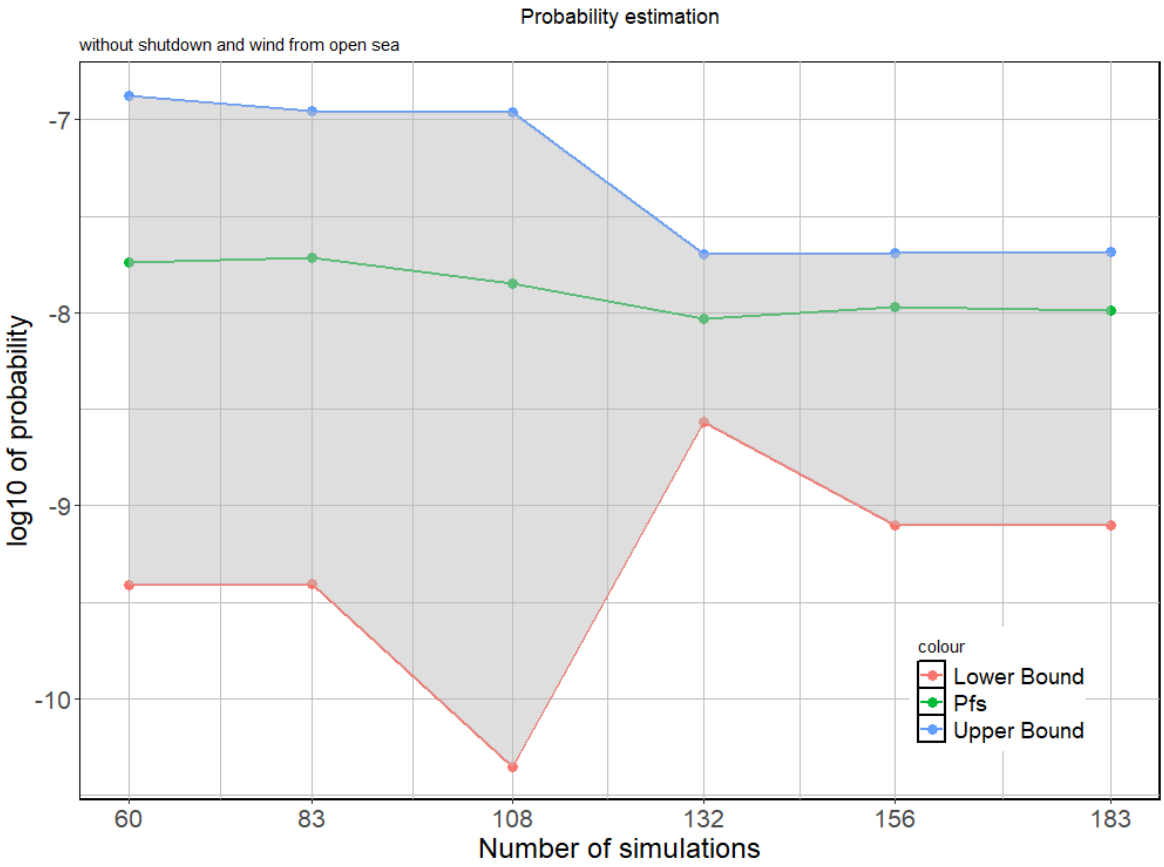

Figure 5.27: Failure probability estimation without shutdown and wind from open sea along the active learning iterations.

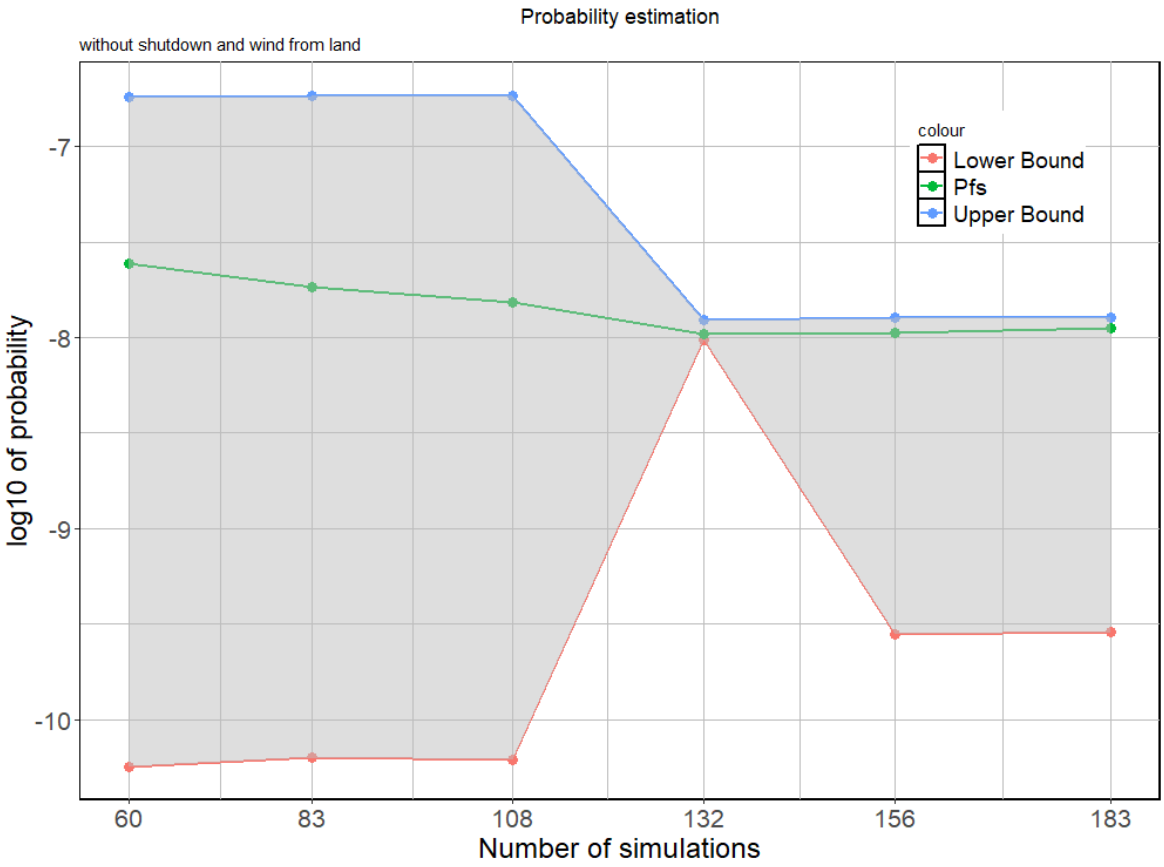

Figure 5.28: Failure probability estimation without shutdown and wind from land along the active learning iterations.

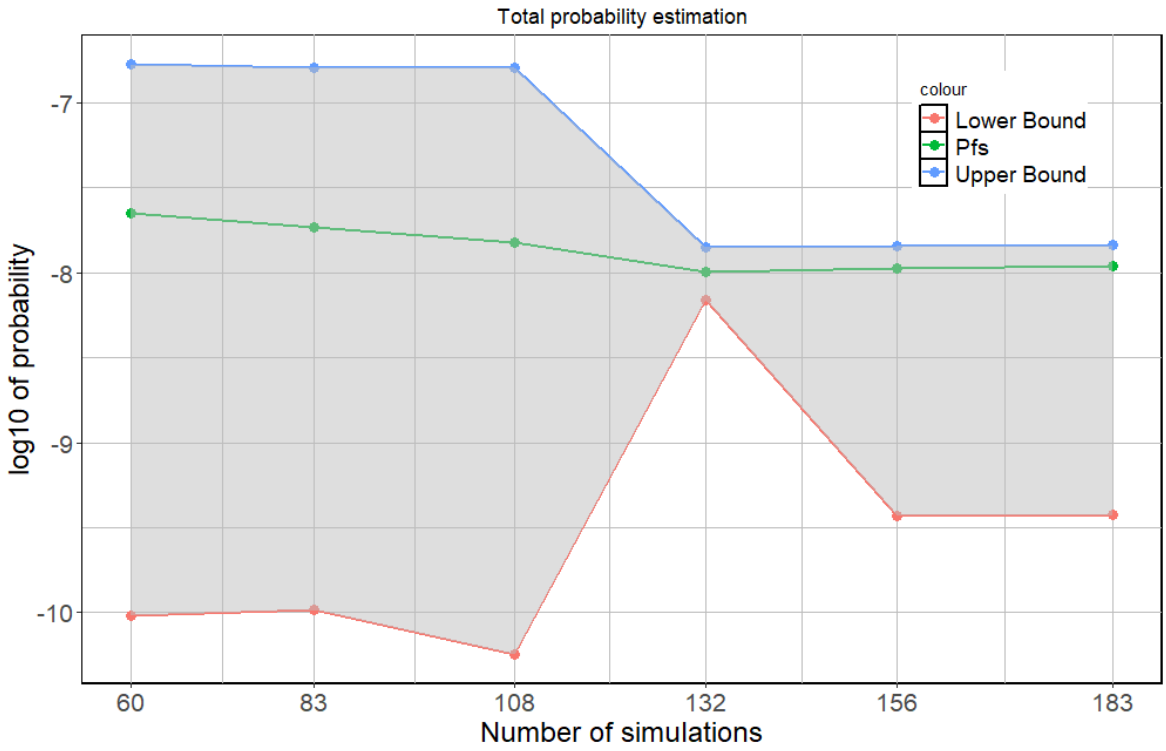

Figure 5.29: Failure probability estimation with transient input wind along the active learning iterations.

6 Application to Teesside case study and design optimization

In this section, we consider an offshore fixed wind turbine of the Teesside wind farm of EDF (UK) EDF (2014).

Two analyses are carried out on this case:

1. first, the sequential sampling described in section 4.1.3 is applied to estimate an ULS failure probability of the wind turbine;
2. then, an optimization of the thickness of the monopile and tower is done to reduce the manufacturing cost of the structure while satisfying several constraints that are described in the dedicated section.

6.1 Case study presentation

The Teesside wind farm is composed of 27 Siemens SWT 2.3MW turbines and was commissioned in 2013, Figure 6.1. Each turbine of rotor diameter about 93m is mounted on a steel foundation consisting of a conical steel transition piece (TP) section, with largest diameter of 4.9m, grouted onto a cylindrical steel monopile section of 4.6m diameter, see Figure 6.11. The steel material for monopile and TP is S355NL. It was assumed in this work that the same steel was used for the tower of Teesside OWT. The yield stress depends on the thickness, which gives a mean value of 315 MPa for the monopile and 335 MPa for the tower.

Several aero-servo-hydro-elastic models (HAWC2, Deeplines Wind^{TM} and DIEGO) of this OWT were built during WP1 of HIPERWIND, with a benchmark campaign comparing successfully their results on various loading cases including irregular waves and turbulent winds, and checking the controller behaviour in a wind step analysis. The soil-monopile interface is not represented by the classical API p-y method Carswell et al. (2015) but with a simpler equivalent stiffness 6x6 matrix. The latter takes into account the embedment depth.

6.1.1 Failure probability

We recall that the ULS failure probability is defined as:

$$p_f = \mathbb{P}_{\zeta,\eta(.,\xi),\nu(.,\xi)}\left(\max_{[0,\Delta T]} s(t;\zeta,\eta(.,\xi),\nu(.,\xi) > \rho\right) \tag{6.1}$$

where, for the Teesside case study:

- ΔT is equal to 10 minutes;
- ζ is a random variable representing the model uncertainties on the yaw misalignement (i.e. the angle between the nacelle and the wind direction);
- ξ is a 5D random vector composed of the following random variables:
  - U_{hub}: the mean wind speed at hub height;
  - σ_{hub}: the temporal standard deviation of the wind speed at hub height;
  - H_s: the significant waveheight;

Figure 6.1: View of the turbines supported by monopiles of the Teesside wind farm, copyright EDF Renewables UK.

  - T_p: the peak period;
  - β: the wind-wave misalignment.
- $\eta(.,\xi)$ and $\nu(.,\xi)$ represent respectively the ST sea elevation and wind velocity. They are both time-dependent stationary GP parameterized respectively by (H_s, T_p) and (U_{hub}, σ_{hub});
- s is the von Mises stress of the monopile at the mudline and in parked (idling turbine) condition. The choice of the quantity of interest is justified in section 6.2.
- ρ is the yield strength of the monopile and tower steel which is also considered stochastic.

This selection of uncertainty aims at keeping important effects on ULS of this OWT structure while reducing as much as possible the dimension of the reliability problem. For instance, the wind and wave orientations are grouped in a single misalignement variable thanks to the isotropy of the monopile foundation and as the turbine realigns with the wind thanks to yaw bearing system. Similarly, several model uncertainties which have been characterized in previous deliverables of HIPERWIND (e.g. wake model uncertainties in Ardillon et al. (2022), hydrodynamics and aerodynamics model uncertainties in Peyrard et al. (2022)) have not been selected, assuming they have smaller influence than the ones listed above on ULS. This choice required to complete the scope with the project timeline is worth to be reconsidered in future works to take advantage of these quantifications which are an important result of HIPERWIND project.

Furthermore, as in Muskulus and Schafhirt (2015), an uncertainty scaling coefficient (mean 1 and CoV 0.2) was also considered initially on each term of the matrix representing the soil/monopile interface. This uncertainty is deemed to be significant to the difficulty of

characterization of soil heterogeneity with geotechnical measurements Carswell et al. (2015). The latter reference showed the importance of the embedment depth on the monopile SLS bending. The equivalent stiffness matrix takes it into account, so that the scaling factor uncertainty also represents its effect. Although this parameter is known to have a major influence on the fatigue of monopile supported OWT, a simple parametric study suggests it has small influence on the ULS for this case study as illustrated in Figure 6.2. In this figure, the maxima of the von Mises stress at the mudline is computed considering all input parameters at their mean values and then comparing to the case where each parameter is at its mean value except one which takes the extreme values of its marginal distribution. We see that the quantity of interest is not sensitive to the soil stiffness. Consequently, it was decided to discard it in the reliable study detailed hereafter.

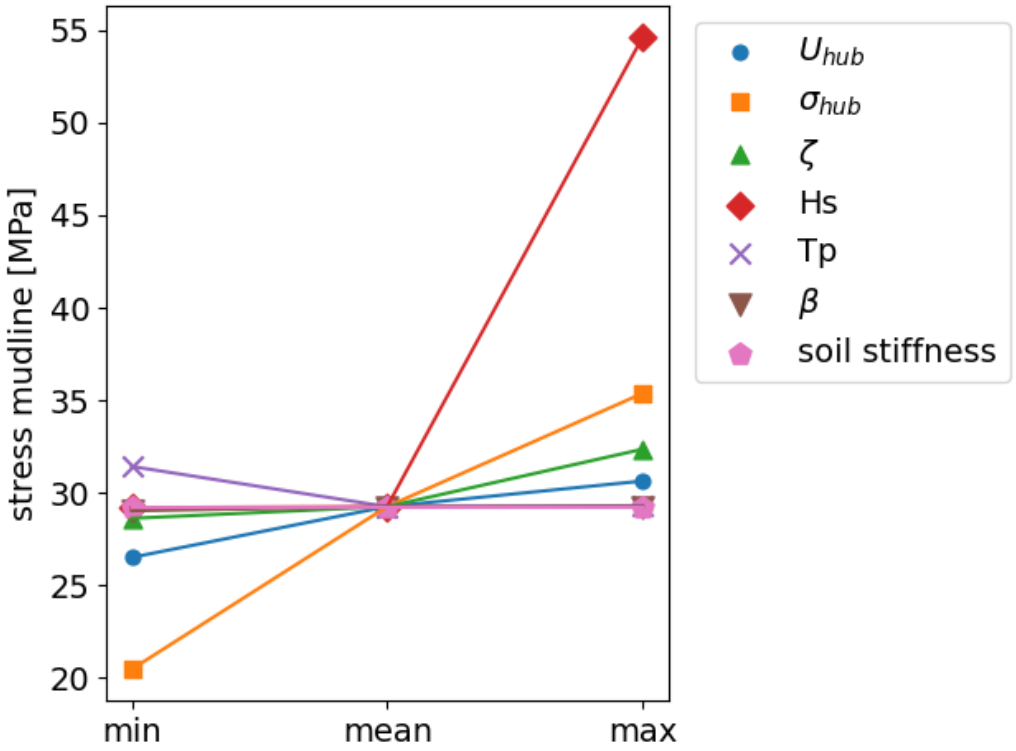

Figure 6.2: Parametric study of max von Mises stress (MPa) at mudline.

6.1.2 Distribution of the uncertainties

For this case, we consider two sectors of wind direction:

- one sector with a wind direction $\in [0°, 120°] \cup [330°, 360°]$ corresponding to wind from open sea (with probability $p_{sea} = 0.274$);
- one sector with a wind direction $\in (120°, 330°)$ corresponding to wind from land (with probability $p_{land} = 0.726$).

One pdf of ξ is fitted for each sector. The fitting method and the description of the resulting distribution is given in Deliverable 2.3 of the Hiperwind project (Kelly and Vanem (2022))).

The failure probability is thus $p_f = p_{f|sea} \times p_{sea} + p_{f|land} \times p_{land}$ where $p_{f|sea}$ and $p_{f|land}$ are the ULS failure probability considering ξ respectively from the first and second sector.

Moreover, the marginal distribution of U_{hub} is truncated below 25m/s since the turbine is in parked condition.

The yaw misalignment ζ is represented by a random variable following a uniform distribution between [-8°,8°] (cf IEC 61400-1).

For the yield strength, a log-normal distribution with coefficient of variation 0.1 is chosen to represent the uncertainties as proposed in Muskulus and Schafhirt (2015). The mean of this variable depends on the material and the thickness of the monopile at the mudline. Here the material is the steel S355NL which implies a mean of ρ at 315 MPa.

6.2 IEC 61400 Load Evaluation of the Teesside case

To ensure the reliability of an offshore wind turbine, the standard IEC 61400 IEC (2019b) requires to run the wind turbine model for a list of operation and environmental configurations called Design Load Case (DLC). In this section a full IEC 61400 Design Load Basis (DLB) calculations is carried out for the Teesside turbine. This analysis allows us to identify the most critical DLC.

Let us first indicate that only plasticity ULS at the tower basis and monopile at mudline were considered as potential ULS. In addition to these two well known mechanisms, often considered in the ULS reliability analyses of OWT supported on monopile, several other limit states need to be checked to validate a design in a real industrial case (e.g. blade root bending, top tower acceleration etc..). Our goal here is not to realize a complete industrial design check and optimization, which would have been out of the scope of HIPERWIND objectives, and would have required missing information on the structure. Our goal is actually to demonstrate the feasibility of the new ULS reliability computation on a realistic case, for which the two selected limit states are enough representative.

Figure 6.3 shows the von mises stress at the tower bottom for each DLC and Figure 6.4 shows the monopile stress at mudline. These figures are obtained using DTU's simulator (HAWC2). The 3.x and 6.x DLCs tend to give the highest loads. However, the controller used for these simulations has not be tuned to give low loads in start-up and tends to produce high rotor speeds in start-up. This can be seen in Figure 6.5. Additionally, some of the waves generated for the 6.x DLC were not physical.

Indeed, the initial water depth configuration from HIPERWIND WP1 model setting was chosen to be 12.5m. However, in WP2 characterization of the wind and wave joint probability Kelly and Vanem (2022), the water depth considered was that of 15m where the data were collected, at an ocean area outside Teesside. Note that in Kelly and Vanem (2022) a truncation limit of 13m was computed for 15m water depth, following a breaking wave criterion given by EDF R&D on H_s and T_p (i.e. H_s update when about 30% highest waves of the sea states are identified as breaking).

This incompatibility issue was solved by updating the water depth of the model to 14.9m, as this value is also found for turbine in the farm.

From EDF design analysis, the selected DLCs are in particular DLC1.3, DLC1.6 and DLC6.1. The DLC6.2 with strong misalignement is consequently discarded in the following,

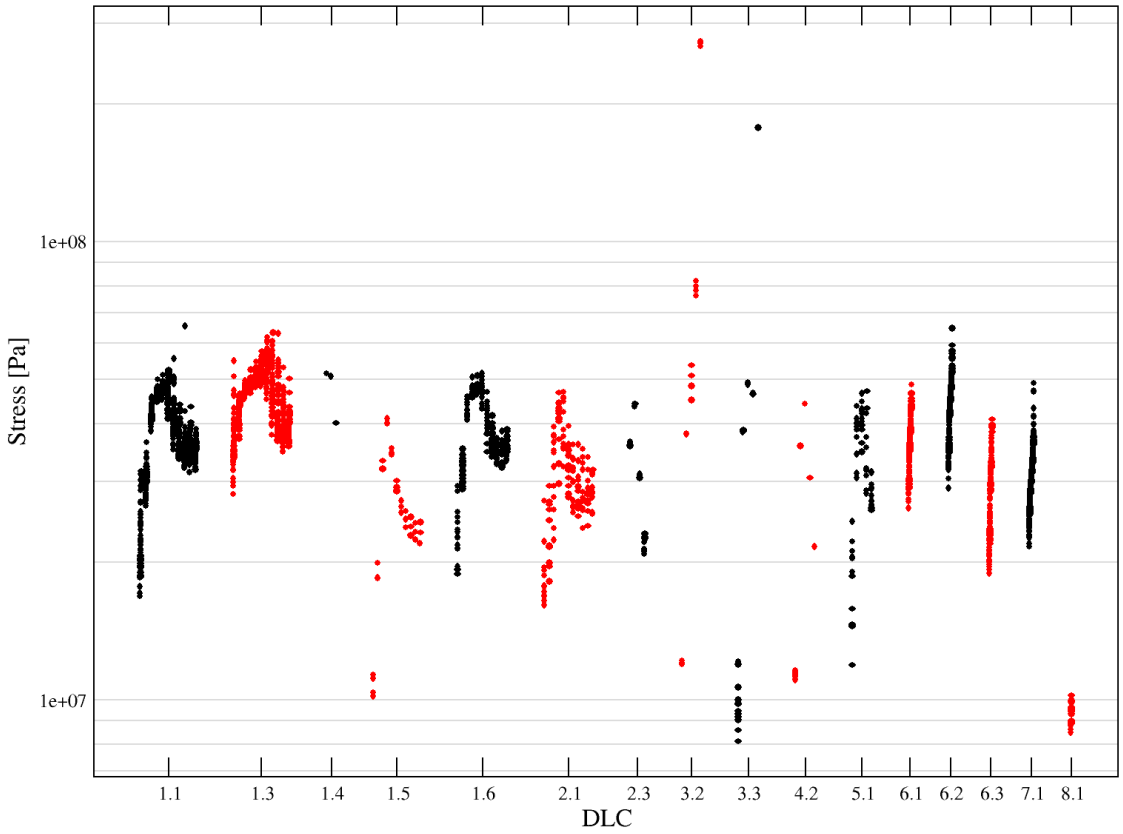

Figure 6.3: Summary of tower stress from the IEC 61400 design load cases.

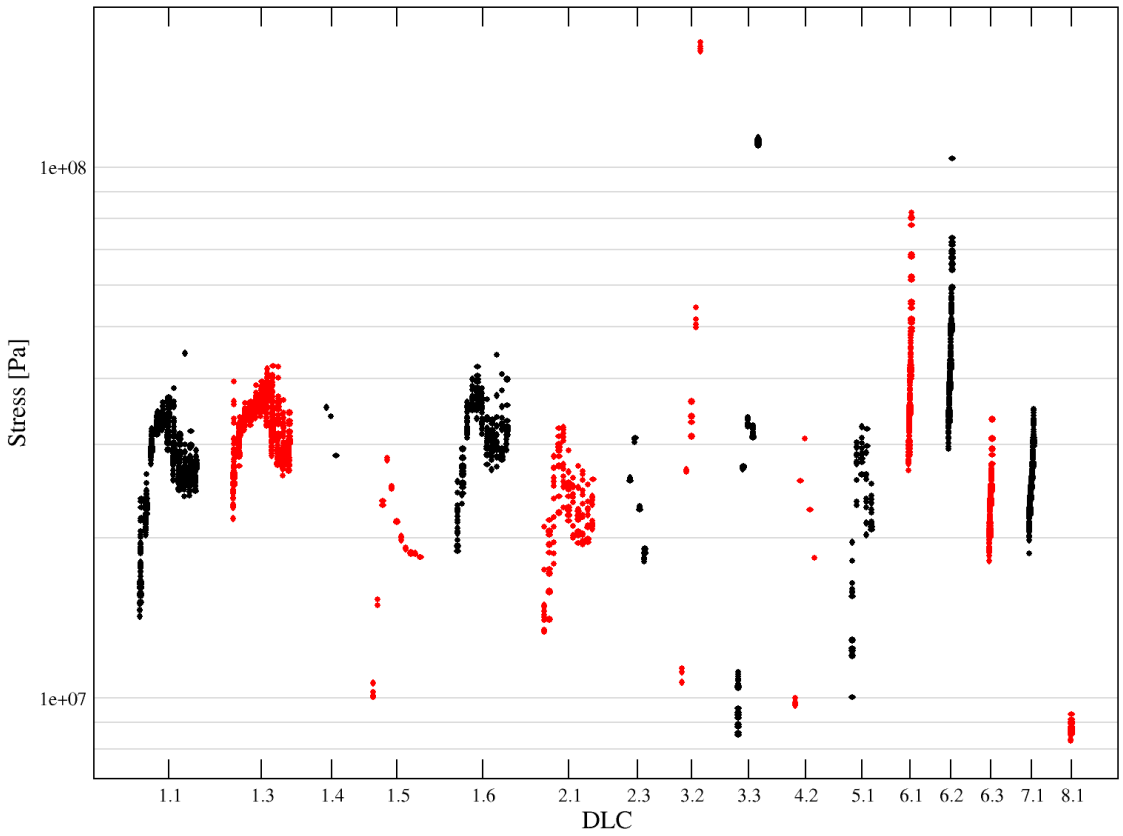

Figure 6.4: Summary of monopile stress from the IEC 61400 design load cases.

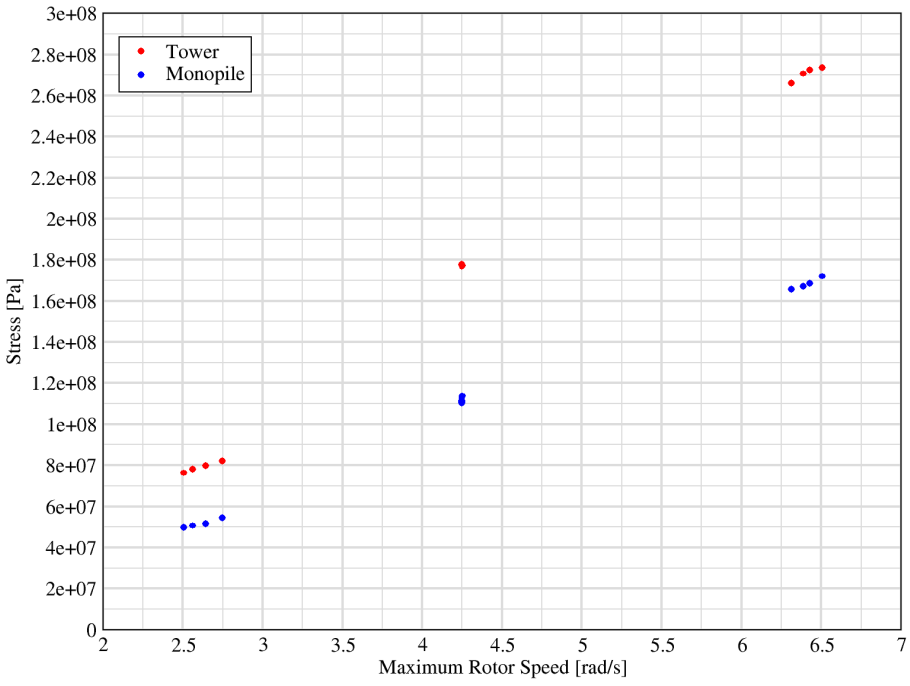

Figure 6.5: Stress vs. max rotor speed in start-up.

assuming the wind turbines are equipped with a power-backup for control and yaw system in case of grid loss IEC (2019a).

Simulations were done with Deeplines Wind^{TM} on the updated case, with the 14.9m water depth that is consistent with the given site data, and limiting the height of the waves with the same breaking wave criterion discussed above. As for the previous case, see Figures 6.3 and 6.3, the largest von Mises stress was obtained on the monopile for DLC 6.1 (see Figure 6.6) which corresponds to a wind turbine in non operating parked (idle) condition. Therefore, only this configuration is considered for the computation of the critical failure probability in this section.

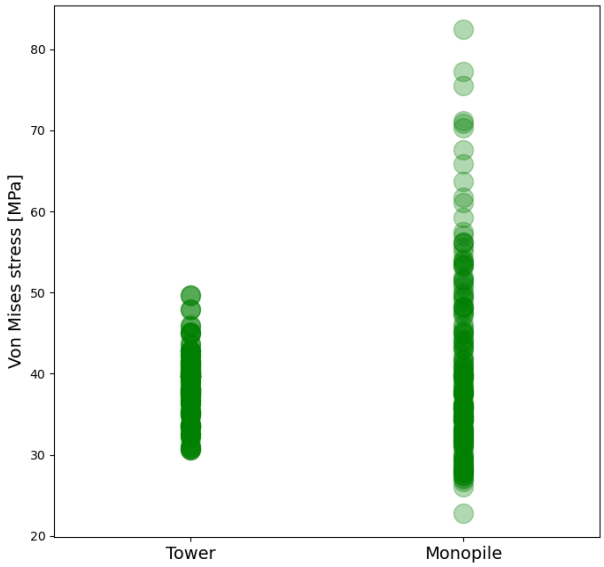

Figure 6.6: Maxima of the von Mises stress at the bottom of the tower and the monopile for the DLC 6.1 with Deeplines Wind^{TM}.

6.3 Evaluation of Initial Design ULS

The sequential sampling method introduced in section 4.1.3 is applied to estimate the failure probability defined in equation (6.1). The configuration of the algorithm as well as the result are described in this section.

6.3.1 Configuration

To estimate the failure probability, the sequential sampling is employed where:

- for the initial DoE a Latin Hypercube Sampling maximin Auffray et al. (2012) of 60 points is used to span the domain of (ξ, ζ);
- at each enrichment step, 60 enrichment points are added to the DoE;
- for each point of the DoE, 20 seeds are considered for the ST sea elevation and wind processes.

6.3.2 Results

Only one enrichment cycle is performed to obtain a sufficiently accurate estimation of the failure probability resulting in 2400 simulations over which 153 crashed. The 2D projections of the resulting Design of Experiments (DoE) is displayed in Figure 6.7.

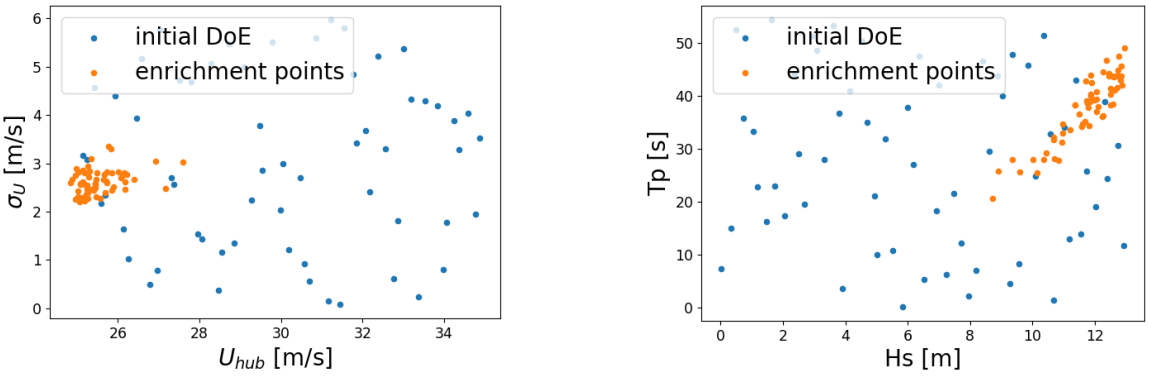

Figure 6.7: 2D projection of the DoE used in the sequential sampling method

The evolution of the annual failure probability and the confidence interval is displayed in Figure 6.8.

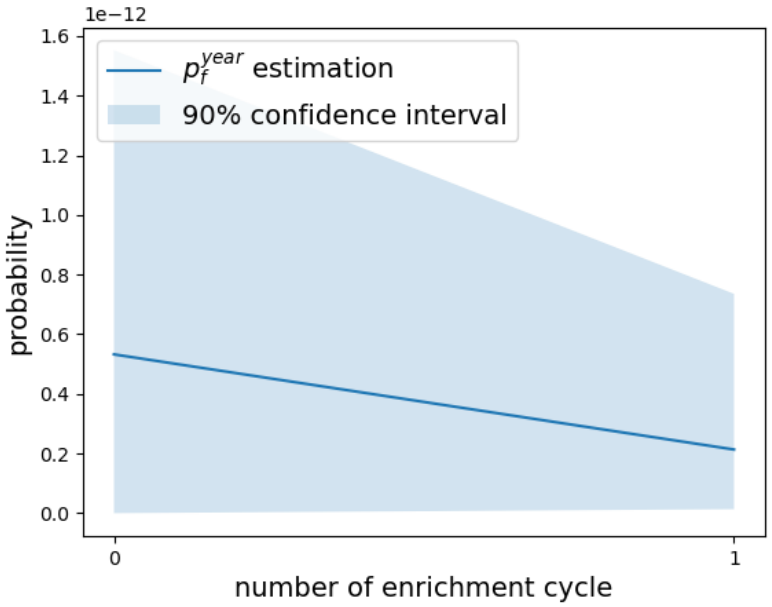

Figure 6.8: Evolution of the annual failure probability estimation with sequential sampling.

The sequential sampling method estimates the annual failure probability at 2.1×10^{-13} with the following 5%-95% confidence interval: $[0.1 \times 10^{-13}, 7.4 \times 10^{-13}]$.

6.4 Optimization of design

6.4.1 Presentation of the problem

From the analysis described in the previous section, it appears that the nominal design of the considered Teesside turbine is conservative. In this section, the purpose is to reduce the mass of the structure which reduces its manufacturing cost while ensuring several constraints. To ensure manufacturability and weldability, the diameter to thickness ratio is contrained to stay the same that in the initial design. The annual critical ULS failure probability must stay below 10^{-4} after requirements of IEC (2019b); DNVGL (2018). The natural frequencies of the tower must be at more than 15 % distance from the 3P rotor frequency to prevent from resonance. Finally two buckling criteria are checked, a beam buckling Lloyd (2005) and a shell buckling Eurocode (1993), like in the WISDEM optimisation software of NREL NREL (2024); Dykes et al. (2014).

6.4.2 Design transformation

Since the thickness of the structure is the main driver of the total mass of the structure, we consider it as the only design variable. To reduce the thickness, we propose to proceed as follows. Let's denote $t_1(n_i)$ and $D_1(n_i)$ respectively the nominal thickness and diameter at at node n_i of the structure. Let's consider α a multiplicative coefficient, $t_\alpha(n_i)$ and $D_\alpha(n_i)$ the thickness and diameter of the new design at node n_i considering α. To obtain these quantities, we proceed as follows:

- if node n_i is a node of the monopile or of the transition piece: $t_\alpha(n_i) = \alpha \times t_1(n_i)$ and $D_\alpha(n_i) = \alpha \times D_1(n_i)$;
- if node n_i is on the tower: $t_\alpha(n_i) = c_\alpha(n_i) \times t_1(n_i)$ and $D_\alpha(n_i) = c_\alpha \times D_1(n_i)$ where:
  - $c_\alpha(n_i) = \alpha$ at the bottom of the tower;
  - $c_\alpha(n_i)$ varies from α to 1 along the tower;
  - $c_\alpha(n_i) = 1$ at the top of the tower.

Doing so, we can reduce the thickness of the structure while ensuring both that the diameter/thickness ratio and the diameter of the tower top are conserved.

6.4.3 Mathematical formulation

The optimization problem we solve in this section writes:

$$\begin{aligned} \text{minimize} \quad & \alpha \\ \text{subject to :} \quad & p_f^{year}(\alpha) < 10^{-4} \\ & f(\alpha) > 1.15 \times f_{3P} \\ & c_b(\alpha) < 1 \end{aligned} \tag{6.2}$$

where $p_f^{year}(\alpha)$, $f(\alpha)$, $c_b(\alpha)$ are respectively the critical annual ULS failure probability, the smallest natural frequency of the tower and the buckling criterion considering the transformation of the design using the coefficient α as described in section 6.4.2. Finally f_{3P} is 3 times the frequency of the rotor.

Notice that the buckling criterion depends on the loads applied to the structure and thus for a complete probabilistic formulation of the constraints, this criterion should consider all

the sources of uncertainties. To simplify the problem, this criterion is checked only for DLC 6.1.

The main difficulty to solve problem (6.2) is that at each iteration of the optimization solver, we need to estimate $p_f^{year}(\alpha)$ which requires to use the sequential sampling method and thus to perform a prohibitive number of simulations. To overcome this difficulty, we propose a new approach which solves problem (6.2) using the simulations obtained from the estimation of the failure probability of the initial design (cf section 6.3) and thus requiring no additional simulation.

This approach is introduced in the next section.

6.4.4 Conservation of the moments and forces with design transformation

To solve problem (6.2), we use the fact that, for this case study and a given external excitation (wind and waves), quantities such as the bending moments and shear forces, throughout the structure, are preserved across a relatively wide range of diameter and thickness. A physical reasoning supporting this observation could be that these quantities are kept constant with (small) changes in the design, similarly to the forces within a simple spring remains constant, even for different springs (what counts is the external loading). In Figure 6.9, we compare the time series of bending moment at the bottom of the tower and at the mudline considering the nominal design, a modified design with a reduction of 25% of the thickness and another design with a reduction of 10% of the diameter. The results are displayed for two realizations of the LT and ST uncertainties (i.e. considering two different loads on the structure). We see that the time series of bending moment are not sensitive to the modification of the thickness and diameter of the structure.

The stress, on the other hand, depends explicitly on the geometry of the structure. For a given external excitation, the relation between the time series of axial stress (σ_z), the bending moment (M) and the tension (T) at some location of the structure is given by:

$$\sigma_z(D_\alpha, t_\alpha) = M\frac{D_\alpha}{2I(D_\alpha, t_\alpha)} + T\frac{1}{A(D_\alpha, t_\alpha)} \tag{6.3}$$

where the moment of inertia $I(D_\alpha, t_\alpha)$ and the area $A(D_\alpha, t_\alpha)$ depend on the local external diameter D_α and thickness t_α at the considered location as:

$$I(D, t_\alpha) = \frac{\pi}{64}(D_\alpha^4 - (D_\alpha - 2t_\alpha)^4), \quad A(D_\alpha, t_\alpha) = \frac{\pi}{4}(D_\alpha^2 - (D_\alpha - 2t_\alpha)^2). \tag{6.4}$$

Using this observation, it is possible to estimate $p_f^{year}(\alpha)$ (the failure probability considering a modified design) using the 2400 simulations done on the nominal design that were carried out to estimate p_f^{year} (cf section 6.3). Indeed, for these simulations, the time series of moments and tension are known. From the observation above, they are the same that for a modified design. The stresses for the new design can thus be obtained with equation (6.3) using the nominal moments and forces and the modified diameter and thickness. This results in a new DoE. The estimation of the new failure probability $p_f^{year}(\alpha)$ is then done using the kriging approach of section 4.1.3 without the enrichment step. This optimization approach is summarized in Figure 6.10.

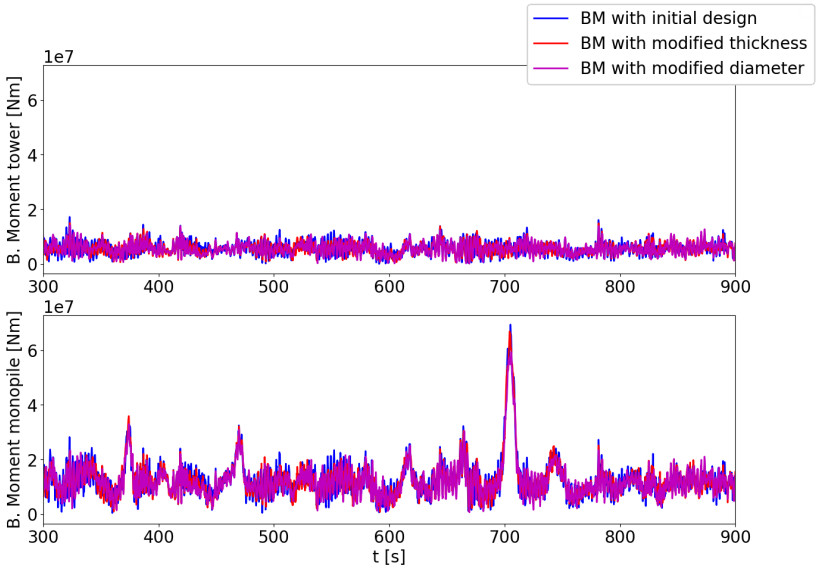

(a) Time series of the bending moment for tower base (top) and monopile at mudline (bottom) with $U = 35$m/s, $TI = 11\%$, $\zeta = 0^o$, $\beta = 0^o$, H_s=13m, T_p=43s.

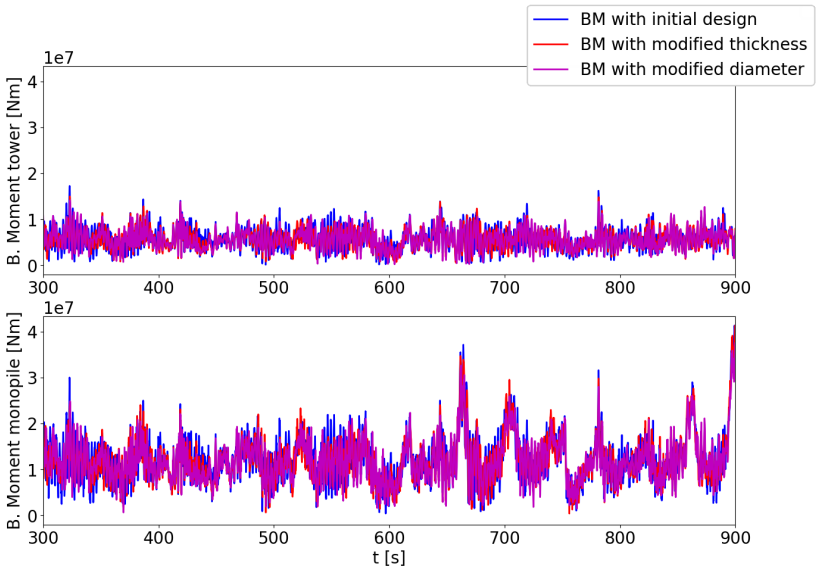

(b) Time series of the bending moment for tower base (top) and monopile at mudline (bottom) with $U = 35$m/s, $TI = 11\%$, $\zeta = 30^o$, $\beta = 30^o$, H_s=13m, T_p=43s.

Figure 6.9: Time series of bending moments with diameter and thickness reduction

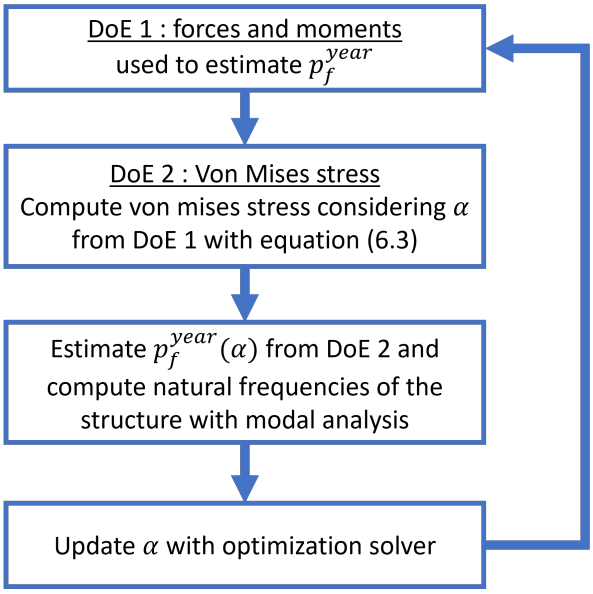

Figure 6.10: Flowchart of the RBDO approach.

6.4.5 Optimization approach

To account for the approximation introduced by the method described in section 6.4.4 to estimate $p_f^{year}(\alpha)$, the threshold of the annual failure probability for the first constraint in problem (6.2) is lowered to 10^{-5}. The 3P resonance is checked during the optimization by means of a fast to compute modal analysis.

Moreover, the buckling constraint is only checked at the end of the optimization process for the optimal solution to speed up the resolution. It becomes feasible to solve problem (6.2) without dynamic simulation. This results in a 1D optimization problem that we solve with the COBYLA solver (Powell (1994)).

6.4.6 Optimization result and verification

The result of the optimization is the new design displayed in Figure 6.11. In this figure, the horizontal lines indicate the separation between the monopile, the transition piece and the tower. The diameter of the initial design is indicated in blue lines while the red lines represent the new design. The thickness of the structure is the distance between the lines and the dotted lines (the thickness is multiplied by a factor 3 on the figure to distinguish it).

This new design leads to a mass reduction of 21 % of the structure, where the limiting criterion of the optimization is the resonance of the structure. The details of the mass reduction for each part of the structure is given in Table 6.1. The failure probability at the optimum is estimated at 2.2×10^{-9} with the approach described in section 6.4.4. We verify this probability with the sequential sampling method on the simulator using the new design and it gives a failure probability at 0.7×10^{-9} with a 90% confidence interval $[5.4^{-11}, 2.2^{-9}]$.

To speed up the process, the buckle criterion was not integrated to the optimization but is verified only for the optimal design on DLC 6.1. The results are shown in Figure 6.12 where we plot the utilization for each point of the tower of the optimal design. We see that they are far from the unity utilization which means a safe design in term of buckling,

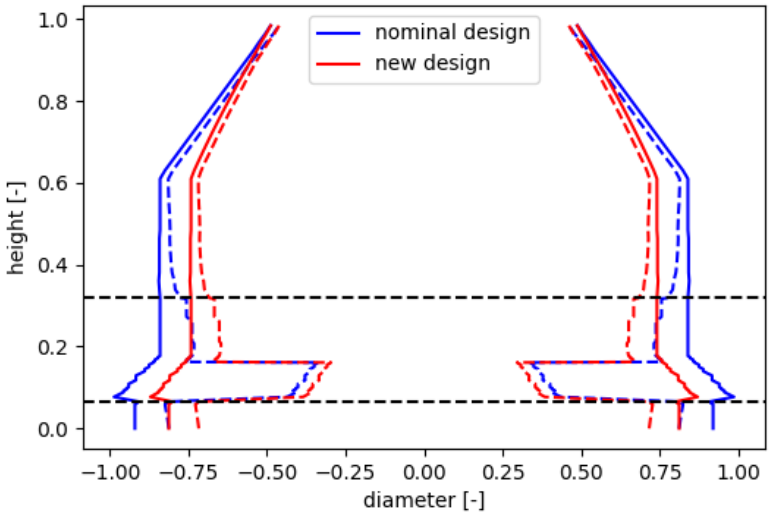

Figure 6.11: Profiles of the nominal design and the new design (with normalized axes).

Part of the structure	mass (initial design) [tons]	mass (new design) [tons]
Monopile	71.62	55.76
MP+TP	226.52	176.34
Transition piece	139.62	108.69
Tower	139.31	114.10
Total	577.08	454.89

Table 6.1: Mass reduction for each part of the structure.

even considering a safety factor of 1.45.

6.5 Conclusions of the Teesside study

In this section, ULS was considered for both tower basis and monopile mudline plasticity. The critical ULS for the Teesside case was identified from simulations of IEC 61400 Design Load Basis to be found for von Mises stresses on monopile at mudline during DLC6.1 (parked idle configuration).

The sequential sampling method described in section 4.1.3 is then applied with success to estimate the critical ULS failure probability with accuracy. This analysis confirms that the nominal design is conservative which is mainly due to the fact that at the time of the design, site specific conditions given by Kelly and Vanem (2022) were not available, hence generic aerodynamic loads of turbine class were used.

To reduce the cost of the structure, a new optimization approach is introduced that aims to reduce its mass with relatively few simulations while ensuring constraints on the manufacturability, the critical reliable ULS, beam and shell buckling and 3P tower resonance. As discussed in section 2, considering a reliable constraint in a design optimization of OWT is highly challenging due to the computational cost of the failure probability evaluation. The

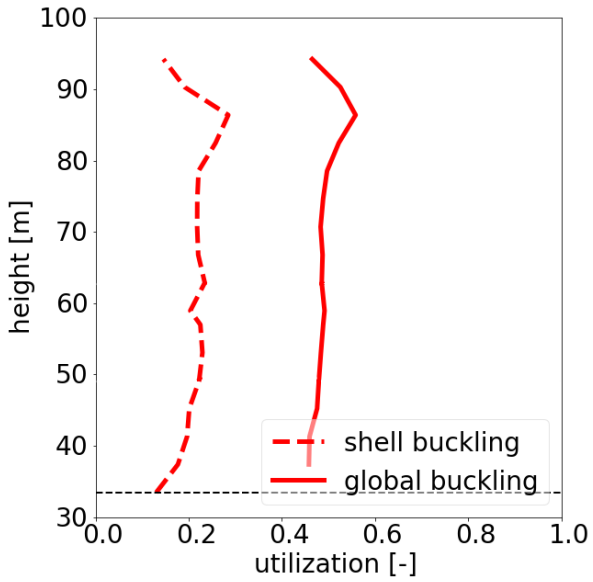

Figure 6.12: Buckling utilization on the optimal design for both the shell and global criteria from the DLC 6.1 (critical one) data.

new procedure proposed here for this monopile case study takes advantage of a relative unchange of the bending moment of the tower when reducing the thickness. The thickness change then only modifies the analytical relation between the bending moment and the von Mises stress at the tower and monopile bottom, enabling an easy update of the failure probability computation with the sequential sampling approach.

This results in a reduction of about four order of magnitude of the reliable ULS failure probability, and 21% mass reduction of the structure, the limiting constraint for the design being actually that of the 3P resonance.

It may be noticed that the failure probability that was considered during this optimization was considering the most critical load case only. When estimating the failure probability, one may actually prefer to compute a more representative estimate which includes both operational and parked configurations each of them being weighted by the expected probability of occurrence. Such computation will be adopted in section 8.3 for the Teesside case, see equation 8.6, the configuration occurrence being determined from the distribution of the mean wind speed. As can be seen in this section, the resulting annual failure probability would actually be smaller, as the parked configuration occurrence is less than that of the operational configuration. We can thus consider our current choice to be conservative for our example. Let us also emphasize that this choice has no consequence on the optimization results, as the limiting criterion is actually the resonance one.

7 Application to South Brittany case study

The exercise presented in the previous section for the Teesside case is repeated for a floating offshore wind turbine located at the South Brittany site. The structure is based on the IEA 15-MW NREL turbine (NREL (2020)) on the UMaine semi-submersible floater (Allen et al. (2020)) which has been modified (tower and mooring) to be adapted to the South Brittany conditions, see details in Peyrard et al. (2022); Capaldo et al. (2021) and a view of the Deeplines Wind^{TM} implementation of this case in Figure 7.1.

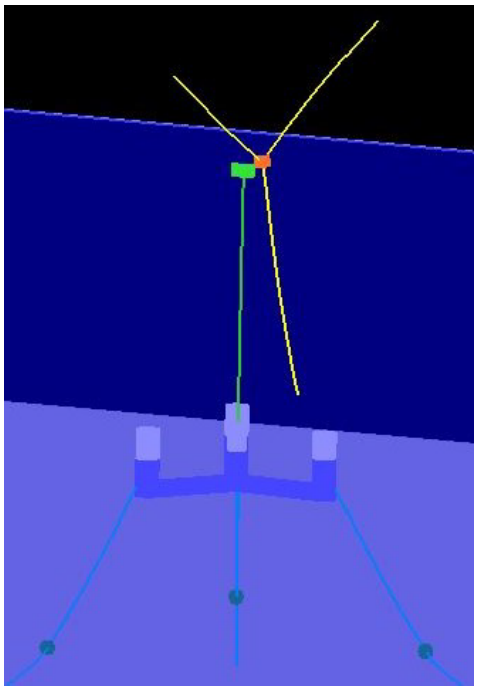

Figure 7.1: 3D view of the IEA15MW on UMaine semi-submersible floater adapted to South Brittany site in HIPERWIND, after Vanem et al. (2023).

7.1 Case study presentation

7.1.1 Failure probability

The failure probability for the South Brittany case has the same definition as for the Teesside case (cf equation (6.1)) except for the following elements:

- ΔT is equal to 1 hour;
- we do not consider uncertainties on a model parameter (so there is no variable ζ);
- ξ is a 4D random vector composed of the following random variables:
  - U_{hub}: the mean wind speed at hub height;
  - σ_{hub}: the temporal standard deviation of the wind speed at hub height;
  - H_s: the significant waveheight;
  - T_p: the peak period;

  The choice to reduce the dimension of the inputs is done to simplify the estimation

of p_f. The variables considered are those to which the quantity of interest s is most sensitive.

- s is the von Mises stress at the tower bottom and in parked condition. Due to time constraints, it was not possible to carry out a complete design load base (DLB) for South Brittany. Based on the Teesside DLB, we assume the same critical DLC for this case.
- ρ is the yield strength of the tower material.

7.1.2 Distribution of the uncertainties

The distribution of the LT parameters for South Brittany is detailed in Vanem et al. (2023). The marginal distribution of U_{hub} is truncated below 25m/s since the turbine is in parked condition.

For the random variable ρ, the material of tower is the steel S355NL and the thickness at the bottom implies the same distribution that for the Teesside case: a lognormal normal distribution with mean 315 MPa and coefficient of variation 0.1.

7.2 Evaluation of Initial Design ULS

The sequential sampling is now applied to South Brittany case described in section 7.1. For the algorithm, the same configuration as for the Teesside is used here.

Three enrichment steps are necessary to obtain a sufficiently accurate estimation of p_f^{year} resulting in 3250 simulations. The 2D projections of the resulting DoE is displayed in Figure 7.2.

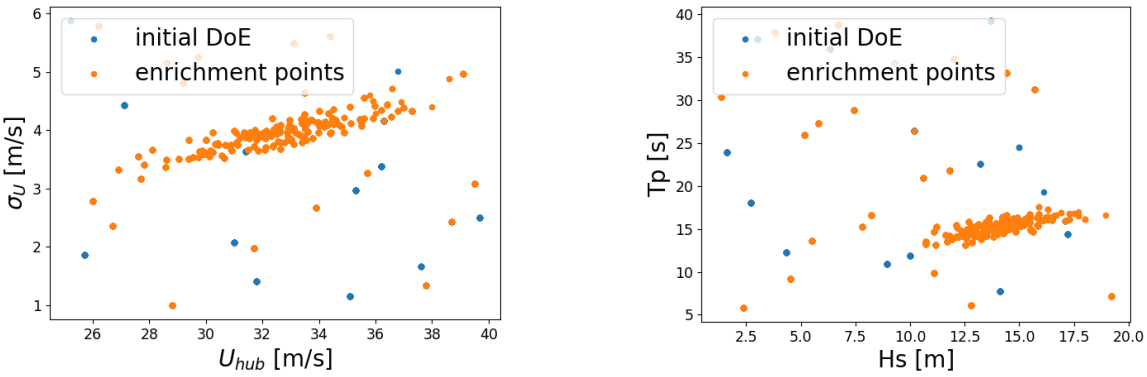

Figure 7.2: 2D projection of the DoE used in the sequential sampling method.

The evolution of the annual failure probability and the confidence interval is displayed in Figure 7.3.

The sequential sampling method estimates the annual failure probability at 3.7×10^{-5} with the following 90% confidence interval: $[2.2 \times 10^{-5}, 5.8 \times 10^{-5}]$.

7.3 Discussions on Design Optimization

As seen in section 7.2, the critical ULS failure probability is at 3.7×10^{-5} which is already close to the threshold 10^{-4}. Consequently, it has been decided to not optimize the design.

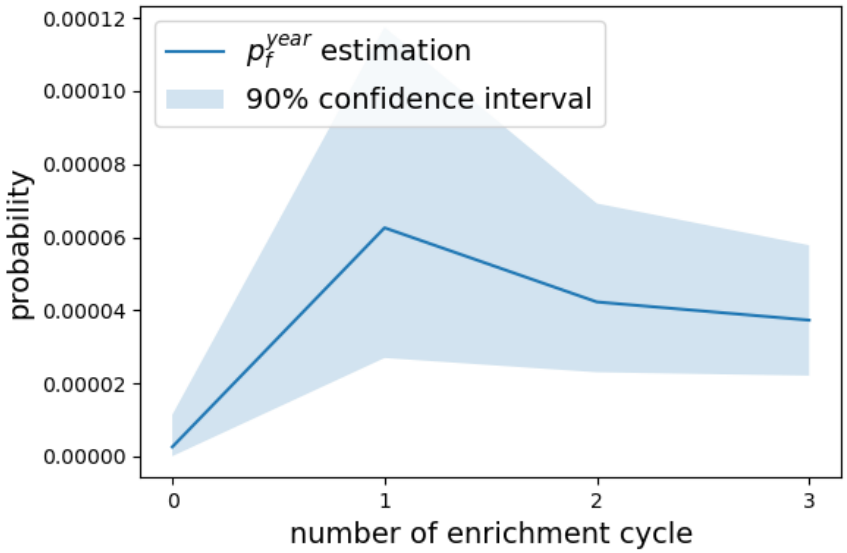

Figure 7.3: Evolution of the annual failure probability estimation with sequential sampling.

On top of the ULS failure probability, we check that the tension of the mooring line is always positive for the DLC6.1 to avoid out-of-plan bending of the line, which would cause the material to break under subsequent tensions. The minimum tension over the three mooring lines for the DLC6.1 is at 8×10^5 Newton.

For what concern buckling check, we refer to Capaldo et al. (2021) which indicates that the diameter to thickness ratio should prevent it. Indeed the two criteria used for Teesside design do not take into account the accommodation of the aerodynamic thrust by the floater motion. A detailed check would require a Finite Element analysis with the equivalent stiffness of the floater and its mooring line at the tower basis, which was not possible for lack of time.

The natural frequencies of the tower are also checked with a modal analysis. The frequencies of the fore-aft and side-side modes are respectively at 0.456 Hz and 0.461 Hz which is sufficiently far from the 3P of 0.378Hz to avoid resonance.

Besides, if the nominal design was conservative, the optimization approach used for the Teesside case would not be possible here. Indeed, the method is based on the observation detailed in section 6.4.4 that the time series of bending moment and forces are not sensitive to a reduction of the thickness and diameter of the structure. For the floating case, this observation does not stand. In Figure 7.4, we compare the bending moment of the nominal and a modified design with a tower thickness and diameter reduced by 10% for two loads and we see that the time series are clearly different. In the modified design, the mass of the floater was also changed (assuming a change in the hydrodynamic ballast only) to avoid recomputation of the hydrodynamic properties. The floater draft in hydrostatic is thus the same that for the initial design. Also, to simplify the understanding, the center of gravity of the floater was modified in order to preserve the total center of gravity of the structure. This simplification may be replaced by a more physical design change, with explicit location of the ballast.

The difference of bending moment illustrated in Figure 7.4 can be explained by the change in the inertia contribution of the balance of momentum equation due to the mass

distribution change between the RNA and turbine on one side and the floater with mooring lines on the other side. This also causes differences in the floater motion, mainly in surge component, which modifies the mooring lines tension distribution, see section 7.5.

Therefore, for a floating wind turbine optimization design, other approaches would need to be considered such as a metamodel-based method considering the design parameters as input of the metamodel.

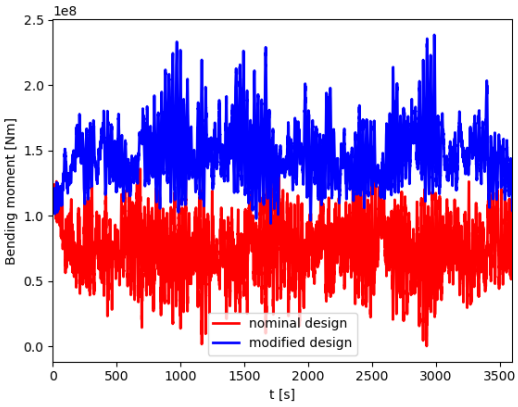

(a) $U = 27.1$m/s, $TI = 12.42\%$, $\zeta = -0.02^o$, H_s=1.36m, T_p=13.61s, $\theta_{wind} = 79.34^o$, $\theta_{wave} = 225.4^o$.

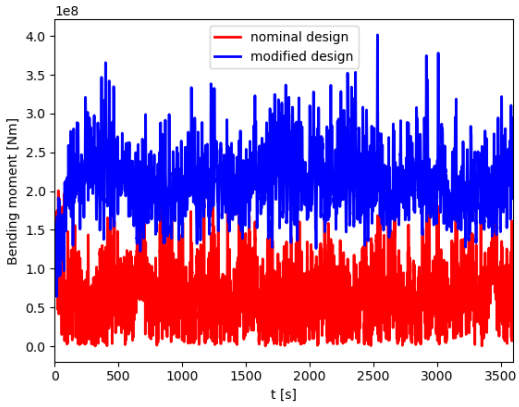

(b) $U = 37.14$m/s, $TI = 9.09\%$, $\zeta = -0.02^o$, $\beta = 30^o$, H_s=7.17m, T_p=13.61s, $\theta_{wind} = 79.34^o$, $\theta_{wave} = 225.4^o$.

Figure 7.4: Comparison of the tower base bending moment time series with nominal and modified designs.

7.4 Conclusions of the South Brittany study

The failure probability has been estimated with the DNV's sequential sampling method. It appears that the critical annual ULS failure probability is close to the threshold of 10^{-4} thus no optimization of the design was performed for this case. Let us however remind, like in the conclusions of the Teesside study, that we could alternately have chosen to compute a more representative annual failure probability considering both parked and operational configuration each of them being weighted by their probability of occurrence. If the parked configuration was actually providing higher loads, the resulting failure probability would then have been smaller, which would have allowed for possible optimisation.

Moreover, it was noticed that contrarily to the Teesside case study, the bending moment time series is significantly changing when modifying the tower thickness for this floating case which may be explained by the change of inertia contribution in the balance of momentum equation of the overall structure. Consequently, the optimization method introduced for the Teesside case could not be applied here and a new method would need to be developed to optimize the design of the structure without a prohibitive number of simulation. This would for instance require to define meta-model of ULS vs tower thickness.

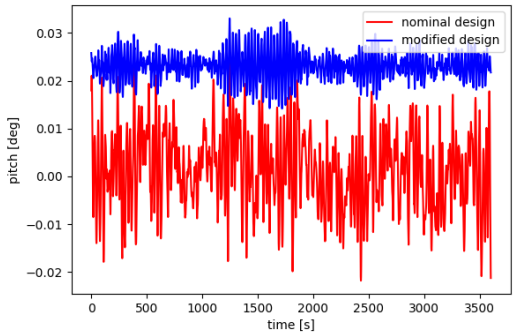

(a) Pitch with LT parameters of the left picture of 7.4.

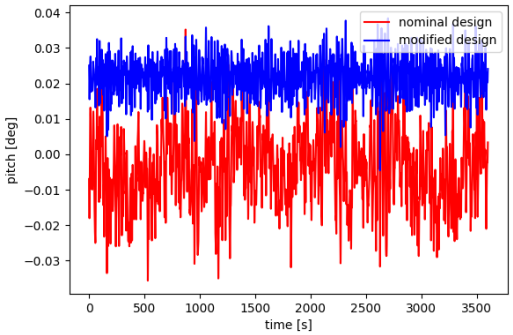

(b) Pitch with LT parameters of the right picture of 7.4.

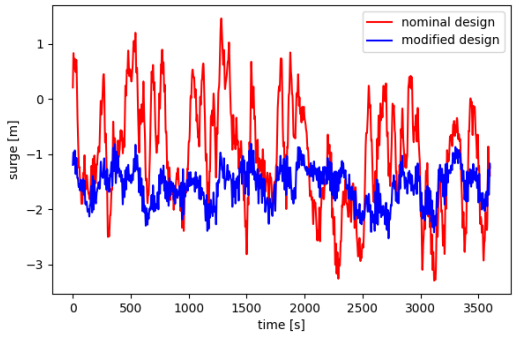

(c) Surge with LT parameters of the left picture of 7.4.

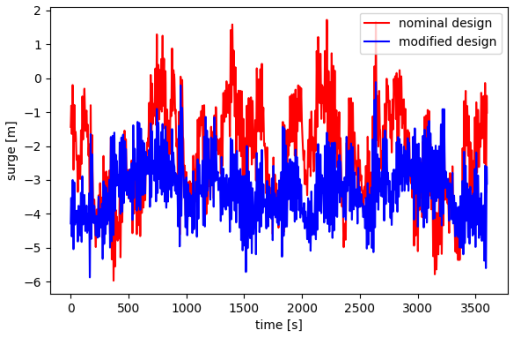

(d) Surge with LT parameters of the right picture of 7.4.

Figure 7.5: Comparison of pitch and surge time series with nominal and modified designs

8 Robustness of the failure probability to the environmental parameter distribution

8.1 Problem statement

The failure probability estimation carried on in Section 6.1, relies on the probability distributions estimated in Kelly and Vanem (2022) and Vanem et al. (2023). Because the latter are determined on the basis of a finite dataset of LT parameters recorded over the span of four years at the Teesside site, we expect them to be affected by epistemic uncertainty following the fitting procedure.

In this section, we aim to perform a robustness/sensitivity analysis of the estimated ULS probability of failure P_f, due to the uncertainty in the joint distribution of the vector of environmental parameters $\xi \sim f_\xi(\xi)$. In other words, we see the estimated failure probability as a random variable with unknown probability distribution, that we want to quantitatively characterize.

8.1.1 Notation

As the topic requires a hefty amount of bookkeeping and different concepts, we introduce here for reference the notation that will be used throughout this analysis.

- $\boldsymbol{X} = \{\xi, \zeta\}$, random vector comprising both the environmental random parameters ξ, and the structural uncertain parameters ζ (see Section 6.1.1).
- $f_{\boldsymbol{X}}(\boldsymbol{x}) = f_\xi(\xi) f_\zeta(\zeta)$ - Reference joint distribution of the random vector $\boldsymbol{X}$ of uncertain parameters. $f_\xi(\xi)$ is the reference distribution calculated in Kelly and Vanem (2022), while $f_\zeta(\zeta)$ is given in Section 6.1.1.
- $\boldsymbol{\theta}$ vector of hyperparameters of the joint distribution $f_\xi(\xi)$. Depending on the parameterization of the latter, they can contain the parameters and types of the marginal distributions ξ_i, those of the conditional distributions $\xi_{i|\xi_j}$, any copulas, etc. When needed in the text, we may also write the joint distribution of environmental parameters with an explicit dependence on the hyperparameters $\boldsymbol{\theta}$, as $f_{\xi|\boldsymbol{\theta}}(\xi, \boldsymbol{\theta})$.
- $\widehat{\boldsymbol{\theta}}$ - reference set of hyperparameters fitted in Kelly and Vanem (2022). It follows that the reference joint distribution of environmental parameters is $f_\xi(\xi) = f_{\xi|\boldsymbol{\theta}}(\xi, \widehat{\boldsymbol{\theta}})$.
- $f_{\boldsymbol{X}|\boldsymbol{\theta}}(\boldsymbol{x}, \boldsymbol{\theta}) = f_{\xi|\boldsymbol{\theta}}(\xi, \widehat{\boldsymbol{\theta}}) f_\zeta(\zeta)$ - joint distribution of the LT uncertainty parameters $\boldsymbol{X}$, with the explicit dependence on the distribution on a given set of hyperparameters $\boldsymbol{\theta}$.
- ω - Latent variable representing the underlying state of randomness of the system, often colloquially referred to as *random seed*. This is what causes failure within a given set of parameters $\boldsymbol{x}$
- $y(\boldsymbol{x}, \omega)$ - Response quantity of interest (QoI) related to the limit-state under investigation, e.g. von Mises stress at the tower base. For a given set of LT parameters $\boldsymbol{x}^*$ and a single random seed $\widehat{\omega}$, this is a deterministic scalar value.
- ρ - Critical maximum threshold related to the QoI $y(\boldsymbol{x}, \omega)$. The system fails if $y(\cdot) > \rho$. For the sake of notation simplicity, we will omit explicit dependencies of ρ in conditional expressions.
- $P_{f|\boldsymbol{x}}(\boldsymbol{x})$ - Conditional probability of failure given a single realization of $\boldsymbol{X}$. It is

defined as:

$$P_{f|\boldsymbol{x}}(\boldsymbol{x}) = P_{\omega}(y(\boldsymbol{x},\omega) \geq \rho) \tag{8.1}$$

- $P_{f|\boldsymbol{\theta}}(\boldsymbol{\theta})$ - Conditional failure probability for a given set of hyperparameters $\boldsymbol{\theta}$:

$$P_{f|\boldsymbol{\theta}}(\boldsymbol{\theta}) = \mathbb{E}_{\boldsymbol{X}}\left[P_{f|\boldsymbol{x}}(\boldsymbol{x})\right] = \int_{\Omega_{\boldsymbol{X}}} P_{f|\boldsymbol{x}}(\boldsymbol{x}) f_{\boldsymbol{X}|\boldsymbol{\theta}}(\boldsymbol{x},\boldsymbol{\theta}) d\boldsymbol{x} \tag{8.2}$$

- P_f - Reference probability of failure, corresponding to $P_f = P_{f|\boldsymbol{\theta}}(\widehat{\boldsymbol{\theta}})$

8.1.2 Research question

Because the reference set of joint distribution parameters $\widehat{\boldsymbol{\theta}}$ in Teesside is estimated from a finite dataset, it is expected to be uncertain. In other words, as is common in estimation theory, each set of estimated parameters $\boldsymbol{\theta}$ can be seen as a realization of an underlying random variable $\boldsymbol{\Theta}$, with unknown joint probability distribution $f_{\boldsymbol{\Theta}}(\boldsymbol{\theta})$. It is therefore important to propagate such uncertainty to the estimated P_f, by providing a statistical characterization of the distribution of $f_{P_{f|\boldsymbol{\theta}}}(P_{f|\boldsymbol{\theta}})$ (e.g. moments, confidence bounds, etc.).

This is a well posed problem, that can be seen as a classical forward uncertainty propagation problem, using as a computational model Eq. (8.2), and as input the random vector of hyperparameters $\boldsymbol{\Theta}$.

8.2 Methodology/Implementation

There are two steps involved in the uncertain propagation of $\boldsymbol{\Theta}$ to P_f:

1. Estimation of the parametric uncertainty on $\boldsymbol{\Theta}$, and
2. Propagation of the parametric uncertainty to $P_{f|\boldsymbol{\theta}}(\boldsymbol{\theta})$.

The entire estimation process is performed directly by bootstrapping (Efron, 1979), the estimator $P_{f|\boldsymbol{\theta}}(\boldsymbol{\theta})$ on the original Teesside dataset used in Kelly and Vanem (2022).

8.3 Step I: uncertainty estimation

We can observe from Eq. (8.2) that the value of $P_{f|\boldsymbol{\theta}}(\boldsymbol{\theta})$ is uniquely determined by the set of environmental hyperparameters θ. Therefore, estimating the uncertainty of P_f via MC simulation simply means generating a set of N realizations $\{\boldsymbol{\theta}^{(1)}, \cdots, \boldsymbol{\theta}^{N}\}$ that is consistent with the available data.

To achieve this, the raw Teesside dataset from Kelly and Vanem (2022), consisting of approximately $200,000$ SCADA measurements of the five parameters in ξ, is first resampled with replication through bootstrapping (Efron, 1979) a total of N times. Each replication is subsequently fitted with a general mixed parametric and non-parametric joint distribution based on the vine copula framework from Aas et al. (2009); Torre et al. (2019).

The inference algorithm has the following characteristics:

- Due to the relatively large size of the experimental design, all marginal distributions are constructed non-parametrically through unbounded, Gaussian Kernel density estimation.

- The dependence structure is determined through a fully automated vine-copula inference procedure (Torre et al., 2022), with the following candidate models:
  - C- and D- vines
  - free pair-copula ordering and structure
  - Available pair-copula families: *Student-t, Gaussian, Clayton, Gumbel, Frank, Independent*, including all allowed rotations.
  - Selection criterion: Akaike information criterion (Akaike, 1973).

All calculations are performed with the statistical inference module of the general purpose uncertainty quantification software UQLab (Marelli and Sudret, 2014; Torre et al., 2022).

Each run of the fitting process results in a set of hyperparameters $\boldsymbol{\theta}^{(i)}$, which we can then use to evaluate two quantities that will be of interest in the next section: the joint distribution $f_{\boldsymbol{X}}^{(i)}(\boldsymbol{x}) \overset{\text{def}}{=} f_{\boldsymbol{X}}(\boldsymbol{x}, \boldsymbol{\theta}^{(i)})$, and the corresponding probability of failure $P_f^{(i)} \overset{\text{def}}{=} P_{f|\boldsymbol{\theta}}(\boldsymbol{\theta}^{(i)})$.

8.4 Step II: Propagation to the failure probability estimate

Calculating $P_f(i)$ can be a computationally challenging process, and one that has already been performed to calculate the reference results in Section 6.3.
A more efficient approach is therefore sought after, that can take advantage of the existing calculations.

We therefore propose to use an approach that is derived directly from the *importance sampling* literature (Melchers, 1989).

The estimation of $P_{f|\theta}$ from Eq. (8.2) consists of the following steps:

- A sample of uncertain parameters $\mathcal{X} = \left\{\boldsymbol{x}^{(i)}, \quad k = 1, ..., N_{\boldsymbol{x}}\right\}$ is drawn from the reference distribution $f_{\boldsymbol{X}}(\boldsymbol{x})$), with $N_{\boldsymbol{x}} \sim \mathcal{O}(10^4)$.
- For each set of LT and structural parameters $\boldsymbol{x}^{(i)}$, multiple simulations with different random seeds ω are solved with an aero-servo-elastic simulator (e.g. Deeplines Wind^{TM} or HAWC2). The resulting set of QoIs are then processed through an adaptive Kriging-based probability estimation method, resulting in a set of conditional failure probabilities, $\mathcal{P}_f = \left\{P_{f|\boldsymbol{x}}(\boldsymbol{x}^{(i)}), i = 1, \cdots, N_{\boldsymbol{x}}\right\}$.
- The integral in Eq. (8.2) is then simply estimated by averaging the conditional $P_{f|\boldsymbol{x}}(\boldsymbol{x})$'s over the sample:

$$P_{f|\boldsymbol{\theta}}(\boldsymbol{\theta}) \approx \frac{1}{N_{\boldsymbol{x}}} \sum_{i=1}^{N_{\boldsymbol{x}}} P_{f|\boldsymbol{x}}(\boldsymbol{x}^{(i)}) \tag{8.3}$$

Even though the calculation of each $P_{f|\boldsymbol{x}}(\boldsymbol{x}^{(i)})$ has a limited computational cost, thanks to the use of the Kriging surrogate model, the large number of evaluations needed to obtain accurate results still makes this computation expensive. For the purposes of calculating confidence bounds on the overall P_f, the entire process would need to be repeated for each of the $\mathcal{O}(10^2)$ bootstrap replications of $\boldsymbol{\theta}^{(i)}$.

Thankfully, computational costs can be significantly reduced by simply reweighting the elements of $\mathcal{P}_f$ with importance sampling, and directly approximating the expected value

in Eq. (8.3), rather than repeating a different sampling for each $\boldsymbol{\theta}^{(i)}$.

Starting from the integral in Eq. (8.2), which depends on $\boldsymbol{\theta}$ only by the joint PDF $f_{\boldsymbol{X}|\boldsymbol{\theta}}(\boldsymbol{x}, \boldsymbol{\theta})$, we can write:

$$P_{f|\boldsymbol{\theta}}(\boldsymbol{\theta}) = \int_{\Omega_{\boldsymbol{X}}} P_{f|\boldsymbol{x}}(\boldsymbol{x}) f_{\boldsymbol{X}|\boldsymbol{\theta}}(\boldsymbol{x}, \boldsymbol{\theta}) d\boldsymbol{x} = \int_{\Omega_{\boldsymbol{X}}} P_{f|\boldsymbol{x}}(\boldsymbol{x}) \frac{f_{\boldsymbol{X}|\boldsymbol{\theta}}(\boldsymbol{x}, \boldsymbol{\theta})}{f_{\boldsymbol{X}|\boldsymbol{\theta}}(\boldsymbol{x}, \widehat{\boldsymbol{\theta}})} f_{\boldsymbol{X}|\boldsymbol{\theta}}(\boldsymbol{x}, \widehat{\boldsymbol{\theta}}) d\boldsymbol{x}, \tag{8.4}$$

as long as $f_{\boldsymbol{X}|\boldsymbol{\theta}}(\boldsymbol{x}, \widehat{\boldsymbol{\theta}}) \neq 0$ on the entire $\Omega_{\boldsymbol{X}}$.
Eq. (8.4) is the basis of importance sampling methods, and it essentially means that we can calculate the expectation in Eq. (8.3) w.r.t. $f_{\boldsymbol{X}|\boldsymbol{\theta}}(\boldsymbol{x}, \boldsymbol{\theta})$, simply by re-weighting the samples from the reference distribution $f_{\boldsymbol{X}}(\boldsymbol{x})$ with the ratio of the two distributions, at no additional cost.

In other words, if both the values of $P_{f|\boldsymbol{x}}(\boldsymbol{x})$ are available for all the points used to calculate $P_{f|\boldsymbol{\theta}}(\boldsymbol{\theta})$ in Eq (8.3), and the corresponding values of both $\boldsymbol{x}^{(i)}$ and $f_{\boldsymbol{X}}(\boldsymbol{x}^{(i)})$, no additional calculation is needed to calculate the failure probability corresponding to any given $\boldsymbol{\theta}$:

$$P_{f|\boldsymbol{\theta}}(\boldsymbol{\theta}) \sim \frac{1}{N} \sum_{i=1}^{N} P_{f|\boldsymbol{x}}\left(\boldsymbol{x}^{(i)}\right) \frac{f_{\boldsymbol{X}|\boldsymbol{\theta}}(\boldsymbol{x}^{(i)}, \boldsymbol{\theta})}{f_{\boldsymbol{X}}(\boldsymbol{x}^{(i)})}. \tag{8.5}$$

8.5 Results

Because the wind turbine under observation has two different working regimes: operational and parked, two different failure probability analysis are performed. In particular, the limit states that are activate in the two regimes are different, as the von Mises stress at the tower bottom is dominant at the operational regimes, while the stress at the mudline is dominant in parked conditions. Conventionally, the two regimes are classified based on the mean windspeed U, with the turbine being operational in the interval $3m/s < U_{hub} < 25m/s$, and parked otherwise. Moreover, we assume that the the parked failure probability for $U_{hub} < 3m/s$ is negligible, and we therefore set it to zero in our analysis.

To perform this analysis, we use two separate datasets of conditional failure probabilities calculated from the reference $f_{\boldsymbol{X}}(\boldsymbol{x})$, depicted for reference in Figure 8.1. The operational dataset consists of a total of $N_{\boldsymbol{x}} = 52,534$ samples of the original distribution $f_{\boldsymbol{X}}(\boldsymbol{x})$ from Kelly and Vanem (2022), while the parked dataset uses $N_{\boldsymbol{x}} = 52,055$ samples from the same distribution, but conditioned on $U_{hub} > 25m/s$.

In both cases, a total of $N = 250$ bootstrap replications are performed on the original Teesside dataset, hence resulting in the same number of conditional $f_{\boldsymbol{X}|\boldsymbol{\theta}}(\boldsymbol{x}, \boldsymbol{\theta})$'s, as well failure probability estimates.

8.5.1 Operational failure results

The histogram of the estimated failure probabilities from the operational dataset is reported in Figure 8.2. (note that the scale is logarithmic on the $x-$axis). The corresponding median failure probability in operational conditions is then $P_f = 3.8 \cdot 10^{-21}$, with a 90% confidence interval $P_f^{\text{op}} \in [1.9, 6.7] \cdot 10^{-21}$.

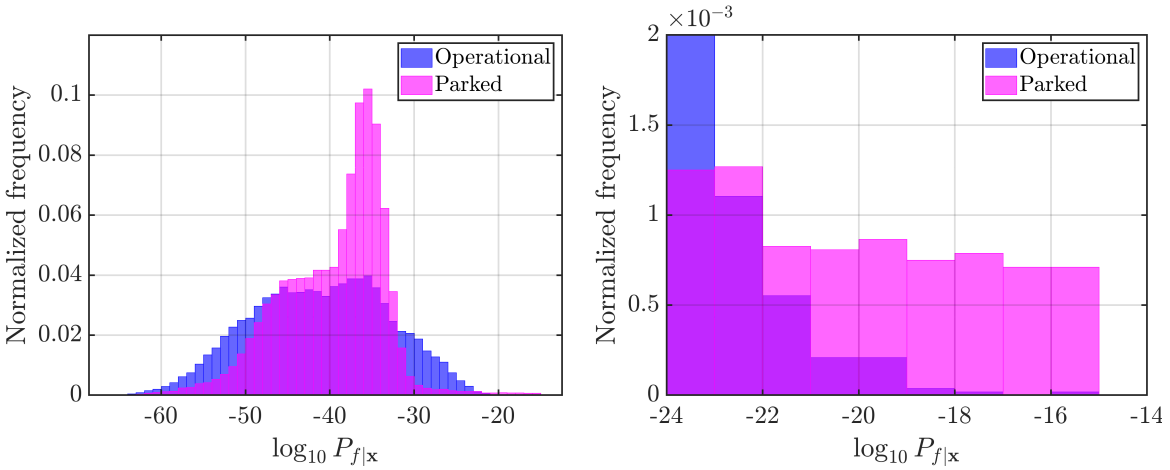

Figure 8.1: Distribution of the raw conditional probabilities used for the robustness analysis in Section 8 in logarithmic scale for operational (blue) and parked (orange) regimes. The left panel showcases the entire distribution, while the right panel focuses only on the upper tail of the distributions, as it is the region that has the highest impact on the expected failure probability in Eq. (8.3). Note that the dataset for parked regime sampled from a conditional distribution with $U_{hub} > 25m/s$. Therefore, despite its overall higher failure probability, it has minimal effect on the overall failure probability, because $\mathcal{P}(U_{hub} > 25m/s) \approx 8 \cdot 10^{-5}$ in Teesside.

8.5.2 Parked failure probability

Similarly, the histogram of the estimated failure probabilities from the parked dataset is reported in Figure 8.3. The corresponding median failure probability in parked conditions with $U_{hub} > 25m/s$ is $P_f = 3.9 \cdot 10^{-18}$, with a 90% confidence interval $P_f^{\text{prk}} \in [1.7, 7.4] \cdot 10^{-18}$. As expected, the failure probability in this range is almost exactly 3 orders of magnitude higher than that in operational conditions. Its confidence bounds are also slightly larger, likely due to them belonging to a relatively far tail of the input distribution, less constrained than other parts of the input domain. Nevertheless, due to the relatively low probability of $\mathcal{P}(U_{hub} > 25m/s) < 10^{-4}$, it is expected that the impact of parked failure will be minor on the total failure probability.

8.5.3 Combined failure probability

The combined failure probability of both operational and parked regimes is simply given by:

$$P_f = (1 - p) \cdot P_f^{\text{op}} + p \cdot P_f^{\text{prk}}, \tag{8.6}$$

where $p = \mathcal{P}(U_{hub} > 25m/s)$ is the probability that $U_{hub} > 25m/s$. In the case of Teesside, $p \approx 8 \cdot 10^{-5}$ The histogram of the estimated failure probabilities from the parked dataset is reported in Figure 8.4. The corresponding median combined failure probability is $P_f = 4.1 \cdot 10^{-21}$, with a 90% confidence interval $P_f \in [2.1, 7.1] \cdot 10^{-21}$, slightly higher than for the operational case.

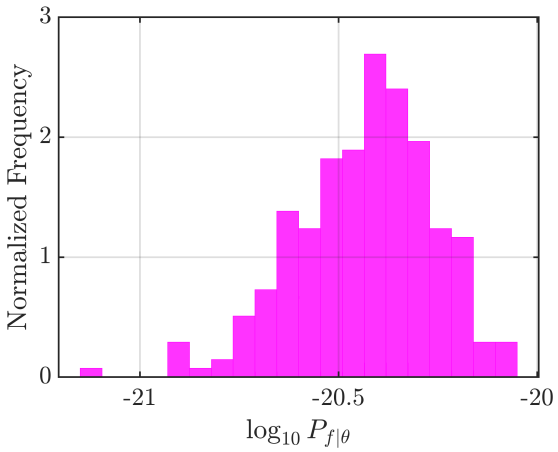

Figure 8.2: Distribution of the failure probabilities conditional on $\boldsymbol{\theta}$ obtained from the bootstrap estimates described in Section 8.3, for the operational regime. They correspond to the weighted average of the $P_{f|\boldsymbol{x}}(\boldsymbol{x})$ shown in Figure 8.1, for each bootstrap replication of $\boldsymbol{\theta}$ (see Section 8.3 and Eq (8.5)).

.

8.6 Wrap up and discussion on the robustness analysis

Our robustness analysis showcases that the uncertainty on the joint model of the environmental input parameters plays a significant role on the accuracy and confidence of the final failure probability estimation. The results are summarized in Table 8.1. As expected, the

Table 8.1: Summary of the robustness analysis results on the failure probability at different regimes

Regime	Mean	Std	q_{50} $(q_5 - q_{95})$
P_f^{op}	4.0×10^{-21}	1.5×10^{-21}	3.8 $(1.9 - 6.7) \times 10^{-21}$
P_f^{prk}	4.1×10^{-18}	1.7×10^{-18}	3.8 $(1.7 - 7.4) \times 10^{-18}$
P_f	4.3×10^{-21}	1.5×10^{-21}	4.1 $(2.1 - 7.1) \times 10^{-21}$

parking failure probability conditioned on $U_{hub} > 25m/s$ shows both a higher failure probability and larger variability, which are slightly reflected in the combined failure probability.

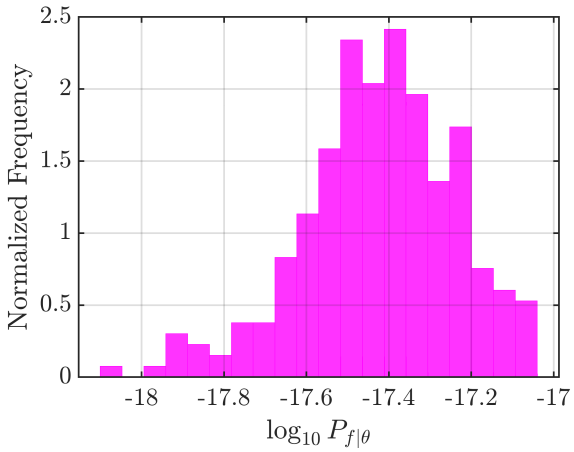

Figure 8.3: Distribution of the failure probabilities conditional on $\boldsymbol{\theta}$ obtained from the bootstrap estimates described in Section 8.3, for the parked regime. They correspond to the weighted average of the $P_{f|\boldsymbol{x}}(\boldsymbol{x})$ shown in Figure 8.1, for each bootstrap replication of $\boldsymbol{\theta}$ (see Section 8.3 and Eq (8.5)).

.

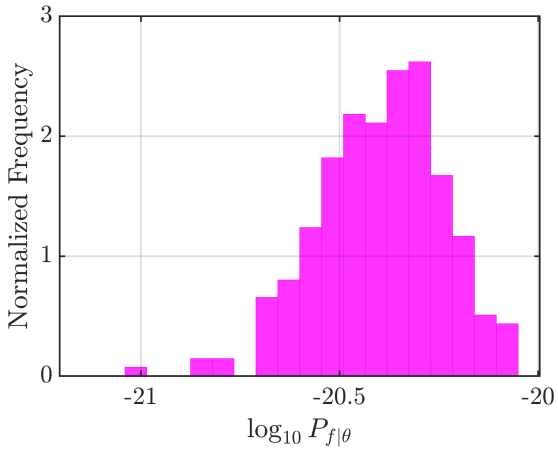

Figure 8.4: Distribution of the failure probabilities conditional on $\boldsymbol{\theta}$ obtained from the bootstrap estimates described in Section 8.3, for the combined operational+parked case. The effect of the parked regime is barely noticeable w.r.t. to the operational case in Figure 8.2, because of the very low conditional probability of $U_{hub} > 25m/s$.

9 Conclusions and perspectives

To leverage the use of reliability in the ULS design check of OWT, several methods have been studied for computing the annual failure probability, taking into account the uncertainty in the environmental (wind and wave) conditions, both in LT and ST parameters, model uncertainty with yaw misalignement, and material resistance uncertainty. Following international standard design basis classification IEC (2019b,a); DNVGL (2018), we distinguished the case of stationary loading event and the case of transient events, the latter including possible wind gust fitting real observations Kelly and Vanem (2022) and grid loss. Two realistic case studies are considered. The first case study is inspired from the OWT of Teesside wind farm of EDF in the West coast of UK. The 2.3MW turbine is supported on a cylindrical monopile foundation. The second case study is composed of the IEA15MW wind turbine supported on UMaine semi-submersible floater that is equipped with 3 catenary mooring lines, as developed in Allen et al. (2020) and then modified during HIPERWIND project, to be consistent with a site in South Brittany (West coast of France) Capaldo et al. (2021); Peyrard et al. (2022).

For the case of stationary ULS, four methods have been compared on a simplified 2D benchmark (in mean speed and turbulence space) with NREL 5MW wind turbine and the auto-regressive mNARX surrogate developed in Dimitrov et al. (2022); Schär et al. (2023) to replace the costly multiphysics simulator. The methods considered are environmental contours, BNN, GP with sequential sampling and outcrossing optimisation in jointed LT and ST spaces. The BNN approach did not succeed to compute accurately the annual failure probability with a feasible computational time because of non-Gaussian tail distribution of ULS. The outcrossing optimization could not converge in both ST and LT parametric space probably because of unexpected complexity of the high dimension reliability problem which limits the validity of FORM, with multiple non connected local minima. Another reason which could explain this difficulty may be due to the lack of identifiability between the LT and ST coefficients. Consequently, the only solution was to perform FORM for fixed LT which would require to much computations in the end.

Fortunately, the GP with sequential sampling succeeded to converge in computing the return value loads and annual failure probability with a small number of iterations. For a given point of a DoE in LT space, this method computes the extreme quantity (maximum of time series of load on OWT component) for multiple stochastic seeds accounting for the wind turbulence and wave irregularity. Then it fits a Gumbel distribution to the maxima, characterizing the ST failure conditional to LT parameters. Last, a GP of the Gumbel parameters is computed in LT space which then allows to compute the LT failure probability. This method is shown to provide similar loads than the Q90 environmental contour for Teesside case study, while for the South-Brittany case study, the failure domain appears to be located inside the contour. As South-Brittany case study in the 2D benchmark is just changing the runtime of simulations (1h instead of 10min) and the joint wind parameter distribution, the reason for this distribution of the failure domain was not identified. Also, the convergence in failure probability is less good than for return value period and slightly underestimates the value obtained with brute force sampling. This can be explained by very few outliers points in the ST maxima significantly deviating from the fitted Gumbel fit which we think are due to the use of mNARX out of its training domain and thus would not occur when using a physical simulator of offshore wind turbine dynamics.

For the case of transient ULS, a comparison of the observation-fitted gust with the IEC EOG has shown that it is possible to find some correspondence after fitting of the gust acceleration and rise-time parameters. An analysis of simulation results indicates that the ST parameter influence on ULS is small, so that the ST uncertainty can be neglected by considering only one stochastic seed. For the LT wind and wave parameters, augmented by the gust and shutdown parameters, a massive MC sampling underlines the role of gust acceleration in increasing significantly the loading when compared to the stationary ULS in similar environment conditions. To reduce the computation cost of the MC sampling, a method is presented which involves a GP surrogate that is enriched in several steps, according to the SUR-Bichon active learning criterion of Duhamel et al. (2023).

When applying the methods to Teesside use case, the critical limit state were found to be on monopile bending plasticity at mudline in extreme parked stationary condition. The GP with sequential sampling method computed an annual failure probability of several order magnitudes lower than the 1E-4 target of OWT design standards IEC (2019b); DNVGL (2018). This conservatism motivated an optimisation of the design which founds a new configuration with 21% mass reduction in tower and monopile and satisfies other design criteria : buckling, tower resonance and manufacturability. The optimisation was possible without additional simulations by taking advantage that the bending moments are not significantly changed when reducing the tower and monopile thickness.

The same methods was also applied to South Brittany use case for computing the annual probability of tower base bending plasticity. It was found to be close to the 1E-4 target so that no optimisation with tower mass reduction was investigated.

Many perspectives can be suggested to this work. Firstly, additional work could be done to address the limitations of the stationary ULS methods which did not succeeded to converge efficiently. The limitation of BNN in predicting the ULS tail distribution could be alleviated by replacing the Gaussian distribution choice with a more flexible one like the Generalized Lambda distribution of Zhu and Sudret (2021). The limitation of the outcrossing optimization approach with FORM could also be alleviated by employing dimension reduction techniques (see references in Breaz et al. (2024)). Despite the implementation of the Gaussian process with sequential sampling method used in this work gave satisfaction, it would be worth to check possible improvements for the ST asymptotic load analysis, with strategies for de-clustering the local maxima (e.g. Block Maxima, Average Conditional Exceedance Rates method of Naess and Gaidai (2009)) and other distributions for load maxima, as documented in Dimitrov (2016).

Secondly, it could be interesting to work on a case study for which the transient event is critical, for instance by reconsidering strong misalignement of DLC6.2 IEC (2019a). The GP with active learning approach should be improved with a Bayesian subset simulation strategy Bect et al. (2017) managing the possible failures of convergence of the simulator.

A third perspective of this work concerns the Teesside application. The demonstration could be completed by considering additional limit states, both in terms of loading condition and for the selection of the failure mechanism. Also, despite a considerable conservatism found in HIPERWIND D4.3 for monopile fatigue on Teesside, it would be worth checking that FLS constraint on monopile and tower base plasticity are still satisfied on the new design obtained with mass reduction. In this optimization exercise, one may enlarge the reliability constraints set by including FLS, using the same assumption that bending moment

is preserved when reducing the tower and monopile thickness.

A fourth perspective concerns the floating South Brittany application. Like in the recent work of Nielsen et al. (2023) based on IEC standard philosophy, we chose to compute the annual failure probability for one DLC independently of the others, here the parked configuration assumed to be the critical one, i.e. the one providing the most unacceptable limit state function. We could however have chosen to compute a more representative failure probability considering both operational and parked configurations, each of them being weighted by their probability of occurrence like in equation 8.6 of section 8. If the parked configuration was indeed the most critical one, the resulting probability would then be smaller, allowing for possible optimisation. Furthermore, instead of the tower mass reduction, one may also look at reducing the clump weights on the mooring lines (see details in Peyrard et al. (2022)) and check that the tension on the mooring lines is still positive in a probabilistic framework. As this tension will obviously change drastically when reducing the clump weights, this will require to solve the challenging problem of defining a surrogate model of this dependency.

Last but not least, it is worth mentioning that with the demonstration done in this work, complementary work should be devoted to complete filling the TRL gap for using such reliability approaches in future industrial OWT designs. This program requires collaborative exchange between the researchers, the offshore wind farm operators and the standard organizations to better identify the roadmap.

Acknowledgement

The work is a part of the HIghly advanced Probabilistic design and Enhanced Reliability methods for the high-value, cost-efficient offshore WIND (HIPERWIND) project, which has received funding from the European Union's Horizon 2020 Research and Innovation Programme under Grant Agreement No. 101006689. The authors are grateful to their colleagues of IFPEN, DTU, DNV, ETH and EDF who have provided technical support to this work.

References

K. Aas, C. Czado, A. Frigessi, and H. Bakken. Pair-copula constructions of multiple dependence. Insurance: Mathematics and Economics, 44(2):182–198, 2009.

Airbus-EDF-IMACS-ONERA-Phimeca. Openturns v1.22, 2024. URL https://openturns.github.io/openturns/latest/user_manual/_generated/openturns.KarhunenLoeveSVDAlgorithm.html.

H. Akaike. Maximum likelihood identification of Gaussian autoregressive moving average models. Biometrika, 60(2):255–265, 08 1973.

C. Allen, A. Viscelli, H. Dagher, A. Goupee, E. Gaertner, N. Abbas, M. Hall, and G. Barter. Definition of the UMaine VolturnUS-S reference platform developed for the IEA wind 15-megawatt offshore reference wind turbine. Technical report, National Renewable Energy Lab.(NREL), Golden, CO (United States); Univ. of . . . , 2020.

C. Andrieu-Renaud, B. Sudret, and M. Lemaire. The PHI2 method: a way to compute time-variant reliability. Reliability Engineering & System Safety, 84(1):75–86, Apr. 2004. ISSN 0951-8320. doi: 10.1016/j.ress.2003.10.005. URL https://www.sciencedirect.com/science/article/pii/S0951832003002321.

E. Ardillon, B. P. M., A. Cousin, N. Dimitrov, M. Dupoiron, S. Eldevik, E. Fekhari, F. C., M. Guiton, J. B., P.-A. Joulin, A. Lovera, L. Mayol, and P. M.M. Deliverable 3.2: Turbine loading and wake model uncertainty. Technical report, EU Horizon2020 Hiperwind, 2022.

Y. Auffray, P. Barbillon, and J.-M. Marin. Maximin design on non hypercube domains and kernel interpolation. Statistics and Computing, 22:703–712, 2012.

J.-M. Azäis and M. Wschebor. Level Sets and Extrema of Random Processes and Fields: Azaïs/Level Sets and Extrema of Random Processes and Fields. John Wiley & Sons, Inc., Hoboken, NJ, USA, Feb. 2009. ISBN 978-0-470-43464-2 978-0-470-40933-6. doi: 10.1002/9780470434642. URL http://doi.wiley.com/10.1002/9780470434642.

G. Baarholm, S. Haver, and O. Økland. Combining contours of significant wave height and peak period with platform response distributions for predicting design response. Marine Structures, 23:147–163, 2010.

J. Bect, D. Ginsbourger, L. Li, V. Picheny, and E. Vazquez. Sequential design of computer experiments for the estimation of a probability of failure. Statistics and Computing, 22 (3):773–793, 2012.

J. Bect, L. Li, and E. Vazquez. Bayesian subset simulation. SIAM/ASA Journal on Uncertainty Quantification, 5(1):762–786, 2017.

C. Blundell, J. Cornebise, K. Kavukcuoglu, and D. Wierstra. Weight uncertainty in neural networks. In F. Bach and D. Blei, editors, Proceedings of the 32nd International Conference on Machine Learning, volume 37 of Proceedings of Machine Learning Research, pages 1613–1622, Lille, France, 07–09 Jul 2015. PMLR. URL https://proceedings.mlr.press/v37/blundell15.html.

E. Branlard, J. Jonkman, C. Brown, and J. Zhang. A digital twin solution for floating offshore wind turbines validated using a full-scale prototype. Wind Energy Science, 9(1): 1–24, 2024. doi: 10.5194/wes-9-1-2024. URL https://wes.copernicus.org/articles/9/1/2024/.

V. Breaz, M. Munoz Zuniga, and O. Zahm. Literature review on rare event probability estimation in high dimension. working paper or preprint, 2024. URL https://hal.archives-ouvertes.fr/hal-04564739.

M. Capaldo, M. Guiton, G. Huwart, E. Julan, N. Krasimirov Dimitrov, T. Kim, A. Lovera, and C. Peyrard. Design brief of HIPERWIND offshore wind turbine cases: bottom fixed 10MW and floating 15MW. Technical report, EU Horizon2020 Hiperwind, June 2021. URL https://ifp.hal.science/hal-04033059.

W. Carswell, S. R. Arwade, D. J. DeGroot, and M. A. Lackner. Soil–structure reliability of offshore wind turbine monopile foundations. Wind Energy, 18(3):483–498, 2015. doi: https://doi.org/10.1002/we.1710. URL https://onlinelibrary.wiley.com/doi/abs/10.1002/we.1710.

D. Castellon, A. Fenerci, and O. Øiseth. Environmental contours for wind-resistant bridge design in complex terrain. Journal of Wind Engineering and Industrial Aerodynamics, 224(104943), 2022.

W. Chai and B. Leira. Environmental contours based on inverse sorm. Marine Structures, 60:34–51, 2018.

E. J. Chen, L. Ding, Y. Liu, X. Ma, and M. J. Skibniewski. On spectral representation method and Karhunen–Loève expansion in modelling construction material properties. Archives of Civil and Mechanical Engineering, 18(3):768–783, July 2018. ISSN 1644-9665. doi: 10.1016/j.acme.2017.12.008. URL https://www.sciencedirect.com/science/article/pii/S1644966517302054.

X. Chen, T. Hasselman, and D. Neill. Reliability based structural design optimization for practical applications. In 38th Structures, Structural Dynamics, and Materials Conference, 1997. doi: 10.2514/6.1997-1403. URL https://arc.aiaa.org/doi/abs/10.2514/6.1997-1403.

M. Chiron, C. Genest, J. Morio, and S. Dubreuil. Failure probability estimation through high-dimensional elliptical distribution modeling with multiple importance sampling. Reliability Engineering & System Safety, 235:109238, 2023.

A. Cousin. Optimisation sous contraintes fiabilistes de systèmes complexes. Application au dimensionnement d'une éolienne offshore flottante. Theses, Ecole polytechnique, Palaiseau, 2021.

A. Cousin, N. Delépine, M. Guiton, M. Munoz Zuniga, and T. Perdrizet. Optimal design of experiments for computing the fatigue life of an offshore wind turbine based on stepwise uncertainty reduction. Structural Safety, 2024. doi: doi:https://doi.org/10.1016/j.strusafe.2024.102483.

N. Dimitrov. Comparative analysis of methods for modelling the short-term probability distribution of extreme wind turbine loads. Wind Energy, 19(4):717–737, 2016. doi: https://doi.org/10.1002/we.1861. URL https://onlinelibrary.wiley.com/doi/abs/10.1002/we.1861.

N. Dimitrov. HiperSim. https://gitlab.windenergy.dtu.dk/HiperSim/hipersim, 2023.

N. Dimitrov and T. Göçmen. Virtual sensors for wind turbines with machine learning-based time series models. Wind Energy, 25(9):1626–1645, 2022. doi: https://doi.org/10.1002/we.2762. URL https://onlinelibrary.wiley.com/doi/abs/10.1002/we.2762.

N. Dimitrov and A. Natarajan. From scada to lifetime assessment and performance optimization: how to use models and machine learning to extract useful insights from limited data. Journal of Physics: Conference Series, 1222(1):012032, may 2019. doi: 10.1088/1742-6596/1222/1/012032. URL https://dx.doi.org/10.1088/1742-6596/1222/1/012032.

N. Dimitrov, M. C. Kelly, A. Vignaroli, and J. Berg. From wind to loads: wind turbine site-specific load estimation with surrogate models trained on high-fidelity load databases. Wind Energy Science, 3(2):767–790, 2018. doi: 10.5194/wes-3-767-2018. URL https://wes.copernicus.org/articles/3/767/2018/.

N. Dimitrov, S. Marelli, and S. Schar. Deliverable 4.1: Novel surrogate modelling approaches for wind turbine reliability assessment. Technical report, EU Horizon2020 Hiperwind, 2022.

DNV. DNV-RP-C205: Environmental conditions and environmental loads. september 2019 edition. Technical report, DNV, 2021.

DNVGL. DNVGL-ST-0437: Loads and site conditions for wind turbines. november 2016 edition. Technical report, DNVGL, 2016.

DNVGL. DNVGL-ST-0119 Floating Wind Turbine Structures: Technical Report. Technical report, DNVGL, Høvik, 2018.

X. Du and W. Chen. Sequential Optimization and Reliability Assessment Method for Efficient Probabilistic Design . Journal of Mechanical Design, 126(2):225–233, 05 2004. ISSN 1050-0472. doi: 10.1115/1.1649968. URL https://doi.org/10.1115/1.1649968.

C. Duhamel, C. Helbert, M. Munoz Zuniga, C. Prieur, and D. Sinoquet. A SUR version of the Bichon criterion for excursion set estimation. Statistics and Computing, 33(2):41, Feb. 2023. ISSN 1573-1375. doi: 10.1007/s11222-023-10208-4. URL https://doi.org/10.1007/s11222-023-10208-4.

K. Dykes, A. Platt, Y. Guo, A. Ning, R. King, T. Parsons, D. Petch, P. Veers, and R. B. Effect of tip-speed constraints on the optimized design of a wind turbine. Technical Report NREL/TP-5000-61726, NREL, 2014.

EDF. Teesside wind farm. https://www.edf.fr/sites/default/files/contrib/groupe-edf/espaces-dedies/espace-medias/dp/dp_edf-teesside-offshore-wind-farm.pdf, 2014. Accessed: 2024-04-26.

B. Efron. Bootstrap Methods: Another Look at the Jackknife. The Annals of Statistics, 7(1):1 – 26, 1979. doi: 10.1214/aos/1176344552. URL https://doi.org/10.1214/aos/1176344552.

Eurocode. Eurocode 3: design of steel structures—part 1-6: general rules—supplementary rules for the shell structures. technical report en 1993-1-6: 20xx, european committee for standardisation, 1993. Technical report, European Committee for Standardisation, 1993.

E. Fekhari, V. Chabridon, J. Muré, and B. Iooss. Given-data probabilistic fatigue assessment for offshore wind turbines using bayesian quadrature. Data-Centric Engineering, 5:e5, 2024. doi: 10.1017/dce.2023.27.

R. V. Field and M. Grigoriu. On the accuracy of the polynomial chaos approximation. Probabilistic Engineering Mechanics, 19(1):65–80, Jan. 2004. ISSN 0266-8920. doi: 10.1016/j.probengmech.2003.11.017. URL https://www.sciencedirect.com/science/article/pii/S0266892003000729.

R. G. Ghanem and P. D. Spanos. Stochastic Finite Elements: A Spectral Approach. Springer, New York, NY, 1991. ISBN 978-1-4612-7795-8 978-1-4612-3094-6. doi: 10.1007/978-1-4612-3094-6. URL http://link.springer.com/10.1007/978-1-4612-3094-6.

F.-I. Giske, K. Kvåle, B. Leira, and O. Øiseth. Long-term extreme response analysis of a long-span pontoon bridge. Marine Structures, 58:154–171, 2018.

I. Goodfellow, Y. Bengio, and A. Courville. Deep Learning. MIT Press, 2016.

O. Gramstad, C. Agrell, E. M. Bitner-Gregersen, B. Guo, E. Ruth, and E. Vanem. Sequential sampling method using gaussian process regression for estimating extreme structural response. Marine Structures, 72:102780, 2020.

M. Grigoriu. Evaluation of Karhunen–Loève, Spectral, and Sampling Representations for Stochastic Processes. Journal of Engineering Mechanics, 132(2):179–189, Feb. 2006. ISSN 0733-9399. doi: 10.1061/(ASCE)0733-9399(2006)132:2(179). URL https://ascelibrary.org/doi/10.1061/%28ASCE%290733-9399%282006%29132%3A2%28179%29. Publisher: American Society of Civil Engineers.

B. G.S. and T. Moan. Application of contour line method to estimate extreme ship hull loads considering operational restrictions. Journal of Ship Research, 45:228–240, 2001.

GWEC. Global offshore wind report 2023. Technical report, Global Wind Energy Council, 2023.

A. Haselsteiner, J.-H. Ohlendorf, W. Wosniok, and K.-D. Thoben. Deriving environmental contours from highest density regions. Coastal Engineering, 123:42–51, 2017.

A. Haselsteiner, R. Coe, L. Manuel, W. Chai, B. Leira, G. Clarindo, C. Soares, A. Hannesdottir, N. Dimitrov, N. Sander, J. Ohlendorf, K. Thoben, G. de Hauteclocque, E. Mackay, P. Jonathan, C. Qiao, A. Myers, A. Rode, A. Hildebrandt, B. Schmidt, E. Vanem, and A. Huseby. A benchmarking exercise for environmental contours. Ocean Engineering, 236(109504), 2021.

S. Haver and S. Winterstein. Environmental contour lines: A method for estimating long term extremes by a short term analysis. Transactions of the Society of Naval Architects and Marine Engineers, 116:116–127, 2009.

J.-T. Horn, J. R. Krokstad, and B. J. Leira. Impact of model uncertainties on the fatigue reliability of offshore wind turbines. Marine Structures, 64:174–185, 2019. ISSN 0951-8339. doi: https://doi.org/10.1016/j.marstruc.2018.11.004. URL https://www.sciencedirect.com/science/article/pii/S0951833918302363.

S. P. Huang, S. T. Quek, and K. K. Phoon. Convergence study of the truncated Karhunen–Loève expansion for simulation of stochastic processes. International Journal for Numerical Methods in Engineering, 52(9):1029–1043, 2001. ISSN 1097-0207. doi: 10.1002/nme.255. URL https://onlinelibrary.wiley.com/doi/abs/10.1002/nme.255. _eprint: https://onlinelibrary.wiley.com/doi/pdf/10.1002/nme.255.

Q. Huchet, C. Mattrand, P. Beaurepaire, N. Relun, and N. Gayton. Ak-da: An efficient method for the fatigue assessment of wind turbine structures. Wind Energy, 22(5):638–652, 2019. doi: https://doi.org/10.1002/we.2312. URL https://onlinelibrary.wiley.com/doi/abs/10.1002/we.2312.

A. Huseby, E. Vanem, and B. Natvig. A new approach to environmental contours for ocean engineering applications based on direct monte carlo simulations. Ocean Engineering, 60:124–135, 2013.

A. Huseby, E. Vanem, and B. Natvig. Alternative environmental contours for structural reliability analysis. Structural Safety, 54:32–45, 2015.

IEC. IEC 61400-1. wind turbines – part 1: Design requirements. edition 4.0 2019-02. Technical report, International Electrotechnical Commission, 2019a.

IEC. IEC 61400-3 Wind turbines - Part 3 : Design requirements for offshore wind turbines. edition 1.0 2019-04. Standard, International Electrotechnical Commission, 2019b.

IEC. IEC CD TS 61400-9; Wind Energy Generation Systems—Part 9: Probabilistic Design Measures for Wind Turbines. Technical report, International Electrotechnical Commission, 2023.

JCSS. JCSS probabilistic model code. Part 3: Resistance models. 3.12 Fatigue models for metallic structures. Technical report, Joint Committee on Structural Safety, 2011.

J. J. Jensen and J. Capul. Extreme response predictions for jack-up units in second order stochastic waves by form. Probabilistic Engineering Mechanics, 21(4):330–337, 2006. ISSN 0266-8920. doi: https://doi.org/10.1016/j.probengmech.2005.11.007. URL https://www.sciencedirect.com/science/article/pii/S0266892005000834.

J. Jonkman, S. Butterfield, W. Musial, and G. Scott. Definition of a 5-MW reference wind turbine for offshore system development. Technical report, National Renewable Energy Laboratory, 2009.

T. Kadota. Differentiation of Karhunen-Loève expansion and application to optimum reception of sure signals in noise. IEEE Transactions on Information Theory, 13(2):255–260, 1967. doi: 10.1109/TIT.1967.1054009.

L. Katafygiotis and K. Zuev. Geometric insight into the challenges of solving high-dimensional reliability problems. Probabilistic Engineering Mechanics, 23(2):208 – 218, 2008. ISSN 0266-8920. doi: https://doi.org/10.1016/j.probengmech.2007.12.026. URL http://www.sciencedirect.com/science/article/pii/S0266892007000707. 5th International Conference on Computational Stochastic Mechanics.

N. Kelley and B. Jonkman. Overview of the turbsim stochastic inflow turbulence simulator. Technical report, NREL, 2007. URL https://www.nrel.gov/wind/nwtc/assets/pdfs/turbsimoverview.pdf.

M. Kelly. From standard wind measurements to spectral characterization: turbulence length scale and distribution. Wind Energy Science, 3(2):533–543, 2018. doi: 10.5194/wes-3-533-2018. URL https://wes.copernicus.org/articles/3/533/2018/.

M. Kelly and E. Vanem. Deliverable 2.3: Environmental joint probability distributions and uncertainties. Technical report, EU Horizon2020 Hiperwind, 2022.

H. Koo, A. Der Kiureghian, and K. Fujimura. Design-point excitation for non-linear random vibrations. Probabilistic Engineering Mechanics, 20:136–147, 2005.

R. Lebrun and A. Dutfoy. Do Rosenblatt and Nataf isoprobabilistic transformations really differ ? Probabilistic Engineering Mechanics, 24(4):577–584, 2009a. ISSN 0266-8920. doi: https://doi.org/10.1016/j.probengmech.2009.04.006. URL https://www.sciencedirect.com/science/article/pii/S0266892009000307.

R. Lebrun and A. Dutfoy. A generalization of the nataf transformation to distributions with elliptical copula. Probabilistic Engineering Mechanics, 24(2):172–178, 2009b. ISSN 0266-8920. doi: https://doi.org/10.1016/j.probengmech.2008.05.001. URL https://www.sciencedirect.com/science/article/pii/S0266892008000507.

B. Leira. A comparison of stochastic process models for definition of design contours. Structural Safety, 30:493–505, 2008.

M. Lemaire, A. Chateauneuf, and J. Mitteau. Reliability of Systems. John Wiley & Sons, Ltd, 2009.

H. Li and C. Guedes Soares. Assessment of failure rates and reliability of floating offshore wind turbines. Reliability Engineering & System Safety, 228:108777, 2022. ISSN 0951-8320. doi: https://doi.org/10.1016/j.ress.2022.108777. URL https://www.sciencedirect.com/science/article/pii/S0951832022004008.

Q. Li, Z. Gao, and T. Moan. Modified environmental contour method for predicting long-term extreme responses of bottom-fixed offshore wind turbines. Marine Structures, 48: 15–32, 2016.

G. Lloyd. Guideline for the certification of offshore wind turbines. iv – part 2, chapter 6. Technical report, Germanischer Lloyd, 2005.

M. Loève. Probability theory, vol. ii. Graduate texts in mathematics, 46:0–387, 1978.

L. Lutes and S. Winterstein. A dynamic inverse form method: Design contours for load combination problems. Probabilistic Engineering Mechanics, 44:118–127, 2016.

J. Mann. The spatial structure of neutral atmospheric surface-layer turbulence. Journal of Fluid Mechanics, 273:141 – 168, 1994. doi: 10.1017/S0022112094001886. URL https://www.scopus.com/inward/record.uri?eid=2-s2.0-0028481033&doi=10.1017%2fS0022112094001886&partnerID=40&md5=ef291319b687b75f877bc3b68f82f2c2. Cited by: 513.

J. Mann. Wind field simulation. Probabilistic Engineering Mechanics, 13(4):269–282, 1998. ISSN 0266-8920. doi: https://doi.org/10.1016/S0266-8920(97)00036-2. URL https://www.sciencedirect.com/science/article/pii/S0266892097000362.

L. Manuel, P. Nguyen, J. Canning, R. Coe, A. Eckert-Gallup, and N. Martin. Alternative approaches to develop environmental contours from metocean data. Journal of Ocean Engineering and Marine Energy, 4:293–310, 2018.

S. Marelli and B. Sudret. Uqlab: A framework for uncertainty quantification in matlab. In Proc. 2nd Int. Conf. on Vulnerability, uncertainty, and risk: quantification, mitigation, and management (ICVRAM2014), pages 2554–2563, 2014.

R. Melchers. Importance sampling in structural systems. Structural Safety, 6:3–10, 1989.

M. A. Mohamad and T. P. Sapsis. Sequential sampling strategy for extreme event statistics in nonlinear dynamical systems. Proceedings of the National Academy of Sciences, 115 (44):11138–11143, 2018. doi: 10.1073/pnas.1813263115. URL https://www.pnas.org/doi/abs/10.1073/pnas.1813263115.

R. Montes-Iturrizaga and E. Heredia-Zavoni. Environmental contours using copulas. Applied Ocean Research, 52:125–139, 2015.

A. Morató and S. Sriramula. Calibration of safety factors for offshore wind turbine support structures using fully coupled simulations. Marine Structures, 75:102880, 2021. ISSN 0951-8339. doi: https://doi.org/10.1016/j.marstruc.2020.102880. URL https://www.sciencedirect.com/science/article/pii/S0951833920301738.

B. Moynihan, E. M. Tronci, M. C. Hughes, B. Moaveni, and E. Hines. Virtual sensing via gaussian process for bending moment response prediction of an offshore wind turbine using scada data. Renewable Energy, 227:120466, 2024. ISSN 0960-1481. doi: https://doi.org/10.1016/j.renene.2024.120466. URL https://www.sciencedirect.com/science/article/pii/S0960148124005317.

M. Muliawan, Z. Gao, and T. Moan. Application of the contour line method for estimating extreme responses in the mooring lines of a two-body floating wave energy converter. Journal of Offshore Mechanics and Arctic Engineering, 135(031301):1–10, 2013.

A. Murangira, M. Munoz Zuniga, and T. Perdrizet. Extreme mecanical response of a floating wind turbine under wind loading. Technical report, IFP Energies Nouvelles, 2015.

M. Muskulus and S. Schafhirt. Reliability-based design of wind turbine support structures. In Symposium on Reliability of Engineering System, SRES'2015, Hangzhou, China, Oct. 15-17, 10 2015. doi: 10.13140/RG.2.1.5125.5766.

K. Müller, M. Dazer, and P. W. Cheng. Damage assessment of floating offshore wind turbines using response surface modeling. Energy Procedia, 137:119–133, 10 2017. doi: 10.1016/j.egypro.2017.10.339.

A. Naess and O. Gaidai. Estimation of extreme values from sampled time series. Structural Safety, 31(4):325–334, 2009. ISSN 0167-4730. doi: https://doi.org/10.1016/j.strusafe.2008.06.021. URL https://www.sciencedirect.com/science/article/pii/S0167473008000829.

A. Nataf. Détermination des distributions dont les marges sont données. Technical report, Comptes Rendus de l'Académie des Sciences 225 (in French), 1962.

J. Niedzwwecki, J. van de Lindt, and J. Yao. Estimating extreme tendon response using environmental contours. Engineering Structures, 20:601–607, 1998.

J. S. Nielsen, H. S. Toft, and G. O. Violato. Risk-based assessment of the reliability level for extreme limit states in iec 61400-1. Energies, 16(4), 2023. ISSN 1996-1073. doi: 10.3390/en16041885. URL https://www.mdpi.com/1996-1073/16/4/1885.

NREL. Definition of the IEA Wind 15-Megawatt Offshore Reference Wind Turbine. Technical report, IEA Wind TCP Task 37, 2020.

NREL. OpenFAST documentation, release v2.5.0, s.l. Technical report, National Renewable Energy Laboratory, 2021.

NREL. Wind-plant Integrated System Design and Engineering Model (WISDEM). https://wisdem.readthedocs.io/en/master/, 2024.

B. Paz, Y. Liu, N. Hermoso, W. Remigius, and A. Abrahamsen. Deliverable 5.2: Electrical grid model. Technical report, EU Horizon2020 Hiperwind, 2023.

T. Perdrizet and D. Averbuch. Short and Long Term Extreme Reliability Analysis Applied to Floating Wind Turbine Design. In Proceedings of the ASME 2011 30th International Conference on Ocean, Offshore and Arctic Engineering, OMAE2011, pages 893–898. American Society of Mechanical Engineers Digital Collection, Oct. 2011. doi: 10.1115/OMAE2011-50264. URL https://manufacturingscience.asmedigitalcollection.asme.org/OMAE/proceedings/OMAE2011/44373/893/351023.

C. Peyrard, F. Robaux, A. Borras-Nadal, P.-A. Joulin, L. Mayol, S. Eldevik, M. Guiton, A. Cousin, M. Benoit, N. Dimitrov, L. A., and F. C. Deliverable 3.3: Aero-servo-hydroelastic model uncertainty. Technical report, EU Horizon2020 Hiperwind, 2022.

M. J. Powell. A direct search optimization method that models the objective and constraint functions by linear interpolation. Springer, 1994.

A. N. Robertson, K. Shaler, L. Sethuraman, and J. Jonkman. Sensitivity analysis of the effect of wind characteristics and turbine properties on wind turbine loads. Wind Energy Science, 4(3):479–513, 2019. doi: 10.5194/wes-4-479-2019. URL https://wes.copernicus.org/articles/4/479/2019/.

M. Rosenblatt. Remarks on a multivariate transformation. The Annals of Mathematical Statistics, 23(3):470–472, 1952. ISSN 00034851. URL http://www.jstor.org/stable/2236692.

E. Ross, O. Astrup, E. Bitner-Gregersen, N. Bunn, G. Feld, B. Gouldby, A. Huseby, Y. Liu, D. Randell, E. Vanem, and P. Jonathan. On environmental contours for marine and coastal design. Ocean Engineering, 195(106194), 2019.

G. Schall, M. H. Faber, and R. Rackwitz. The Ergodicity Assumption for Sea States in the Reliability Estimation of Offshore Structures. Journal of Offshore Mechanics and Arctic Engineering, 113(3):241–246, Aug. 1991. ISSN 0892-7219. doi: 10.1115/1.2919926. URL https://doi.org/10.1115/1.2919926.

S. Schär, S. Marelli, and B. Sudret. Emulating the dynamics of complex systems using autoregressive models on manifolds (mNARX), 2023.

M. Shinozuka and G. Deodatis. Simulation of stochastic processes by spectral representation. Applied Mechanics Review, 44:191–204, 1991.

A. A. Shittu, A. Mehmanparast, P. Amirafshari, P. Hart, and A. Kolios. Sensitivity analysis of design parameters for reliability assessment of offshore wind turbine jacket support structures. International Journal of Naval Architecture and Ocean Engineering, 14: 100441, 2022. ISSN 2092-6782. doi: https://doi.org/10.1016/j.ijnaoe.2022.100441. URL https://www.sciencedirect.com/science/article/pii/S2092678222000073.

F. Silva-González, E. Heredia-Zavoni, and R. Montes-Iturrizaga. Development of environmentalcontours using nataf distribution model. Applied Ocean Research, 58:27–34, 2013.

D. Sinoquet and H. Langoüet. Sqa: a generic trust region derivative free optimization method for black box industrial applications. In ICCOPT international conference on continuous optimization, 2013.

R. M. Slot, J. D. Sørensen, B. Sudret, L. Svenningsen, and M. L. Thøgersen. Surrogate model uncertainty in wind turbine reliability assessment. Renewable Energy, 151:1150–1162, 2020. ISSN 0960-1481. doi: https://doi.org/10.1016/j.renene.2019.11.101. URL https://www.sciencedirect.com/science/article/pii/S096014811931794X.

G. Stefanou and M. Papadrakakis. Assessment of spectral representation and Karhunen–Loéve expansion methods for the simulation of Gaussian stochastic fields. Computer Methods in Applied Mechanics and Engineering, 196(21):2465–2477, Apr. 2007. ISSN 0045-7825. doi: 10.1016/j.cma.2007.01.009. URL https://www.sciencedirect.com/science/article/pii/S0045782507000254.

L. E. S. Stieng and M. Muskulus. Reliability-based design optimization of offshore wind turbine support structures using analytical sensitivities and factorized uncertainty modeling. Wind Energy Science, 5(1):171–198, 2020. doi: 10.5194/wes-5-171-2020. URL https://wes.copernicus.org/articles/5/171/2020/.

B. Sudret. Analytical derivation of the outcrossing rate in time-variant reliability problems. Structure and Infrastructure Engineering - STRUCT INFRASTRUCT ENG, 4:353–362, 10 2008. doi: 10.1080/15732470701270058.

N. J. Tarp-Johansen, I. Kozine, L. Rademakers, J. D. Sørensen, and K. O. Ronold. Optimised and balanced structural and system reliability of offshore wind turbines. an account. Technical report, DTU, Risø-R-1420(EN), 2005. URL https://api.semanticscholar.org/CorpusID:59143129.

R. C. Taylor. Applications Of Dynamic Programming To Agricultural Decision Problems. Westview Press, 1993.

G. C. Tiao and G. E. P. Box. Bayesian inference in statistical analysis. Wiley, 1992.

E. Torre, S. Marelli, P. Embrechts, and B. Sudret. A general framework for data-driven uncertainty quantification under complex input dependencies using vine copulas. Probabilistic Engineering Mechanics, 55:1–16, 2019.

E. Torre, S. Marelli, and B. Sudret. UQLab user manual–Statistical inference. Chair of Risk, Safety and Uncertainty Quantification, ETH Zurich, 2022.

J. van de Lindt and J. Niedzwecki. Environmental contour analysis in earthquake engineering. Engineering Structures, 22:1661–1676, 2000.

S. F. van Eijk, R. Bos, and W. A. A. M. Bierbooms. The risks of extreme load extrapolation. Wind Energy Science, 2(2):377–386, 2017. doi: 10.5194/wes-2-377-2017. URL https://wes.copernicus.org/articles/2/377/2017/.

E. Vanem. 3-dimensional environmental contours based on a direct sampling method for structural reliability analysis of ships and offshore structures. Ships and Offshore Structures, 14:74–85, 2018.

E. Vanem, E. Fekhari, N. Dimitrov, M. Kelly, A. Cousin, and M. Guiton. A joint probability distribution model for multivariate wind and wave conditions. In ASME 2023 42nd International Conference on Ocean, Offshore and Arctic Engineering, 2023.

J. Velarde, E. Vanem, C. Kramhøft, and J. Sørensen. Probabilistic analysis of offshore wind turbines under extreme resonant response: Application of environmental contour method. Applied Ocean Research, 93(101947), 2019.

J. Velarde, A. Mankar, C. Kramhøft, and J. D. Sørensen. Probabilistic calibration of fatigue safety factors for offshore wind turbine concrete structures. Engineering Structures, 222: 111090, 2020. ISSN 0141-0296. doi: https://doi.org/10.1016/j.engstruct.2020.111090. URL https://www.sciencedirect.com/science/article/pii/S0141029619352010.

D. Veldkamp. A probabilistic evaluation of wind turbine fatigue design rules. Wind Energy, 11:655–672, 2008.

F. Vorpahl, H. Schwarze, T. Fischer, M. Seidel, and J. Jonkman. Offshore wind turbine environment, loads, simulation, and design. Wiley Interdisciplinary Reviews: Energy and Environment, 2, 09 2013. doi: 10.1002/wene.52.

K. Wang, O. Gaidai, F. Wang, X. Xu, T. Zhang, and H. Deng. Artificial neural network-based prediction of the extreme response of floating offshore wind turbines under operating conditions. Journal of Marine Science and Engineering, 11(9), 2023. ISSN 2077-1312. doi: 10.3390/jmse11091807. URL https://www.mdpi.com/2077-1312/11/9/1807.

L. Wang. Karhunen-Loève expansions and their applications. PhD thesis, London School of Economics and Political Science, 2008. URL https://etheses.lse.ac.uk/2950/.

L. Wang, A. Kolios, X. Liu, D. Venetsanos, and R. Cai. Reliability of offshore wind turbine support structures: A state-of-the-art review. Renewable and Sustainable Energy Reviews, 161:112250, 2022. ISSN 1364-0321. doi: https://doi.org/10.1016/j.rser.2022.112250. URL https://www.sciencedirect.com/science/article/pii/S136403212200171X.

Z. Wang and A. Der Kiureghian. Orthogonal plane sampling for high-dimensional reliability analysis. ASCE-ASME Journal of Risk and Uncertainty in Engineering Systems, Part A: Civil Engineering, 3(3):D4016003, Sep 2017. doi: 10.1061/AJRUA6.0000901. URL https://doi.org/10.1061/AJRUA6.0000901.

Z. Wang and J. Song. Hyper-spherical extrapolation method (hem) for general high dimensional reliability problems. Structural Safety, 72:65–73, 2018. ISSN 0167-4730. doi: https://doi.org/10.1016/j.strusafe.2017.12.005. URL https://www.sciencedirect.com/science/article/pii/S0167473016301795.

S. Winterstein, T. Ude, T. Cornell, P. Bjerager, and S. Haver. Environmental parameters for extreme response: Inverse form with omission factors. In 6th International Conference on Structural Safety and Reliability, 1993.

X. Zhu and B. Sudret. Emulation of stochastic simulators using generalized lambda models. SIAM/ASA Journal on Uncertainty Quantification, 9(4):1345–1380, 2021. doi: 10.1137/20M1337302. URL https://doi.org/10.1137/20M1337302.

A. Zimek, E. Schubert, and H.-P. Kriegel. A survey on unsupervised outlier detection in high-dimensional numerical data. Statistical Analysis and Data Mining: The ASA Data Science Journal, 5(5):363–387, 2012. doi: https://doi.org/10.1002/sam.11161. URL https://onlinelibrary.wiley.com/doi/abs/10.1002/sam.11161.